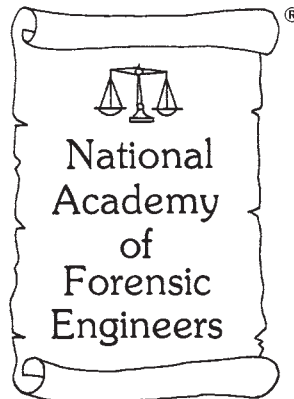


Journal of the
National
Academy OF
Forensic
Engineers[®]



National Academy of Forensic Engineers®

Journal Staff

Technical Review Committee Chair:

John Leffler, P.E.

Journal Editor:

Ellen Parson

Technical Review Process

The Technical Review Committee Chair chooses the reviewers for each Journal manuscript from amongst the members and affiliates of the NAFE according to their competence and the subject of the paper, and then arbitrates as necessary during the review process. This confidential process concludes with the acceptance of the finished paper for publication or its rejection or withdrawal. The name(s) of authors are included with their published works. However, unpublished drafts together with the names and comments of reviewers are entirely confidential during the review process and are excised upon publication of the finished paper.

National Academy of Forensic Engineers®

Board of Directors

President

Jeffrey D. Armstrong, P.E.
Fellow

President-Elect

John P. Leffler, P.E.
Senior Member

Senior Vice President

William C. Bracken, P.E.
Fellow

Vice President

Michael D. Leshner, P.E.
Fellow

Treasurer

Jerry S. Ogden, P.E.
Fellow

Secretary

Paul Swanson, P.E.
Member

Past Presidents

E. Ross Curtis, P.E.
Senior Member

Paul R. Stephens, P.E.
Fellow

Richard M. Ziernicki, Ph.D, P.E.
Fellow

Directors at Large

Martin Gordon, P.E.
Member

Marvin M. Specter, P.E., L.S.
Fellow

Executive Director

Arthur E. Schwartz, Esq.

Submitting Proposed Papers to NAFE for Consideration

A concise abstract of approximately 100 words shall be sent to the Journal Editor for initial consideration. Upon approval of the abstract, the author will be scheduled to present their work at one of the semi-yearly NAFE Technical Conferences. A 90% complete draft copy of the manuscript shall be submitted to the Journal Editor for review and approval no later than 30 days before the conference.

For complete details about requirements for authors, visit:

www.nafe.org/assets/docs/journalcontents.pdf

For the NAFE Bylaws content “Responsibilities of, Obligations of and Guidelines for Authors, the Journal Editor, Technical Review Committee Chair, and Technical Reviewers,” visit:

www.nafe.org/assets/docs/journalguidelines.pdf

Copies of the Journal

The Journal of the National Academy of Forensic Engineers® contains papers that have been accepted by NAFE. In most cases, papers have been presented at NAFE seminars. Members and affiliates receive a copy of the Journal as part of their annual dues. To obtain additional copies, the costs are as follows: \$15.00 for members and correspondents of the NAFE; \$30.00 for members of the NSPE not included in NAFE membership; \$45.00 for all others. Requests should be sent to Arthur Schwartz, Executive Director, NAFE, 1420 King St., Alexandria, VA 22314-2794. Individual Journal papers may also be purchased and downloaded from the NAFE website at www.nafe.org.

Editor’s Note

Some graphics reproduced in this black and white print edition are more clearly represented in the electronic version, which displays graphics in full color.

Comments by Readers

Comments by readers are invited, and, if deemed appropriate, will be published.

Send to: Arthur Schwartz, Esq., Executive Director, 1420 King St., Alexandria, VA 22314-2794.

Comments can also be sent via email to journal@nafe.org.

Material published in this Journal, including all interpretations and conclusions contained in papers, articles, and speeches, are those of the specific author or authors and do not necessarily represent the view of the National Academy of Forensic Engineers® (NAFE) or its members.

© 2015 National Academy of Forensic Engineers® (NAFE)

Table of Contents

* Forensic Engineering Experience with Electrically Ignited Fires	1
<i>By Roger L. Boyell, P.E. (NAFE 696F)</i>	
* Forensic Engineering Analysis of an Emergency Bridge Replacement Project	9
<i>By Paul G. Swanson, P.E. (NAFE 653S)</i>	
* Generalized Deformation and Total Velocity Change Analysis with Missing Vehicle Stiffness Coefficients; G-DaTAAV™	15
<i>By Jerry S. Ogden, P.E. (NAFE 561F)</i>	
* Forensic Engineering Investigation of Workplace Incidents Involving Machinery	35
<i>By Richard Ziernicki, Ph.D., P.E. (NAFE 308F)</i>	
* Furnace Malfunction & Forensic Engineering Wiring Reconstruction	45
<i>By John Certuse, P.E. (NAFE 708F)</i>	
* Forensic Engineering Investigation and Analysis of a Tower Crane Collapse	53
<i>By Bransford Pickett, MScBa, P.E. (NAFE 795M)</i>	
+ Forensic Engineering Analysis of Dynamic Forces Created by Pedestrians Impacting Plate Glass at Different Speeds	73
<i>By Michael Kravitz, P.E. (NAFE 451F)</i>	

* Papers presented at the NAFE seminar held 1/10/15 in Hollywood, FL.

+ Paper presented at the NAFE seminar held 7/5/14 in Washington, D.C.

Forensic Engineering Experience with Electrically Ignited Fires

By Roger L. Boyell, P.E. (NAFE 696F)

Abstract

After a fire that may have been caused by an electrical defect or malfunction, significant physical evidence is often what was most destroyed in the fire. The evidence void might be filled with fire investigators' inference or speculation that the cause was a specific electrical failure. This paper illustrates two fires in which the initial reconstructions claiming electrical ignition were subsequently found to be wrong. In one case, an investigator drew a conclusion about an extension cord from a floor fire pattern, and this interpretation was refuted when further evidence was unearthed. Investigators on another case retained evidence to support an obviously defective room air conditioner. However, the unit later was shown to be only a victim of the fire, and the needed evidence had been lost. Both cases involved extensive litigation.

Keywords

Electrical fire, electrical ignition, electrical failure, extension cord

Introduction

During fire investigations, sometimes determining the origin and cause of the fire might come down to "it must have been electrical" only after methodically ruling out all other possibilities. Then investigators might develop plausible arguments for scenarios involving electrical ignition of combustibles, including short circuits, overheated conductors, intermittent connections, arcing, and combinations of these effects.

On the other hand, sometimes the electrical cause in a fire scene is immediately apparent. The post-fire evidence is obvious, and the investigator can state with certainty that a specific electrical defect or malfunction caused the fire. But, as will be seen in the following cases, sometimes that investigator is wrong.

Case A, Extension Cord

Case A (all photographs for this section taken by Paul J. Boerner) involved an overnight fire in a house under construction (**Figure 1**) that resulted in extensive damage (**Figure 2**). The fire gutted most of the interior (**Figure 3**). Immediately after the incident, fire investigators observed numerous electrical extension cords (**Figure 4**) and propane heater hoses (**Figure 5**) that had been strung by various contractors working on the interior the day before the fire.

The investigators took note of the cans of paint and bottles of propane (**Figure 6**) stored at the site, observing the route of the fire (**Figure 7**) as it climbed through the roof. Interest centered, in particular, on one orange extension cord that wound through the



Figure 1

House under construction at the time of the fire.



Figure 2

Fire inside broke through the roof.

structure (**Figure 8**) and into an area exhibiting heavy fire damage (**Figure 9**).

The orange jacket of the extension cord had been burned away near a plug-and-socket junction with a black power cord (lower right of **Figure 10**). The junction was encrusted with debris (right side of **Figure**

11), and the power cord was found to originate from a dual-head halogen work light (**Figure 12**), which later was found to draw 1,000 watts of power.

Although a winter snowstorm impeded the fire examination, the plug-and-socket junction was retained for further examination (**Figure 13**). An investigator



Figure 3
Interior heavily damaged.



Figure 4
Various contractors' extension cords.



Figure 5
Propane tank and hoses.



Figure 6
Paint cans and propane tanks.



Figure 7
Fire damage from ground floor through roof.



Figure 8
Orange extension cord of particular interest.



Figure 9
Extension cord leading into area of heavy damage.

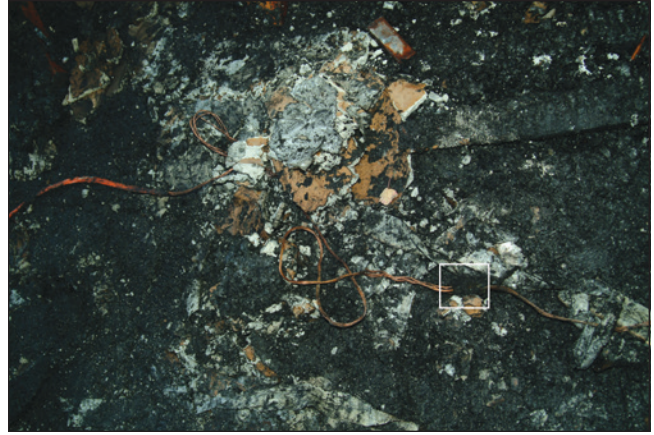


Figure 10
Plug-and-socket junction (at lower right of center).

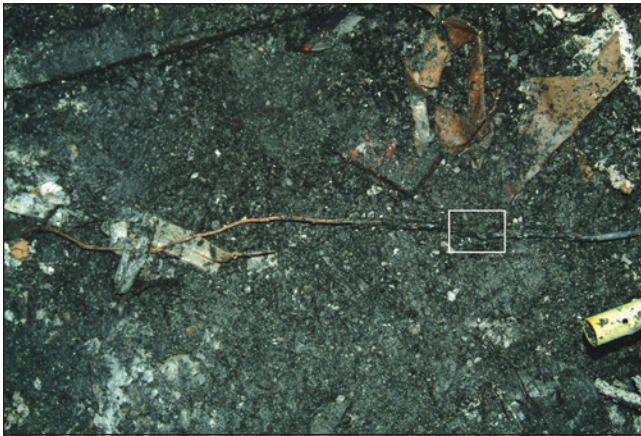


Figure 11
Plug-and-socket junction encrusted with debris.



Figure 12
Work light that was plugged into the extension cord.



Figure 13
Extension cord (on the left), work light cord (on the right).

for the property owner said he had observed a distinct pattern showing an imprint of the allegedly overheated plug-and-socket junction on the wood floor in the upstairs hallway as he cleared the debris for examination. Based on this observation, the investigator claimed that the overheated electrical junction where the work light power cord was plugged into the extension cord was the cause of the fire — and that the fire patterns on the

walls supported his findings. Accordingly, he retained the extension cord and work light and secured them in an evidence locker. Because he believed this electrical junction was the obvious cause of the fire, he did not retain any other evidence.

The extension cord and work light were attributed to one of several contractors who had been working at the site. However, that contractor's fire investigator identified other potential non-electrical causes. For example, he claimed that fire patterns showed the origin of the fire to be at the downstairs level (where propane heaters had been operating) and that the extension cord was merely a victim.

Engineering examination of the physical evidence was delayed by legal issues. The property owner (an individual) brought suit against the builder (a construction company). The individual and the company were insured by different carriers. Several contractors and subcontractors were all brought into the litigation as co-defendants and cross-claimers. In fact,

it took four years to complete all of the depositions, interviews, correspondence, affidavits, motions, and hearings about admissibility of the evidence.

Eventually, the physical evidence was to be made available for examination. When the big day came, the extension cord and work light were unwrapped (Figure 14), and the first peek at the allegedly burned electrical junction (Figure 15) showed it to be intact and unburned. The debris that encrusted the junction seemingly protected it from damage during the fire. Engineers retained by the accused contractor opined that this physical evidence indicated the contractor's electrical equipment was not responsible for the fire.

Not being deterred, the property owner's expert insisted that X-rays would show there was arcing or some other electrical damage at the junction. As a result, more time and money were spent obtaining high-resolution X-rays. Nevertheless, inspection of the resulting radiographs of the evidence (Figure 16 and Figure 17) showed that the electrical connections between the plug and the socket were perfectly normal

and could not have been the cause of the fire. In addition, when examined under X-ray, the work light (Figure 18) and the far end (plug) of the extension cord (Figure 19) showed no electrical damage. Two more years transpired due to more expert reports, addendums, explanations, affidavits, and lawyers' correspondence about the matter. Finally, the initial investigator agreed under deposition cross-examination that his interpretation of the floor pattern may have been in error.

It is likely that the imprint he saw on the wood floor was not a burn pattern caused by an overheated junction, but rather the shadow from its area having been shielded from the heat of the fire. Simply put, the investigator may have misinterpreted the negative image as a positive and jumped to the wrong conclusion.

Although the cause of the fire remained undetermined, the investigators for the accused contractor argued that it was not due to the electrical extension cord, and the legal case was eventually settled by all parties.



Figure 14
Evidence when first opened for examination.



Figure 15
Plug (black) and socket (orange) showing minimal damage.

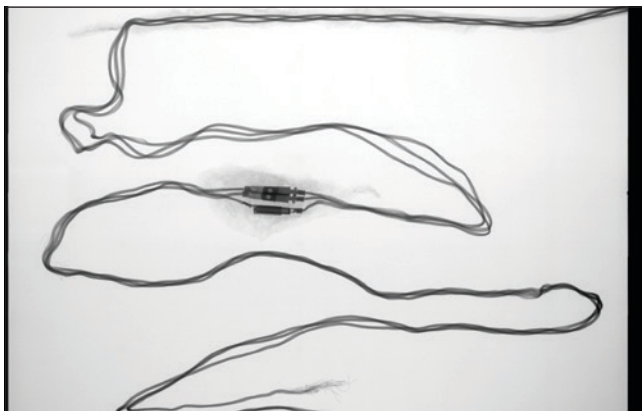


Figure 16
X-rays of power cords forming the junction.

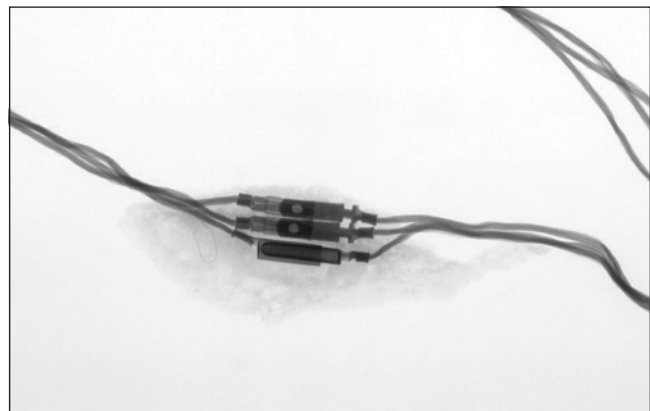


Figure 17
Enlargement showing no electrical defect.

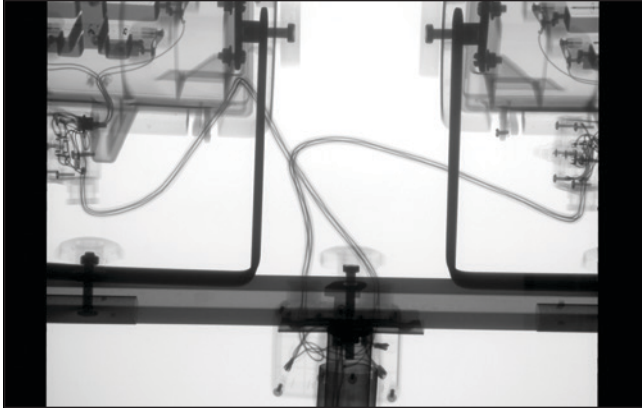


Figure 18

X-ray of work light showing no electrical abnormality.

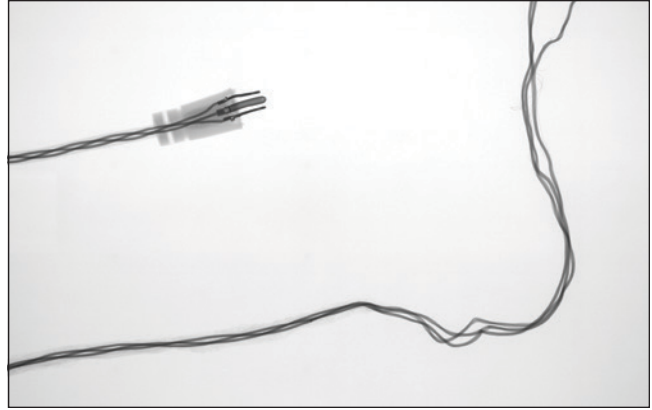


Figure 19

Extension cord plug also showing no electrical abnormality.

Case B, Air Conditioner

Case B (all photographs for this section taken by the author) was a fire that consumed everything in the room of origin. An eyewitness who suffered skin burns said the fire started in a free-standing in-room air conditioner while it was running. In fact, the witness said he saw the fire begin right at the bottom of the unit

and then blossom into a large area of flame before he was able to escape.

Fire investigators preserved the remains of the unit as evidence and presented them for examination (**Figure 20** and **Figure 21**). The allegation was that some electrical defect or malfunction caused



Figure 20

Front view of remains of room air conditioner.



Figure 21

Side view of remains of room air conditioner.



Figure 22

Exemplar of room air conditioner.



Figure 23

Interior of exemplar unit.

the unit to ignite; therefore, the manufacturer was responsible.

With this portable air conditioner (see exemplar in **Figure 22**), room air is blown through the evaporator coils at the top, and outside air is circulated through the interior by plastic ducts that run to an adjacent window. The molded plastic case can be removed to show the internal construction (**Figure 23**).

The exemplar exhibits electrical wiring, a compressor motor, and fan motors (**Figure 24**), all of which can be compared with the evidence unit to locate the presumed defect or malfunction. Upon investigation, such comparison revealed that the bottom of the evidence unit was surprisingly intact (**Figure 25**), considering that the fire was said to have begun there.

Examination of all the evidence, including the power cord (**Figure 26**) and the plug and wall receptacle (**Figure 27**), supported the allegation that

the air conditioner ignited first and spread to the rest of the room. It was curious, however, that the retained evidence was so thoroughly destroyed (**Figure 28**). It appeared as if a blowtorch had been applied to the unit rather than it being consumed in a plastic or wood fire. There was no damage pattern typifying a localized electrical event. Perhaps the air conditioner was merely a victim of the fire that had started elsewhere.

Information was pieced together from many witnesses. Everyone said the fire started near the front corner of the house. The layout of the premises is shown in **Figure 29**. The portable room air conditioner had been running to cool the room. The unit obtained its intake and exhaust from the front window.

The key witness said he entered the room and walked to the air conditioner as shown in **Figure 29**, seeing the flame begin there. Before he could do anything, the unit became engulfed in flames, and he ran out the front door to the street.

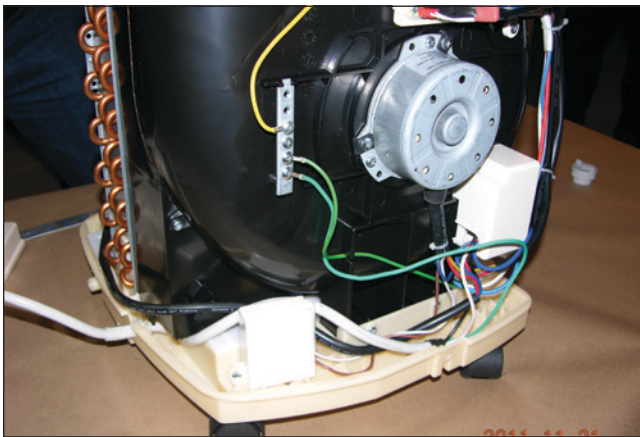


Figure 24
Fan motor and electrical wiring.



Figure 25
Underside of evidence unit showing little damage.

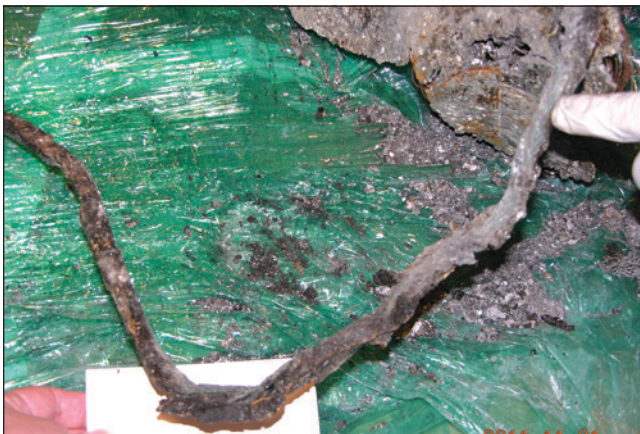


Figure 26
Power cord insulation burned away.



Figure 27
Plug and receptacle burned from outside in.



Figure 28

Evidence of intense fire consuming the entire unit.

Shortly thereafter, the room exhibited flashover: nearly simultaneous ignition of the gaseous combustion products from the initial fire. These products would have diffused throughout the confined space. Upon the gases having been brought to a critical concentration and temperature, flashover results in fire damage to every exposed surface in the room.

Despite the simplicity of the defective air conditioner hypothesis, extensive litigation ensued. Buried in the text of witness interviews was a statement by the neighbor that he also saw the fire begin at the front of the house and progress from there into the structure.

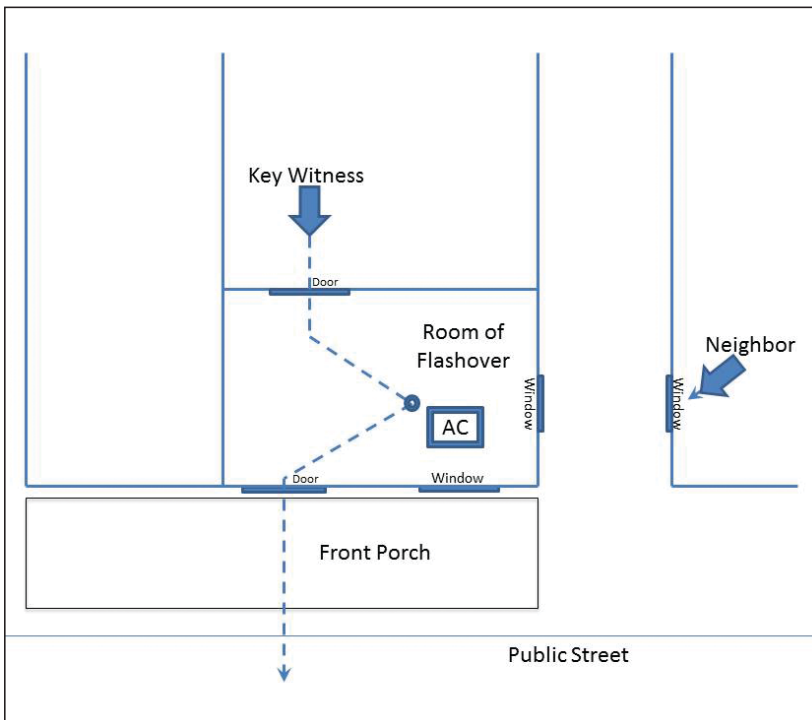


Figure 29

Layout of the house showing witness path.

An astute investigator for one of the parties obtained a photograph that showed the front of the house was really an enclosed porch, although most of the porch was burned away. This meant that the neighbor actually saw the initial burst of flame in or on the porch, not in the room containing the air conditioner. Incidentally, the house was in an area of town in which fire bombings had occurred in the past, so the possibility of an intentionally set fire was not out of the question.

An alternative hypothesis was offered by engineers retained by the manufacturer: The fire started on the porch and was drawn into the running air conditioner. So, in essence, what the key witness saw was not the initiation of the fire, but rather its first exposure from combustion inside the air conditioner. The ducts between the unit and window were consumed by the fire drawn in from outside, along with the unit's plastic enclosure.



Figure 30

Inadequately preserved debris from front window.

While an electrically ignited fire usually shows a localized area of most intense destruction, this air conditioner exhibited uniform damage. That would be consistent with fire attacking the unit from the burning material circulating within it.

This alternative hypothesis of the air conditioner being the victim could not be disproved, because investigators on the scene had not considered the origin to be on the porch. Little material was retained from outside the window of the room, and that material was not well preserved for examination (Figure 30).

The ambiguity as to where the fire started, whether the air conditioner was actually the first combustible item, and why it showed no indication of an electrical defect or malfunction all contributed to the settlement of the legal case.

Conclusion

A fire investigator's initial opinion that "it must have been electrical" does not always prove true once further engineering examination takes place. This paper relates how the extension cord in Case A and the air conditioner in Case B were wrongly accused of being electrical ignition sources for fires. In both cases, other non-electrical events were likely causes.

Forensic Engineering Analysis of an Emergency Bridge Replacement Project

By Paul G. Swanson, P.E. (NAFE 653S)

Abstract

A bridge that provided grade separation and vehicle access over a commercial rail line in a small town in the Southeast had sustained soil erosion and settlement as a result of a severe storm. Replacement of the bridge was undertaken by the State Department of Transportation as an emergency project in cooperation with the Federal Highway Administration using the design-build procurement method. Subsequent to the bidding, the design-build team made several changes to the bridge foundations and superstructure that significantly increased the cost of construction. The contractor claimed damages against the other members of the design-build team resulting from design errors and an alleged breach of the customary standards associated with the design-build concept.

Keywords

Design-build, bridge foundation, PDA, pile capacity

Project Background

The bridge structure was supported on a system of shallow foundations at each abutment and three internal bents (internal column and pile support), which were spaced about 25 feet on centers and spanned the railroad tracks (**Figure 1**). They supported concrete columns that, in turn, supported the bridge deck. Settlement at one of the bridge abutments caused closure of the roadway (**Figure 2**).

State Department of Transportation (SDOT) engaged a firm to prepare a request for proposal (RFP) for the bridge replacement and asked that a local geotechnical engineer conduct the investigation associated with the RFP. SDOT issued the RFP for the project in April 2012. Included in the RFP was a geotechnical data summary report prepared by that engineer.

A construction company (contractor), well known to SDOT and local to the area, was one of several companies that responded to the SDOT RFP. As part of its response, the contractor selected a local design engineer for the design-build team. The design engineer contracted with the same geotechnical engineer that participated in the development of the RFP for geotechnical design on the project. This design-build team was chosen as the successful bidder for the replacement bridge project.

Basis of Bid

Rather than replace the bridge in kind, the design team selected a pre-stressed concrete single span arch as the primary component of the bridge replacement



Figure 1

Vehicle bridge over Norfolk Southern Railroad.



Figure 2

Settlement resulting from soil erosion at the bridge abutment.

section (**Figure 3**). The design engineer had an expectation of using either H-piles or pipe piles for the foundation support based on the geotechnical engineer’s recommendation.

For the bid quantities, the length of the abutment wall — and therefore the length of the bridge foundation — was assumed to be 45 feet. The SDOT design minimum was 44 feet; however, there was a note in the RFP that because the alignment of the bridge was skewed to the alignment of the railroad (**Figure 4**), additional foundation width would be required, should the precast reinforced concrete floorless culvert option be chosen. The wing walls on either side of the abutments were assumed to be supported on shallow foundations. The number of piles supporting the bridge structure was assumed to be two rows of piles spaced 5 feet on centers for the length of the foundation for a total of 16 piles for each abutment. A pile length of 40 feet was used in the calculation to determine a total of 1,280 linear feet of piles for the project.

As part of the design-build process, the design team, once selected, was required to prepare and submit for review design drawings responsive to SDOT standards at three stages: 50% design, 90% design, and final design. A detailed geotechnical report supporting the design was to accompany each design submission.

Design Submission 50%

The geotechnical recommendations for pile support of the bridge abutments were based entirely on the results obtained from the two borings drilled for the SDOT RFP, even though it was “encouraged” in the RFP that the proposers obtain additional subsurface explorations prior to bid submission. The borings drilled for the RFP were located approximately 50 feet from the proposed pile locations. The only additional information included with the 50% design was the laboratory classification testing of selected soil samples obtained during the RFP drilling effort.

Based on the geotechnical engineer’s experience, HP 14x73 steel piles were recommended for support of the abutments (**Figure 5**). The pile section is generally the shape of the letter H, approximately 14 inches square, weighing 73 pounds per foot of pile length. The pile capacity was to be derived primarily from end bearing in the dense sands of a geologic formation common to the area. The assumed average pile length was 46 feet. The ultimate pile capacity was



Figure 3

Newly constructed abutments with arch culvert segments in place.



Figure 4

Existing bridge removed with soil abutments exposed.

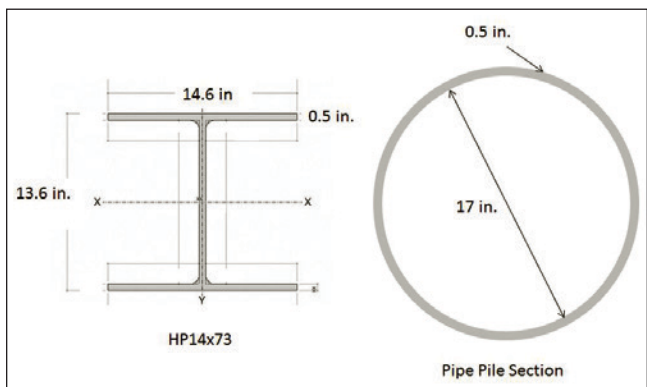


Figure 5

The 14-inch H-pile and 18-inch pipe pile sections.

estimated to be 460 kips (230 tons). The geotechnical engineer specifically discouraged the use of high displacement piles (closed-end pipe piles, as shown in **Figure 5**) due to the proximity of the railroad to the proposed pile foundations (approximately 23 feet).

The geotechnical engineer considered the installation of high displacement piles and associated lateral soil and track movement as a potential concern.

The geotechnical engineer recommended a program of dynamic testing during pile installation (index piles) using a pile driving analyzer (PDA), as shown in **Figure 6**. The purpose of the testing was to determine both the drivability of the piles and provide a refinement of the pile capacity. Generally, this is an acceptable procedure in lieu of static load testing, particularly in a design-build situation. Based on the engineer's analyses, estimated pile penetration rates, ranging from 139 to 258 blows per foot (bpf), were calculated to achieve the desired capacity for the proposed pile type and driving equipment. The analysis was based on the equipment used to drive the index piles. No pile refusal rate was established for the testing program.

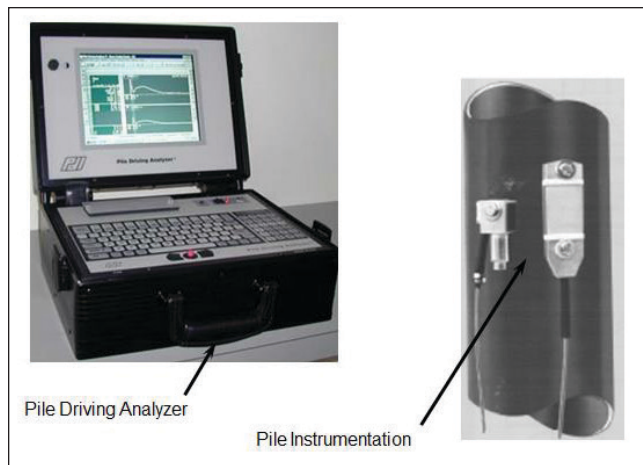


Figure 6

Pile driving analyzer readout box and instrumented pile.

The bid submission did not account for the skewed angle of intersection between the roadway alignment and the railroad alignment. The skew geometry resulted in an extended abutment foundation from 45 feet to nearly 90 feet. The number of piles increased from a total of 32 piles based on the geometry assumed at bid submission to 74 piles for the 50% design submission. At the time of the 50% design submission, no consideration was given to pile support of the retaining walls associated with the abutments. For this submission, the geotechnical engineer still provided recommendations for shallow support of the retaining walls on either side of the bridge abutments. Based on the information reviewed, it appeared that the omission of the skew angle in the calculations supporting the bid was an oversight.

Final Design Submission

Approximately eight weeks after the contract was awarded, the geotechnical engineer provided the final report in support of the design engineer's final design submission. The geotechnical engineer provided additional analyses but continued to rely on the subsurface data obtained from the initial two borings. The ultimate pile capacity for piles supporting the abutments was increased from 230 tons to 262 tons, which increased the predicted pile length from 46 feet to 52 feet. The engineer revised the number of piles to support the abutments down to 56 piles; however, pile support of the retaining walls associated with the abutments was determined to be required, increasing the overall number of piles to 83.

Based on the engineer's lateral load analysis, the pile section was revised from HP14x73 to composite sections of HP14x102 and HP14x73 welded together or HP14x89 and HP14x73 welded together.

Construction

After approval of the final geotechnical report and associated design submission, pile installation began. Four instrumented test piles were driven to depths of 49 feet to 118 feet. A summary of the test pile driving is included in **Figure 7**.

Pile Designation	Pile Type	Depth Driven (ft)	Driving Resistance (bpf)*
Pile#1	HP14x73/ HP14x102	48	42
		49	56
		68	70
Pile #2	HP14x73/ HP14x102	48	55
		49	41
Pile#1A	HP14x102	57	25
Pile#2A	HP14x73	38	40
		78	58
		97	25
		118	145

*A driving resistance of 139 to 258 bpf was required for estimated design capacity.

Figure 7

Summary of test pile driving.

As a result of the pile test program, the geotechnical engineer drilled an additional boring at the pile line location at each abutment. Based on the lack of performance of the H-piles driven on-site and review of the additional boring data, the design team decided to use 18-inch-diameter closed-end pipe piles for support of the abutments. The geotechnical engineer never amended previous concerns regarding proximity of pile driving next to the railroad tracks. A revised wave equation analysis was performed, and a new driving criterion of 50 to 55 bpf was established for the pipe piles. The result was that the production pipe piles achieved the bearing criteria with an average embedment of 35 feet to 40 feet.

The Case

A design-build contract affords the contractor very limited ability to modify the accepted bid. By its very nature, the design-build contract requires that the design-build team perform sufficient design analyses prior to bid release to establish a comprehensive bid for execution of the scope of work. The issuing authority must provide the bidders with sufficiently accurate details of the conditions and scope of work. One of the most common sources of inaccurate bid information in the traditional design, bid, and build contract, “the design documents” are not part of the bidding process for a design-build contract. Therefore, the contractor has very limited recourse to the owner should the bid turn out to be insufficient for the scope of work. In this case, the contractor claimed the excess construction cost was the result of errors made by the contractor’s design team. The contractor claimed the designer breached the standard of care with regard to providing an accurate design and estimate of quantities prior to bid.

The cost issues associated with the foundation system for the bridge fell into two major categories: 1) the number of piles required to support the bridge loads; and 2) the misjudgment of the load capacity of the chosen pile system.

The choice to replace the bridge with a floorless culvert option significantly influenced the size and uncertainty associated with the foundation system. The footprint of the pile-supported foundation given to the contractor as a basis for bid was approximately 40% of the pile-supported foundation footprint used in the final submission.

Part of the discrepancy can be attributed to the fact that the designer did not account for the skew between the alignment of the roadway and the alignment of the bridge until after bid submission. A major portion of this discrepancy related to the fact that the retaining walls to either side of each abutment also required pile support and a modification of the pile section with depth. This was primarily the result of the geotechnical engineer changing the estimate of the lateral load imposed on the abutments and retaining walls from active earth pressure to at-rest earth pressure, an increase of nearly 50%. This revised recommendation of lateral load came over two months after bid submission.

The second issue that caused significant impact to the project was the inability to attain the predicted load capacity with the chosen H-pile foundation system. The geotechnical engineer recommended and performed a case method analysis (CAPWAP, Case Pile Wave Analysis Program) in conjunction with the test piles to judge nominal capacity and confirm the driving criteria. This is standard practice in the industry. The methodology uses information obtained during pile driving to modify parameters assumed in the wave equation analysis program (WEAP) until calculations match conditions measured during driving. The modified analysis is used to generate a relationship of pile capacity and driving resistance. The driving resistance (number of blows per foot) required to achieve capacity was not attained for the test H-piles.

The use of dynamic analysis (CAPWAP) to predict a static bearing capacity of H-piles in a layered soil environment is difficult. Various researchers (Seo et al. 2009) have questioned whether full bearing (bearing across the entire area circumscribed by the pile section) can be realized in such environments. A multi-layered environment, such as the one at this site, may prevent the soil “plug” from developing at the base and along the sides of the pile.

The geotechnical engineer did not drill additional borings or perform additional field testing along the proposed pile lines but rather throughout the design relied on two borings that were significantly offset from the proposed pile lines. It was only during construction — after the chosen pile system did not attain the required bearing capacity — that additional borings on the pile lines were drilled. Even though the geotechnical engineer classified the geologic formation boundaries as consistent across all of the borings, the

layers of sands and clays at each boring location varied in elevation and affected pile driving resistance — and therefore the predicted capacity. It was also evident that significantly more clays were encountered in the two additional borings than were recognized in the original borings, which added to the difficulty of predicting capacity and driving resistance.

Using the wave equation to dynamically analyze piles assumes that sufficient strain occurs during driving to mobilize the assumed parameters in the soil profile. The ASTM standard test method for dynamically testing deep foundations (ASTM D4945-2012) recommends at least 2 millimeters of pile movement per blow to remain within a range of movement consistent with the analysis. The penetration rate (139 to 258 bpf), resulting from the geotechnical engineer's analysis of the H-piles (equated to movements of 2.2 mm to 1.2 mm), was largely outside the range recommended by ASTM. One test pile that was driven to more than twice the predicted termination depth (118 feet) attained the required driving resistance. Only then did the geotechnical engineer decide to change the pile type from H-piles to closed-end pipe piles. Once the change was made, construction proceeded without further delay.

It was evident from the communication documents recovered during discovery that both the design engineer and the geotechnical engineer performed as if the contract was a traditional design, bid, build contract. The design effort prior to bid consisted primarily of rough sketches of proposed geometry and design assumptions based on past experience with little or no application to the specific site. Low-displacement pilings, such as H-piles, were not generally used for bridge support in this geologic environment. The geotechnical engineer's reluctance to obtain more boring information resulted in a dependency on a dynamic test method to determine pile capacity that could only be validated during construction, resulting in an expensive change of materials and equipment to the contractor. The case was settled out of court with a negotiated settlement.

References

ASTM D4945-2012. Standard test method for high-strain dynamic testing of deep foundations. West Conshohocken, PA; ASTM International.

Seo H, Yildirim Z, Prezzi M. Assessment of axial load response of an H pile driven in multilayered soil. *Journal of Geotechnical and Geoenvironmental Engineering*. 2009; Vol 135 (12), 1789–1804.

Generalized Deformation and Total Velocity Change Analysis with Missing Vehicle Stiffness Coefficients; G-DaTA ΔV^{TM}

By Jerry S. Ogden, P.E. (NAFE 561F)

Abstract

Analysis of vehicle deformation from impacts largely relies upon A and B stiffness coefficients for vehicle structures in order to approximate the velocity change and accelerations produced by an impact. While frontal impact stiffness factors for passenger vehicles, light trucks, vans, and sport utility vehicles are relatively prevalent for modern vehicles, stiffness factors for rear and side structures — as well as heavy vehicles, buses, recreational vehicles, trailers, motorcycles, and even objects — are essentially non-existent.

This paper presents methods developed from the principles of energy, momentum, restitution, tire forces, and rotational mechanics applicable to deformation profile analysis by eliminating the need for structural A and B stiffness coefficients for both vehicles involved in a two-vehicle collision. This is often achievable for most collision combinations. Additionally, the application of these developed principles to RICSAC (Research Input for Computer Simulation of Automobile Collisions) test data will demonstrate the accuracy achieved by using this methodology — even when the structural stiffness values for both vehicles are available, but only the frontal stiffness values of one vehicle are utilized.

Keywords

Forensic engineering, force deflection, damage analysis, missing vehicle stiffness, velocity change from damage, motorcycle, heavy vehicles, object impacts, G-DaTA ΔV^{TM}

Background

One of the earliest approaches to analyze vehicle damage was developed through the work done by Campbell in the early 1970s¹. Campbell observed a linear relationship between fixed barrier impact speeds and residual deformation of a vehicle structure during full-scale impact testing using General Motors vehicles.

Further research into this matter was conducted by McHenry and others at Cornell Aeronautical Lab (currently known as CALSPAN) through the development of SMAC (Simulation Model for Automobile Collisions), which improved upon Campbell's earlier observations. Specifically, McHenry noted that vehicles behave like linear energy-dissipating springs. The studies by Campbell and McHenry were later adapted into a computer analysis package known as the Collision Reconstruction of Accident Speeds on Highways Program, or CRASH, which was a first approximation tool for use in estimates necessary for the SMAC analysis. The current edition of this

program is known as CRASH III, with other clone or similar variants in use today².

Current common practices for motor vehicle damage analysis, such as standardizing measurement protocols^{3,4} and a widespread use of modernized equations that account for rotational effects⁵, have developed into accurate, reliable, and commonly used means for determining collision severity levels and collision velocities. This is assuming proper structural stiffness values for each colliding vehicle characteristic (for both vehicles and the specific impacted surface) are available. Although extensive test data is presently available from vehicle manufacturers and test laboratories for the determination of frontal stiffness coefficients (for many passenger vehicles and light trucks), few tests are available for such determination as they relate to side and rear surface vehicle specific stiffness coefficients. Additionally, there is limited data available for heavy vehicle frontal barrier impacts (including semi-tractors

and buses), for frontal stiffness coefficient determination. Accordingly, either additional expensive and time-consuming barrier tests are needed to fill these gaps, or another method of analysis is needed.

In general, the limiting assumptions and limitations of CRASH III and similar CRASH-based programs are as follows:

- Deformation energy is equal to the impact kinetic energy loss.
- Collisions are inelastic, and the centroids of damage reach a common velocity.
- Sliding between vehicles occurs during the separation phase of the impact and not during the approach velocity change phase; therefore, it is not accounted for in the velocity change analysis.
- Tire-ground forces are negligible (non-conservative forces external to the impact) or very small as compared to the collision force and do not need to be accounted for.
- Damage profile measurements are limited by evenly spaced measurements of 2, 4, 6 or more deformation depths over uniform spaced measurement widths.
- Vehicle structural stiffness is defined by categories of vehicles by type (i.e., car, truck, van), and wheelbase lengths, all assumed to have similar inertial and stiffness characteristics.

This paper presents the equations derived from engineering principles that allow for the following analysis considerations not currently considered by CRASH-type analysis procedures:

- Develop analysis methodologies that eliminate the dependence upon multiple structural stiffness coefficients for permanent vehicle structural deformation analysis, regardless of the impacted surface and vehicle type involved.
- Develop analysis methodologies that account for oblique and offset collisions that result in principal directions of force that do not pass through the mass centers of vehicles and produce rotation.
- Develop analysis methodologies that account for friction due to the colliding surfaces of vehicles sliding during the approach velocity change of an impact.

- Develop analysis methodologies that account for forces external to the impact produced by tire-ground forces during the approach velocity change of an impact.
- Establish important relationships regarding impact forces as they relate to motor vehicle collisions and vehicle deformation properties.

Basic Equations

The basic CRASH algorithms are derived from sound principles and applications of Newton's laws of motion, Hooke's law, and the conservation of energy and momentum. For central, single degree of freedom impacts — where the vehicle-to-vehicle colliding system is treated as a simple harmonic oscillating spring system — the basic force-deflection equation is as follows:

$$F = (A + B \cdot c^R) \cdot w \quad (1)$$

Where, A = (force / length), which is the force per unit depth to initiate damage to the vehicle and applied throughout the application of external forces resulting from the collision

B = (force / area), the generalized spring constant associated with resistance to continued deformation/spring compression of the vehicle structure as a result of the external forces of the collision

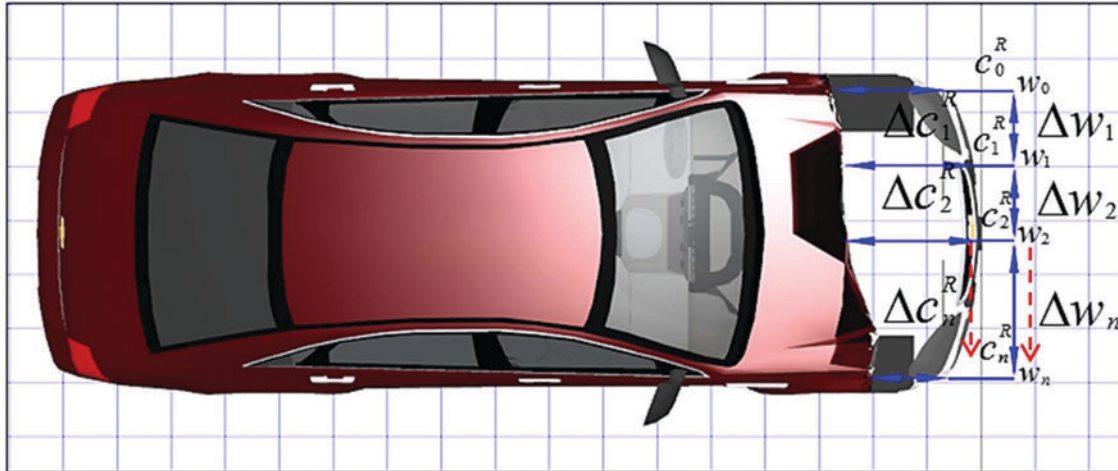
c^R = (length), residual inward deformation measured post-collision, perpendicular to the damaged surface

w = (length), width of deformation profile between measured points

Equation 1 is a basic expression that relates to a uniform deformation profile of uniform deformation depth across its entire width. For more complex damage profiles, the impact force is approximated using what will be defined as the *Central Impact Force-Deflection Model*:

$$\sum_{j=0}^n F_j^I = \sum_{j=0}^n (A_i + B_i \cdot \Delta c_j^R) \cdot \Delta w_j \quad (2)$$

Where, $\Delta c_j^R = \frac{(c_j^R + c_{j+1}^R)}{2}$ = (length) average deformation depth between measured points j and $j+1$, $j=0 \dots n$ measurements across differential width



Description of point measured	Distance from Left Front (0)	Distance to undamaged profile
Left front corner	w0: +0 cm (0 inches)	c0: +81 cm (32 inches)
Left front frame rail	w1: +46 cm (18 inches)	c1: +81 cm (32 inches)
Center bumper reinforcement bar	w2: +92 cm (36 inches)	c2: +71 cm (28 inches)
C3...C(n-1)	w3...w(n-1)	c3...c(n-1)
Right front corner	w(n): +183 cm (72 inches)	c(n): +51 cm (20 inches)

So that,
$$\Delta c_1^R = \frac{c_0^R + c_1^R}{2} = \frac{(81cm + 81cm)}{2} = 81cm (32 \text{ inches})$$

$$\Delta c_2^R = \frac{c_1^R + c_2^R}{2} = \frac{(81cm + 71cm)}{2} = 76cm (30 \text{ inches}), \text{ and so forth.}$$

And,
$$\Delta w_1 = w_1 - w_0 = (46cm - 0cm) = 46cm (18 \text{ inches})$$

$$\Delta w_2 = w_2 - w_1 = (92cm - 46cm) = 46cm (18 \text{ inches}), \text{ and so forth.}$$

Figure 1
Measured damage dimensions.

$\Delta W_j = (w_{j+1} - w_j)$ = (length) width of deformation interval between measured points j and j+1, j=0...n measurements across differential width

Figure 1 shows an example of how the deformation depth and width measurements are made and tabulated for ease of use.

Integrating Equation 2 with respect to the deformation depth, Δc^R , provides the work done over the deformation profile due to the collision impulse. This integral operation produces what is hereto defined as the *Central Impact Work/Energy Model* of Equation 3.

$$\sum_{j=0}^n F_j^I = \sum_{j=0}^n (A_i + B_i \cdot \Delta c_j^R) \cdot \Delta w_j$$

$$E_i = \sum_{j=0}^n \int_0^{\Delta w_j} F_j^I \cdot d\Delta w_j = \sum_{j=0}^n \int_0^{\Delta c_j^R} ((A_i + B_i \cdot \Delta c_j^R) \cdot \Delta w_j) \cdot d\Delta c_j^R$$

$$E_i^{damage} = \sum_{j=0}^n \left(A_i \cdot \Delta c_j^R + \frac{B_i \cdot (\Delta c_j^R)^2}{2} + \frac{A_i^2}{2 \cdot B_i} \right) \cdot \Delta w_j \quad (3)$$

Where, A_i and B_i = unique structural stiffness values for the impacted surface of the i^{th} vehicle (for a two-vehicle system, $i = 1..2$)

Δc_j^R = the residual deformation, or “crush”, of the i^{th} deformation measured on the i^{th} vehicle

perpendicular to the damaged surface from its undamaged dimensions

Δw_j = width of the j^{th} deformation, measured parallel to the damaged surface of the i^{th} vehicle

By utilizing a numerical method of determining the work, E_i , done by the impact force, F_i , for each vehicle, $i=1..2$, the restriction imposed by CRASH-type programs of 2, 4, or 6 evenly spaced deformation measurements is eliminated. Utilizing Equations 2 and 3 allows for the analysis of deformation with as many measurements as needed and at any measured width in order to accurately describe a vehicle’s damage profile.

The basic equations for a completely plastic central impact that does not consider restitution, tire-ground forces, rotation, or inter-vehicle friction are the basis of the earlier CRASH-based computer programs, and the basic velocity change magnitude equations are as follows:

$$\Delta V1 = \sqrt{\frac{2 \cdot m_2 \cdot (E1_{damage} + E2_{damage})}{m_1 \cdot (m_1 + m_2)}} \quad (4)$$

$$\Delta V2 = \sqrt{\frac{2 \cdot m_1 \cdot (E1_{damage} + E2_{damage})}{m_2 \cdot (m_1 + m_2)}} \quad (5)$$

Central Impacts Accounting for Restitution and Tire-Ground Forces

This author has previously published methods for utilizing vehicle deformation profiles for determining velocity changes of collinear, central impacts that account for the effects of restitution and tire-ground forces of an impact^{6,7}. Restitution effects are greatest

at lower impact velocity change levels ($0 < \Delta v \leq 10$ mph) and will range between $0.2 \leq e \leq 0.6$ for most collisions with the highest restitution values occurring at the lowest velocity change levels of the range, and will approach $e \approx 0$ at higher impact velocity change levels ($\Delta v > 20$ mph).

Tire forces may contribute significantly to the external impulses acting upon a low velocity change impact ($\Delta v \leq 10$ mph), but are often considered insignificant for higher level impacts. Examples of when tire forces may not be negligible are as follows:

- Collinear rear-end collision event where front vehicle (target vehicle) is braking when struck by rear vehicle (bullet vehicle).
- Broadside impact where side-struck vehicle (target vehicle) slides broadside against the roadway surface during the impact.
- Impact with a heavy vehicle either broadside or while brakes are applied on the heavy vehicle and/or trailer.
- Any collision configuration where a motion constraint, such as wheel blocking, curb, wall or barrier, etc., may be present at impact.

Figure 2 shows how the external impulse of braking force interacts external to the forces of an impact event. It is important to note that the impulse of tire-ground forces is external to the collision impulse in that tire-ground forces are “non-conservative” impulse constraint forces acting upon the system during the approach velocity change, which is common for many constrained holonomic and non-holonomic dynamic systems⁸.

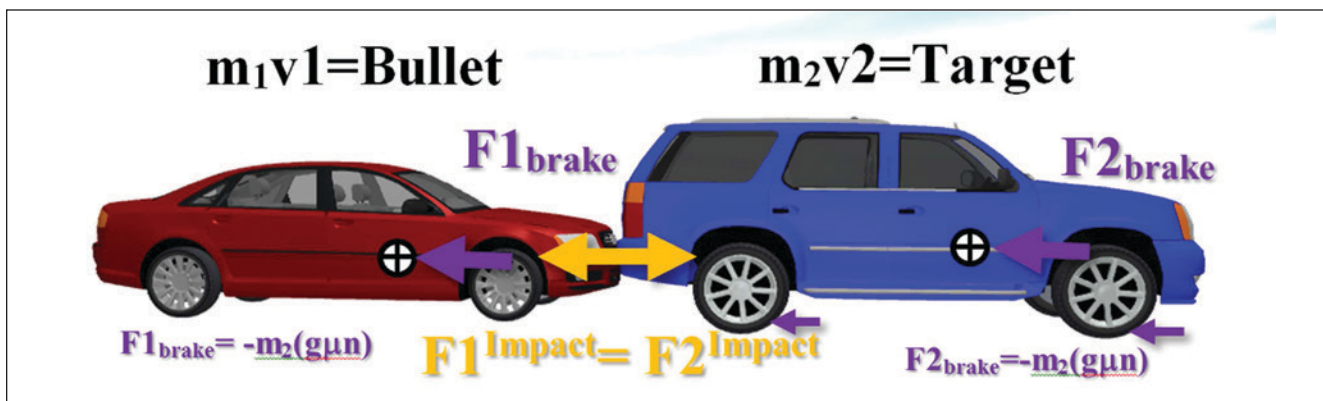


Figure 2
Tire-ground forces external to collision impulse (front vehicle braking).

The basic equations derived while accounting for restitution effects during the approach velocity change as well as non-conservative external tire-ground impulse constraint forces are hereto defined as the *Central Impact Force-Deflection Velocity Change Equations*:

Tire-ground contribution vehicle 1:

$$F1^{brake} = m_1 \cdot a1^{brake} = m_2 \cdot (g\mu n)$$

$$m_1 \cdot \frac{\Delta v1^{brake}}{\Delta t} = m_2 \cdot (g\mu n)$$

$$\Delta v1^{brake} = \frac{m_2 \cdot (g\mu n) \cdot \Delta t}{m_1}$$

Tire-ground contribution vehicle 2:

$$F2^{brake} = m_2 \cdot a2^{brake} = -m_2 \cdot (g\mu n)$$

$$m_2 \cdot \frac{\Delta v2^{brake}}{\Delta t} = -m_2 \cdot (g\mu n)$$

$$\Delta v2^{brake} = \frac{-m_2 \cdot (g\mu n) \cdot \Delta t}{m_2} = -(g\mu n) \cdot \Delta t$$

$$\Delta V1 = (1+e) \sqrt{\frac{2 \cdot m_2 \cdot (E1^{damage} + E2^{damage})}{m_1 \cdot (m_1 + m_2)}} + \frac{m_2 \cdot (g \cdot \mu \cdot n) \cdot \Delta t}{m_1} \quad (6)$$

$$\Delta V2 = (1+e) \sqrt{\frac{2 \cdot m_1 \cdot (E1^{damage} + E2^{damage})}{m_2 \cdot (m_1 + m_2)}} - (g \cdot \mu \cdot n) \cdot \Delta t \quad (7)$$

The previous equations (as derived) are limited to central impacts or collinear impacts that produce negligible rotation to either vehicle due to impact offset. It is important to again stress that these velocity change magnitudes are vectors along a single coordinate line of action, so that the absolute value of the velocity change for the bullet vehicle ($\Delta V1$) is *increased* by tire-ground impulse constraint forces, while the absolute value of the velocity change for the target vehicle ($\Delta V2$) is *decreased* by tire-ground impulse constraint forces.

Oblique and Offset Impacts

Oblique and offset impacts result from applied forces that do not act through the mass centers of at least

one of the colliding vehicles. As such, the applied force creates a pure force couple, resulting in rotation or at least the potential for rotation to one or both colliding vehicles along with translation, or at least the potential for translational motion. When rotation occurs, tire forces are often counteracting to the moment created by the oblique force application. **Figure 3** shows the effects of an oblique impact upon the overall planar motion (x, y, ϕ) of a vehicle, resulting in rotation about the z -axis in yaw (ϕ).

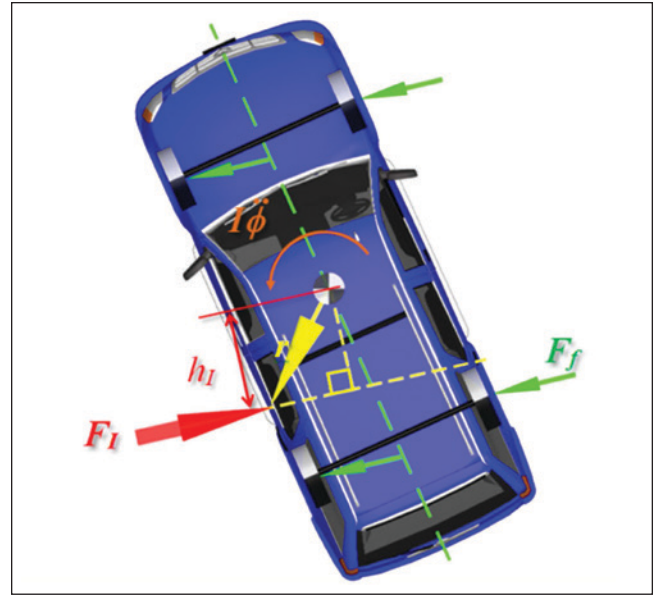


Figure 3

Moment arm applied to produce rotation about mass center.

The mass moment of inertia is an object's measure of resisting rotational acceleration, just as mass is the measure of a body's resistance to translational acceleration. The moment of inertia of an object is a function of shape and mass. If the moment of inertia is determined about a primary axis that passes through the mass center of an object, it is called a *polar moment of inertia*⁹. Using polar moments of inertia, hereto simply referred to as *mass moment of inertia*, and determining dynamics about polar (or primary) axes makes analysis much easier, and is routinely used for motor vehicle collision analysis with few exceptions. The moment of inertia about any axis, to include those that do not pass through the mass center of a body, can be determined using the parallel axis theorem if the polar moment of inertia is known. Likewise, the polar moment of inertia of a composite or oddly shaped object can be determined using the parallel axis theorem with respect to each of the individual moments of inertia of the geometric shapes that make up the total body shape. In

general, the moment of inertia is determined as the sum of the product of all the differential mass elements of the body, dm , and the square of its distance from the axis of rotation, r .

$$dI = r^2 \cdot dm$$

$$I = \sum_{i=1}^n r_i^2 \cdot m_i \tag{8}$$

Another method of describing the polar moment of inertia of an object with great utility is known as the *radius of gyration*, k_g , which assumes all the mass, m , is concentrated within an equivalent radius about a primary axis that passes through the mass center of the object^{9,10}.

$$I = m \cdot k_g^2 \tag{9}$$

Because passenger vehicles, light trucks, and vans are non-homogeneous complex geometric shapes, the mass moment of inertia is determined experimentally using tilt table measurements, or more commonly from best-fit equations derived from experimental data. Garrott presented data from the NHTSA Light Vehicle Inertial Parameter Data Base containing measured vehicle inertial parameters of 356 tested vehicles, plus tilt table data for 168 vehicles¹¹ as a follow-up to an initial paper presenting an algorithm for determining moments of inertia for the curb weight of unloaded vehicles by distinct vehicle classifications¹². Neptune presented a method for determining the yaw moment of inertia (I_{zz} , or mass moment of inertia about the z -axis of the vehicle) based upon the method presented by Garrott, but allowing for the addition of occupant and cargo weights¹³, providing greater utility for collision analysis. Equation 10 from the Neptune paper reduces

to the best fit algorithm developed by Garrott when the vehicle is unloaded.

$$I_{zz} = \frac{m_{curb}}{K_G} \cdot (L^2 + b^2) \cdot \left(K_M \cdot \left(\frac{m_{loaded} - m_{curb}}{m_{loaded}} \right) \right) \tag{10}$$

Where, I_{zz} = yaw moment of inertia (about z -axis)

m_{curb} = curb mass of vehicle (unloaded)

m_{loaded} = loaded mass of vehicle (curb plus occupants and cargo)

L = total length of vehicle

b = maximum width of vehicle

K_G = geometric empirically determined constant (see **Figure 4**)

K_M = geometric empirically determined constant (see **Figure 4**)

Vehicle type	K_G	K_M	R^2
All combined	13.1	0.696	0.85
Passenger car	13.8	0.769	0.86
Light truck	13.4	0.750	0.92
SUV	12.2	0.656	0.76
Light van	12.3	0.642	0.90

Figure 4

Yaw moment of inertia empirical constants.

Consider the vehicle in **Figure 5**. The principal direction of force, PDOF, acting upon the centroid of the damaged frontal surface is angled from the residual deformation measurements, c_n^R , which are recorded parallel to the primary longitudinal axis, using the

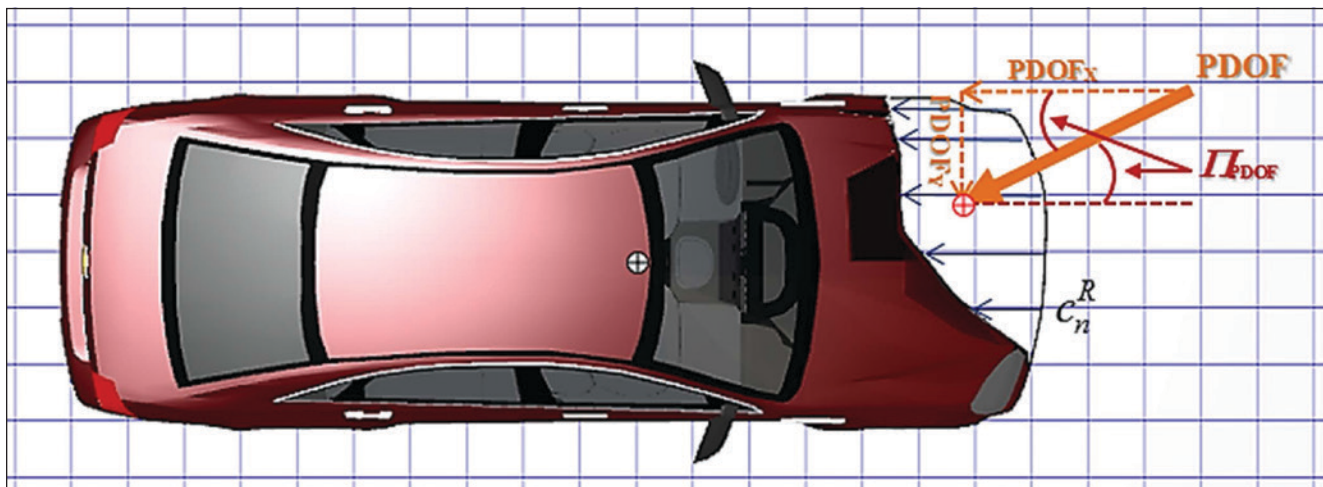


Figure 5

Oblique impact PDOF acting at damage centroid.

undamaged surface (in this case, front bumper) as the datum line to measure from for a frontal deformation profile. Therefore, using Equation 2 to determine the impact force only accounts for the longitudinal component of the force without accounting for the fact that the total collision force acts along the angle of the PDOF, Π^{PDOF} . Such an assumption may lead to a significant under-approximation of the total force acting upon the vehicle structure for an oblique impact.

Therefore, the total force of the impact, \mathbf{F}_{PDOF} , must be determined. The following derivation for \mathbf{F}_{PDOF} from Equation 2 results in the *Generalized Impact Force-Deflection Model*.

$$\begin{aligned} Fx &= F^{PDOF} \cdot \cos(\Pi^{PDOF}) \\ F^{PDOF} &= Fx \cdot \frac{1}{\cos(\Pi^{PDOF})} \\ F^{Gen} &= \sum_{j=0}^n \left(A_i + B_i \cdot \Delta c_j^R \right) \cdot \frac{\Delta w_j}{\cos(\Pi_i^{PDOF})} \end{aligned} \quad (11)$$

Where, A_i , B_i , Δc_j^R , Δw_j are as previously defined
 Π_i^{PDOF} = angle of the PDOF acting upon the i^{th} vehicle

The *Generalized Impact Force-Deflection Model* of Equation 11 provides the magnitude of the total external force acting upon the damage centroid of a vehicle during an oblique or offset impact. This is equal in magnitude but opposite in direction of application to the external force applied through the damage centroid for the opposing vehicle in accordance with Newton's third law. Equation 11 is a more complete and generalized statement of the *Central Impact Force-Deflection Model* stated by Equation 2, in that as Π_{PDOF} approaches 0 for Equation 11,

then $\mathbf{F}^{Gen} \rightarrow \sum_{j=0}^n \mathbf{F}_j^I$ of Equation 2. As a generalized equation, Equation 11 has broader application to a multitude of varying impact configurations that include central, collinear, offset, and oblique impacts.

The *Generalized Force-Deflection Model* provides the means by which the total force acting upon a vehicle during an impact is determined, regardless of whether the impact is a central or oblique collision event. Similar methods previously used in formulating the expression for the work necessary to deform the vehicle spring system (resulting from a central impact) are utilized when determining the work necessary to produce permanent deformation to the i^{th} vehicle (where $i=1..2$ for a two vehicle system) involved in an oblique or central impact event, when the deformation depth and width measurements for each vehicle are known or knowable. This results in the *Oblique Impact Work/Energy Model* represented by Equation 12.

$$\begin{aligned} \sum_{j=0}^n \int_0^{\Delta c_j^{total}} (F_{pdof}) \cdot d\Delta c_j^{total} &= \sum_{j=0}^n \left(\int_0^{\Delta c_j^{total}} \left((A_i + B_i \cdot \Delta c_j^R) \cdot \frac{\Delta w_j}{\cos(\Pi_{PDOF})} \right) \cdot d\Delta c_j^{total} \right) \\ \Delta c_j^{total} &= \frac{\Delta c_j^R}{\cos(\Pi_{PDOF})} \quad \text{Integrate then substitute value for total deformation} \\ \sum_{j=0}^n \int_0^{\Delta c_j^{total}} (F_{pdof}) \cdot d\Delta c_j^{total} &= \sum_{j=0}^n \left(A_i \cdot \Delta c_j^R + \frac{B_i \cdot (\Delta c_j^R)^2}{2} + \frac{A_i^2}{2 \cdot B_i} \right) \cdot \frac{\Delta w_j}{\cos(\Pi_{PDOF})^2} \end{aligned} \quad (12)$$

Work due to friction often results from oblique impacts where the corner or narrow "contact" region on a striking vehicle slides along the relative extended length of the "surface" on a struck vehicle so that the overall *contact*

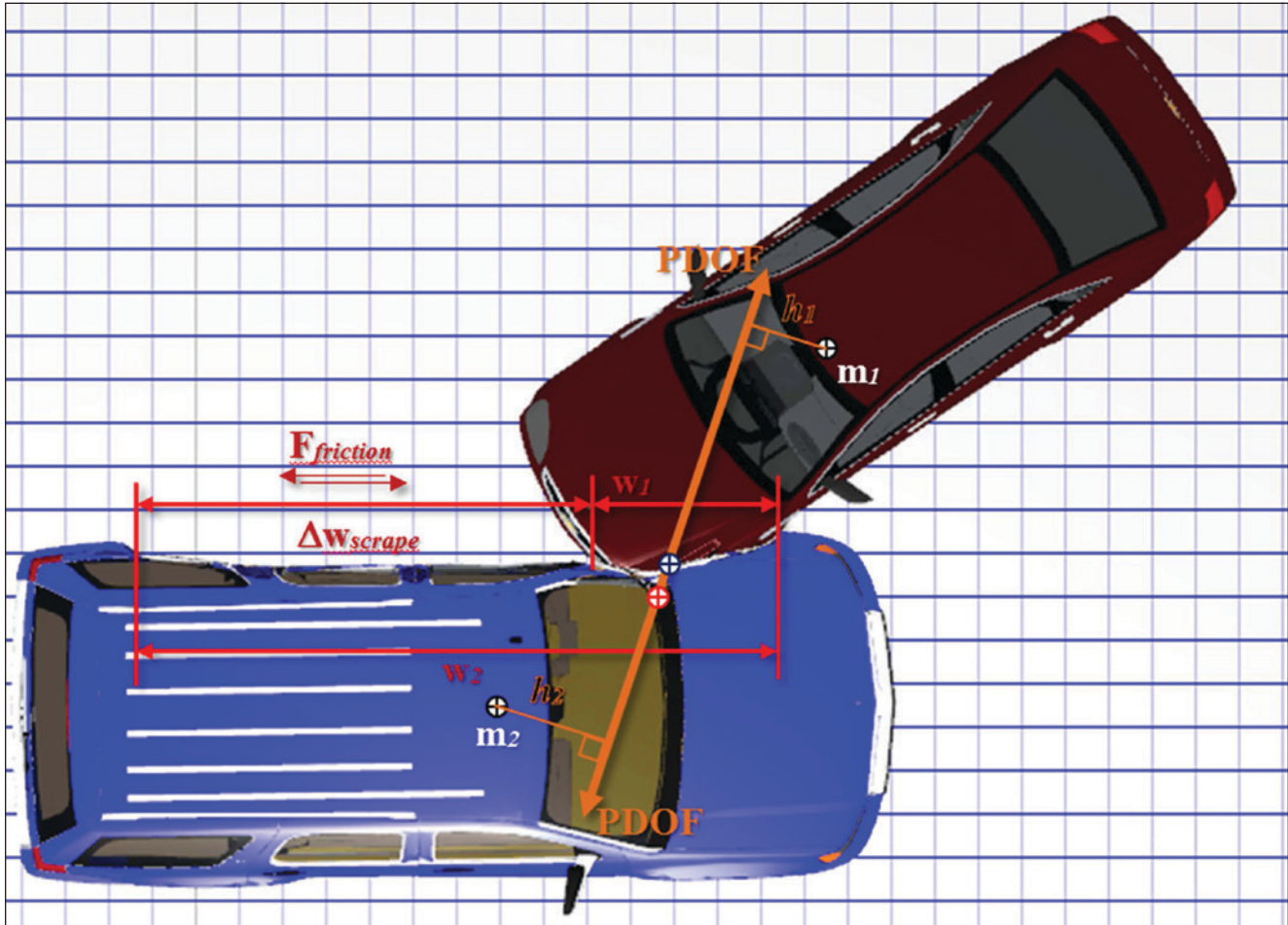


Figure 6
Friction of extended contact, scraping impacts.

and *surface* damage regions between the vehicles are dissimilar. The resultant *approach phase* force (due to impact determined in Equation 11) does not change as a result of the inter-vehicular friction between the two surfaces, since the frictional forces between the vehicles act at (or near) perpendicular to the applied impact force at maximum impulse, thus not contributing to the impulsive force of the impact. Therefore, inter-vehicular friction results in an extended tail of the impulse curve due to an extended contact time period between the vehicles during approach and separation. **Figure 6** demonstrates how to determine the net contact distance due to inter-vehicle friction.

Consider the contact between the two vehicles shown in **Figure 6**. The width of contact on the striking vehicle, m_1 , is concentrated on the left front corner, while the width of contact on the struck vehicle, m_2 , extends across a much broader width of contact, which is due to scraping between the vehicles during separation. The width of scraping may be difficult to directly

measure on each vehicle, but is easily and accurately approximated by the difference in contact widths.

$$\Delta w_{scrape} = w_2 - w_1 \tag{13}$$

The work done within the region of scraping is dissipated energy due to kinetic friction as the two surfaces slide against each other, as well as continued deformation resulting from an extended impact force impulse — until final separation occurs. Even though the inter-vehicular friction occurs during the separation phase of the impact, the additional inward deformation from separation should be considered as part of the deformation profile when calculating the total force and total work in Equations 11 and 12. The basic equation for kinetic friction between any two surfaces is as follows:

$$F^{friction} = \mu_k \cdot F^{Normal} \tag{14}$$

Where, μ_k = coefficient of kinetic friction

F^{Normal} = normal force acting between two sliding surfaces

Because the force due to friction is acting between the two sliding vehicle surfaces while in contact, the friction force acting upon m_1 must be equal in magnitude but opposite in application to the friction force acting upon m_2 .

$$\begin{aligned} m_1 \cdot a_1 \cdot \mu_k &= m_2 \cdot a_2 \cdot \mu_k \\ m_1 \cdot g \cdot n_1 \cdot \mu_k &= m_2 \cdot g \cdot n_2 \cdot \mu_k \\ m_1 \cdot g \cdot \left(\frac{m_2}{m_1 + m_2} \right) \cdot \mu_k &= m_2 \cdot g \cdot \left(\frac{m_1}{m_1 + m_2} \right) \cdot \mu_k \end{aligned} \quad (15)$$

$$F_2^{friction} = m_2 \cdot g \cdot \left(\frac{m_1}{m_1 + m_2} \right) \cdot \mu_k \quad (16)$$

The work done due to friction is the integral of the force over the work distance, Δw_{scrape} , which results in the additional work due to friction that must be accounted for during the approach phase of the collision.

$$\begin{aligned} \int_0^{w_1} F_1^{Friction} \cdot dw_1 &= \int_0^{w_1} \left(m_1 \cdot g \cdot \mu_k \cdot \left(\frac{m_2}{m_1 + m_2} \right) \right) \cdot d\Delta w_{scrape} \\ \int_0^{\Delta w_{scrape}} F_2^{Friction} \cdot dw_2 &= \int_0^{\Delta w_{scrape}} \left(m_2 \cdot g \cdot \mu_k \cdot \left(\frac{m_1}{m_1 + m_2} \right) \right) \cdot d\Delta w_{scrape} \end{aligned}$$

$$E_1^{friction} = m_1 \cdot g \cdot \mu_k \cdot \left(\frac{m_2}{m_1 + m_2} \right) \cdot \Delta w_{scrape} \quad (17)$$

$$E_2^{friction} = m_2 \cdot g \cdot \mu_k \cdot \left(\frac{m_1}{m_1 + m_2} \right) \cdot \Delta w_{scrape} \quad (18)$$

Studies have reported the coefficient of kinetic friction for vehicle-to-vehicle contact ranges between $0.3 \leq \mu_k \leq 1.1$, depending upon the angle of impact^{14,15}. The highest friction levels were associated with impacts nearing parallel approach angles at contact (sideswipe), while the lower friction levels were associated with oblique impacts. By inspection of Equations 17 and 18, frictional effects may be a significant consideration for impacts that produce large discrepancies between the damage widths of the vehicles. Additionally, the longer the vehicles remain in contact during the approach velocity change phase, the longer the external tire/surface impulse affects the overall velocity change levels for both vehicles. Therefore, the consideration of work due to friction (if evidence of sliding is present) should provide a more accurate analysis of the collision event.

The development of the oblique impact and friction work equations allow for a more generalized analysis of work to cause deformation. A complete generalized model should account for the effects of an oblique collision upon the residual damage approximations across the damage width as well as the contributions of friction between sliding surfaces in contact during the approach phase of the impact. The total work done on the system is the sum of the work during the approach and departure velocity change phases, which are defined here as the *Generalized Impact Work/Energy Model* of Equations 19 and 20.

$$\begin{aligned} E_1^{Gen} &= E_1^{Oblique} + E_1^{friction} \\ &= \sum_{j=0}^n \left(A_1 \cdot \Delta c1_j^R + \frac{B_1 \cdot (\Delta c1_j^R)^2}{2} + \frac{A_1^2}{2 \cdot B_1} \right) \cdot \Delta w1_j \cdot (1 + \tan^2(\Pi_{PDOF1})) + m_1 \cdot g \cdot \mu_k \cdot \left(\frac{m_2}{m_1 + m_2} \right) \cdot \Delta w_{scrape} \end{aligned} \quad (19)$$

$$\begin{aligned} E_2^{Gen} &= E_2^{Oblique} + E_2^{friction} \\ &= \sum_{j=0}^n \left(A_2 \cdot \Delta c2_j^R + \frac{B_2 \cdot (\Delta c2_j^R)^2}{2} + \frac{A_2^2}{2 \cdot B_2} \right) \cdot \Delta w2_j \cdot (1 + \tan^2(\Pi_{PDOF2})) + m_2 \cdot g \cdot \mu_k \cdot \left(\frac{m_1}{m_1 + m_2} \right) \cdot \Delta w_{scrape} \end{aligned} \quad (20)$$

Figure 6 showed an oblique collision between two vehicles and the moment arms, h_1 and h_2 , for the torque applied to vehicles 1 and 2, respectively. The torque applied to each vehicle is given by Equation 21, and Newton's second law states that the sum of the torques for a conservative system (which impact impulse is identified as a conservative contribution to the system) must be equal to zero. Equation 9 also provided an important relationship between the yaw moment of inertia of a vehicle about the primary vertical axis, I_{zz} , and the radius of gyration of the effective mass as it rotates around the primary vertical axis.

$$\tau = r \times F_i = h \cdot F^{magnitude} = I_{cm} \ddot{\phi} \quad (21)$$

$$I_{zz} = m \cdot k^2 \quad (\text{restatement of Equation 9})$$

Where, τ = torque

r = vector from point of rotation to applied force

F_i = applied force vector from collision

$F_{magnitude}$ = magnitude of applied force

I_{cm} = polar mass moment of inertia (about axis through mass center)

$\ddot{\phi}$ = rotational acceleration

h_i = perpendicular moment arm for impact induced moment

k = radius of gyration about principle axis of rotation

m = mass of vehicle

Additionally, the acceleration at the damage centroid of each vehicle, or common velocity point, between the vehicles has the following relationships with respect to each vehicle:

$$\text{Vehicle 1:} \quad a1_{common} = a1_{cm} + h_1 \cdot \ddot{\phi}_1$$

$$\ddot{\phi}_1 = \frac{a1_{common} - a1_{cm}}{h_1}$$

Vehicle 2:

$$a2_{common} = a2_{cm} + h_2 \cdot \ddot{\phi}_2$$

$$\ddot{\phi}_2 = \frac{a2_{common} - a2_{cm}}{h_2}$$

The rotational acceleration of each vehicle produced by the force couple can be related in the following manner.

Vehicle 1:

$$F^{Gen} \cdot h_1 = I1_{zz} \cdot \ddot{\phi}_1$$

$$h_1 \cdot m_1 \cdot a1_{cm} = m_1 \cdot k1_g^2 \cdot \left(\frac{a1_{common} - a1_{cm}}{h_1} \right)$$

Vehicle 2:

$$F^{Gen} \cdot h_2 = I2_{zz} \cdot \ddot{\phi}_2$$

$$h_2 \cdot m_2 \cdot a2_{cm} = m_2 \cdot k2_g^2 \cdot \left(\frac{a2_{common} - a2_{cm}}{h_2} \right)$$

Grouping like terms allows for the solution for the force at the center of mass with respect to the radius of gyration and moment arm of the force applied at the common point of contact between the vehicles.

Vehicle 1:

$$h_1^2 \cdot (m_1 \cdot a1_{cm}) = m_1 \cdot k1_g^2 \cdot (a1_{common} - a1_{cm})$$

$$m_1 \cdot a1_{cm} \cdot (k1_g^2 + h_1^2) = m_1 \cdot a1_{common} \cdot k1_g^2$$

$$m_1 \cdot a1_{cm} = \left(\frac{k1_g^2}{k1_g^2 + h_1^2} \right) \cdot m_1 \cdot a1_{common}$$

Vehicle 2:

$$h_2^2 \cdot (m_2 \cdot a2_{cm}) = m_2 \cdot k2_g^2 \cdot (a2_{common} - a2_{cm})$$

$$m_2 \cdot a2_{cm} \cdot (k2_g^2 + h_2^2) = m_2 \cdot a2_{common} \cdot k2_g^2$$

$$m_2 \cdot a2_{cm} = \left(\frac{k2_g^2}{k2_g^2 + h_2^2} \right) \cdot m_2 \cdot a2_{common}$$

Substitute Equation 9 for the radius of gyration for each vehicle:

Vehicle 1:

$$m_1 \cdot a1_{cm} = \left(\frac{\frac{I1_{zz}}{m_1}}{\frac{I1_{zz}}{m_1} + h_1^2} \right) \cdot m_1 \cdot a1_{common}$$

$$\text{Where, } \gamma_1 = \left(\frac{I1_{zz}}{I1_{zz} + m_1 \cdot h_1^2} \right)$$

$$F1_{cm} = (m_1 \cdot \gamma_1) \cdot \frac{\Delta v1_{common}}{\Delta t}$$

Vehicle 2:

$$m_2 \cdot a2_{cm} = \left(\frac{\frac{I2_{zz}}{m_2}}{\frac{I2_{zz}}{m_2} + h_2^2} \right) \cdot m_2 \cdot a2_{common}$$

$$\text{Where, } \gamma_2 = \left(\frac{I2_{zz}}{I2_{zz} + m_2 \cdot h_2^2} \right)$$

$$F2_{cm} = (m_2 \cdot \gamma_2) \cdot \frac{\Delta v2_{common}}{\Delta t}$$

Vehicle 1 total momentum change:

$$F1_{cm} \cdot \Delta t = \Delta p_1 = (m_1 \cdot \gamma_1) \cdot \Delta v1_{common}$$

Vehicle 2 total momentum change:

$$F2_{cm} \cdot \Delta t = \Delta p_2 = (m_2 \cdot \gamma_2) \cdot \Delta v2_{common}$$

The values of γ_1 and γ_2 are defined here as the *effective rotational (dynamic) mass ratio* for vehicle 1 and vehicle 2, respectively. The above final equation simply states that the total change in momentum for each vehicle is equivalent to the velocity change at the point of common contact between the vehicles times the *effective rotational mass ratio* produced by the oblique impact. The culmination of the consideration of restitution, tire forces, friction and rotational contributions to the collision leads to the *Generalized Impact Force-Deflection Velocity Change Model*, which determines the *total velocity change* magnitudes for each of the vehicles as follows:

$$\Delta V_1^{Gen} = (1+e) \sqrt{\frac{2 \cdot m_2 \cdot \gamma_2 \cdot (E_1^{Gen} + E_2^{Gen})}{m_1 \cdot \gamma_1 \cdot (m_1 \cdot \gamma_1 + m_2 \cdot \gamma_2)}} + \frac{m_2 \cdot (g \cdot \mu \cdot n) \cdot \Delta t}{m_1} \quad (22)$$

$$\Delta V_2^{Gen} = (1+e) \sqrt{\frac{2 \cdot m_1 \cdot \gamma_1 \cdot (E_1^{Gen} + E_2^{Gen})}{m_2 \cdot \gamma_2 \cdot (m_1 \cdot \gamma_1 + m_2 \cdot \gamma_2)}} - (g \cdot \mu \cdot n) \cdot \Delta t \quad (23)$$

Where, e = coefficient of restitution for collision level

γ_1 and γ_2 = effective rotational (dynamic) mass ratios

μ = roadway coefficient of friction

n = braking efficiency and/or brake force distribution as a decimal ($0 \leq n \leq 1.0$)

Δt = impulse time period during approach velocity change

E_1^{Gen} and E_2^{Gen} = the total work determined by Equations 19 and 20

Solving for the impulse time period when considering the impact force, rotational effects and all external forces acting upon the system results in Equation 24.

$$\Delta t^{Gen} = \sqrt{\left(\frac{2 \cdot m_1 \cdot \gamma_1 \cdot m_2 \cdot \gamma_2}{(m_1 \cdot \gamma_1 + m_2 \cdot \gamma_2)} \right) \cdot \frac{(E_1^{Gen} + E_2^{Gen})}{(F^{Gen})^2}} \quad (24)$$

Inspection of Equation 22 through Equation 24 reveals that in the absence of inter-vehicle friction, tire forces and rotation, each of these equations reduce to their parent forms developed in the original CRASH-type programs.

Missing Damage Dimensions

The *Generalized Force-Deflection Model* and the *Generalized Impact Work/Energy Model* in their present form (as derived in this paper) require knowledge of structural A and B stiffness coefficients and measured deformation profiles, Δc^R and Δw , for both vehicles. However, the Newton's third law expression for the impact using Equation 11 considers the total force acting equal and opposite between the vehicles during an oblique collision, resulting in the ability to predict the damage profile deformation depths of a vehicle if the structural stiffness values for both colliding vehicles and the damage profile of at least one vehicle in the impact are known. This results in Equation 25, hereto defined as the *Generalized Newtonian Deformation*

Prediction Model:

$$F_{known}^{Gen} = F_{unknown}^{Gen}$$

$$\Delta C_{unknown}^{Gen} = \frac{\frac{F_{known}^{Gen}}{\Delta W_{unknown}} - A_{unknown}}{B_{unknown}} \quad (25)$$

Where, F_{known}^{Gen} = generalized peak force calculated for the vehicle of known deformation

$F_{unknown}^{Gen}$ = generalized peak force for vehicle of unknown deformation by Newton's third law

$C_{unknown}^{Gen}$ = Newtonian predicted generalized deformation for vehicle of unknown deformation

$w_{unknown}$ = total deformation width for the vehicle of unknown deformation depth (quantity must be known or knowable)

$A_{unknown}$ and $B_{unknown}$ = structural stiffness values for vehicle of unknown deformation depth (these values must be known or knowable)

Equation 25 can be used in two different manners. First, if piece-wise measurements (individual sections measured for width and depth) of a damaged vehicle profile can be associated with distinct piece-wise segments of the vehicle with unknown deformation depth but known deformation width, the actual profile of the "unknown" vehicle can be predicted. This is useful for simulations where having a realistic damage profile prediction that can be compared to general diagrams or photographs is useful in solving the collision solution. Secondly, the weighted average deformation depth (average of depth as though distributed across the entire damage width) of the vehicle of unknown deformation depth can be determined over the known or knowable damage width, which will result in the same work done on the system, but will not produce a piecewise damage profile.

Missing Structural Stiffness Coefficients

The *Generalized Force-Deflection Model* provides the means by which the net generalized force of any generalized impact can be determined, and

the measureable deformation profile to a vehicle with PDOF considerations provides the distance over which the net generalized force is applied. This basic concept is an expression of work/energy principles, in that the distance over which a force is applied to the system is equivalent to the total work done on the system.

$$\int F^{Gen} dx = E_{work}^{Gen}$$

Where, F^{Gen} is the generalized force magnitude applied at peak impulse, and dx is the differential distance over which the work on the system occurs

Consider a collision involving two vehicles where the damage profile of each vehicle has been measured or can be determined from photographic documentation. Unlike the application of the equations previously presented, this collision event has only one vehicle that has a known or knowable structural stiffness characteristic (A and B stiffness values), and the other associated vehicle or object does not have known or knowable structural stiffness values. If the weighted average damage for the vehicle of unknown structural stiffness is determinable, then by applying work/energy principles to a generalized vehicle-to-vehicle collision, a generalized expression for the work on the vehicle of unknown structural stiffness characteristics can be determined by Equation 26.

$$\sum_{j=0}^n F_j^{Gen} = \sum_{j=0}^n (A^{known} + B^{known} \cdot \Delta C_j^R) \cdot \frac{\Delta W_j}{\cos(\Pi^{known})}$$

$$(E_{work}^{Gen})^{unknown} = (F^{Gen})^{known} \cdot (\bar{C}^{unknown}) \cdot (1 + \tan^2(\Pi^{unknown})) \quad (26)$$

Where, $(E_{work}^{Gen})^{unknown}$ = Generalized work on vehicle with unknown structural stiffness values

$(F^{Gen})^{known}$ = Generalized force applied to the vehicle of known A/B values

$\bar{C}^{unknown}$ = Weighted average deformation on vehicle of unknown A/B values

The weighted average deformation depth on the vehicle with unknown A/B stiffness values is calculated from the measured damage profile using Equation 27.

$$\bar{c}^{unknown} = \frac{\sum_{j=1}^n \Delta w_j \cdot \Delta c_j}{\sum_{j=1}^n \Delta w_j} \quad (27)$$

In fact, by applying Equation 26 in all cases, even when both structural stiffness values are known or knowable, the collision is forced to comply with Newton's third law, and a more accurate solution is produced, which will be demonstrated in the following section where these principles were applied to the RICSAC (Research Input for Computer Simulation of Automobile Collisions) staged collisions¹⁶. Equations 11, 17 through 20, and 22 through 27 make up the *Generalized Deformation and Total Velocity Change Analysis System of Equations*, or **G-DaTA ΔV^{TM}** .

Application of Methodology to RICSAC Staged Collisions

Equation 26 has no "vehicle type-specific" conditions or restrictions for its application of unknown structural stiffness values. In other words, the generalized form of Equation 26 has far-reaching and broader application beyond passenger vehicles, light trucks, vans, and SUVs, with the application to commercial vehicles, motorcycles, and even objects provided the damage profile and weighted average deformation can be determined.

By using Equation 26 for evaluating the generalized work done on any two-vehicle or vehicle-to-object collision system, the analysis of impacts with vehicles of unknown stiffness (due to the lack of testing, lack of model year overlap, or lack of adequate information regarding structural characteristics) is no longer a limiting factor. As long as one of the vehicle

surfaces involved in an impact has known or knowable structural stiffness characteristics, any vehicle or object of unknown structural characteristics but known or knowable deformation profile can be analyzed using the deformation analysis methods presented. Additionally, as will be demonstrated through applying these principles to the 12 RICSAC tests, using these generalized models and only the stiffness coefficients for the frontal impacting vehicle (frontal A/B values only) and applying Equation 26 for the determination of work on the non-frontal impact vehicle (broadside or rear, or even by choosing one vehicle only in the head-on offset impacts) provides the best correlation of results.

The generalized models developed as summarized in this paper were tested against the 12 collisions as part of the RICSAC validation study that is used for the validation of computer models for collision analysis. The proper coordinate transformations of the accelerometer data as outlined in follow-on studies were also considered in order to ensure that the most accurate data for analysis was utilized¹⁷. **Figure 7 and Figure 8** shows the results and statistical analysis of the study using the generalized methods presented in this paper as compared to the RICSAC testing. Additionally, **Figure 9 and Figure 10** show the plots of the data fit, all of which fit within a $\pm 10\%$ boundary using the generalized models.

The results of the testing show a high degree of correlation between the models developed and presented by this author to the RICSAC testing — much higher than has been achieved with any other known model to date. These results demonstrate that by carefully considering restitution, tire-ground forces, inter-vehicular friction, and rotational effects from off-set and/or oblique impacts, accurate and precise velocity change determinations for collisions can be made while considering only the structural stiffness characteristics of one vehicle.

RICSAC Test/Veh	ΔVx (kph)	ΔVy (kph)	ΔVy (mph)	PDOF (degrees)	RICSAC Test ΔVtotal (kph)	RICSAC Test ΔVtotal (mph)	RICSAC Test ΔVtotal (mph)	RESULTS PIECEWISE DVtotal (mph)	Absolute Difference (mph)	Percent Difference (Calc-Test)	RESULTS AVERAGE DVtotal (mph)	Absolute Diff (mph)	Percent Difference (Calc-Test)	e rest.	h feet	ΔWscrape inches	% tire forces
1-V1	-18.2	7.7	4.8	-22.9	19.8	12.3	12.3	12.3	0.1	0.6%	12.3	0.0	0.2%	0.05	1.0	35.9	75%
1-V2	25.7	-8.5	-5.3	-18.3	27.1	16.9	16.3	16.3	-0.6	-3.7%	16.2	-0.7	-4.0%		0.8		
2-V1	-27.8	14.1	8.8	-26.8	31.2	19.5	19.9	19.9	0.4	2.1%	19.8	0.3	1.4%	0.00	1.1	41.7	75%
2-V2	-30.1	-18.8	-17.7	43.3	41.3	25.8	26.0	26.0	0.2	0.6%	25.8	0.0	-0.2%		0.8		
3-V1	-15.3	-1.1	-0.7	4.1	15.3	9.5	9.3	9.3	-0.3	-2.8%	10.5	0.9	8.9%	0.20	1.0	0	10%
3-V2	25.1	3.5	2.5	7.9	25.3	15.8	15.3	15.3	-0.5	-3.0%	17.3	1.5	8.7%		1.2		
4-V1	-30.1	-18.7	-0.5	1.0	30.1	18.7	17.4	17.4	-1.3	-7.7%	19.1	0.4	2.2%	0.00	1.6	0	75%
4-V2	35.7	22.2	1.0	1.6	35.7	22.2	22.1	22.1	-0.1	-0.5%	24.3	2.1	8.7%		0.0		
5-V1	-26.1	-16.2	-0.2	0.4	26.1	16.2	16.4	16.4	0.2	1.0%	16.2	0.0	-0.1%	0.05	2.4	0	75%
5-V2	41.0	25.5	2.4	3.4	41.1	25.5	25.4	25.4	-0.2	-0.8%	25.1	-0.4	-1.8%		1.4		
6-V1	-14.2	-8.8	3.9	-15.4	14.7	9.1	9.5	9.5	0.3	3.7%	9.3	0.2	2.2%	0.00	1.0	33.2	50%
6-V2	22.0	13.7	-6.8	-17.2	23.0	14.3	14.2	14.2	-0.1	-0.6%	14.0	-0.3	-2.1%		1.1		
7-V1	-18.8	-11.7	4.0	-12.0	19.2	12.0	12.2	12.2	0.3	2.1%	12.9	1.0	7.5%	0.00	1.4	31.7	50%
7-V2	31.4	19.5	-5.6	-10.1	31.9	19.8	18.3	18.3	-1.5	-8.5%	19.3	-0.5	-2.4%		2.1		
8-V1	-21.6	-13.4	10.6	-26.1	24.1	14.9	15.1	15.1	0.1	0.8%	15.2	0.3	1.8%	0.05	3.2	8.5	50%
8-V2	13.2	8.2	-11.9	-42.0	17.8	11.0	11.4	11.4	0.3	2.9%	11.5	0.5	4.0%		2.6		
9-V1	-29.0	-18.0	13.7	-25.3	32.1	19.9	20.8	20.8	0.9	4.5%	20.9	1.0	4.8%	0.10	0.9	0	50%
9-V2	11.1	6.9	-7.1	-32.6	13.2	8.2	8.3	8.3	0.1	1.1%	8.3	0.1	1.5%		0.9		
10-V1	-46.3	-28.8	29.1	-32.1	54.7	34.0	34.8	34.8	0.8	2.2%	34.4	0.4	1.2%	0.20	2.3	0	50%
10-V2	15.9	9.9	-12.4	-37.9	20.2	12.5	12.4	12.4	-0.1	-1.2%	12.3	-0.3	-2.2%		2.0		
11-V1	-39.3	-24.4	2.6	-3.8	39.4	24.5	25.0	25.0	0.5	2.2%	24.8	0.4	1.5%	0.00	1.1	0	0%
11-V2	25.3	15.7	0.8	1.8	25.3	15.7	16.4	16.4	0.7	4.4%	16.3	0.6	3.8%		1.0		
12-V1	-65.7	-40.8	-1.3	1.1	65.7	40.8	44.7	44.7	3.9	8.6%	43.8	3.0	6.9%	0.00	1.1	0	0%
12-V2	43.0	26.7	-2.4	-3.2	43.1	26.7	29.7	29.7	2.9	9.9%	29.1	2.4	8.2%		1.1		

Figure 7
Summary of results for generalized model application to RICSAC testing.

Piecwise Matching Method			Weighted Average Method		
χ^2 Test of fit	1.07	standard deviation of error	χ^2 Test of fit	1.09	standard deviation of error
χ^2 critical => ($\alpha=0.01$)	10.2 (n=23)	± 1.1 mph	χ^2 critical => ($\alpha=0.01$)	10.2 (n=23)	± 0.9 mph
R^2 =>	0.989	$\pm 4.1\%$	R^2 =>	0.990	$\pm 3.9\%$
T-test => ($\alpha = 0.99$)	0.24		T-test => ($\alpha = 0.99$)	0.01	
critical=>	2.5		critical=>	2.5	
F-test => ($\alpha = 0.99$)	0.69		F-test => ($\alpha = 0.99$)	0.79	
critical=>	2.26		critical=>	2.26	

Figure 8
Statistical analysis of generalized models compared to RICSAC results.

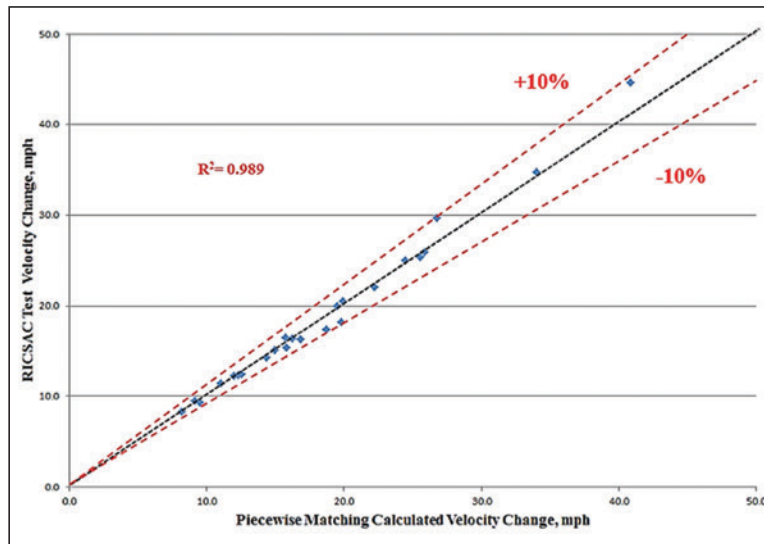


Figure 9
Results using Equation 26 for piecewise damage matching between vehicles.

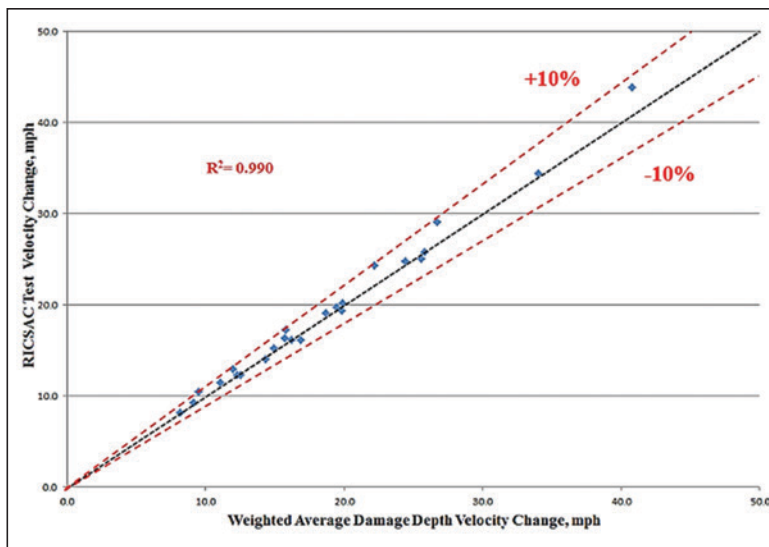


Figure 10
Results using Equation 26 for weighted average damage application.

G-DaTA ΔV^{TM} Analysis Procedure

Application of the **G-DaTA ΔV^{TM}** system of equations starts with the documentation and measurement of vehicle deformation profiles for each vehicle into the form demonstrated in **Figure 1**. After tabulating the deformation profiles for the numerical analysis, the following general analytical steps provide the *Total Velocity Change* for two colliding vehicles:

- 1) Obtain vehicle weights, dimensions and determine inertial properties (Equation 10).
- 2) Determine the PDOF acting upon each vehicle (which will be directly opposite in direction when the vehicles are placed together at initial contact or maximum engagement; **Figure 6**).
- 3) Obtain vehicle A/B stiffness values for the selected vehicle in determining the *Generalized Force* acting equal and opposite between the colliding vehicles (Equation 11) based upon the following hierarchy:
 - a) If both colliding vehicles have frontal stiffness values available, choose the A/B stiffness value for the vehicle with the greatest extent of measured damage (damage width and depth profile).
 - b) Frontal A/B stiffness for vehicle with frontal impact damage for oblique side, broadside and rear-end impact configurations.
 - c) A/B stiffness by vehicle struck surface (front, rear or side) if only one vehicle has an impact surface that is supported by test data regardless of impact configuration.
 - d) If neither vehicle impact surface is supported, use a range of A/B stiffness factors for similar vehicles to establish a higher and lower bounding for the analysis.
- 4) Determine the work due to the non-conservative friction forces (Equations 17 and 18).
- 5) Determine the weighted average deformation depth for the vehicle which is not supported by A/B stiffness data or where A/B stiffness data was not used (Equation 27).
- 6) Determine the *Generalized Work* to produce compression of the vehicle structures in the form of permanent deformation (Equations 19 and 26).
- 7) Determine the time period to reach maximum impulse (Equation 24).
- 8) Determine the roadway friction (μ) and equivalent braking efficiency (n) for the vehicle whose tires act against the direction of impact force application (struck vehicle).
- 9) Determine an appropriate coefficient of restitution for the impact. The following are general rules for determining appropriate coefficients of restitution:
 - e) Minor impacts with minor damage will have higher restitution values (see references 6 and 7).
 - f) Even with extensive permanent damage profiles, ranging restitution between 0 and 0.1 may provide a greater confidence interval in the analysis results.
 - g) When the impact involves an axle and/or wheel of a struck vehicle in an oblique side or broadside impact, restitution will range from 0.2 to 0.4 to account for the hardened zone of the axle and/or the “bounce” effect of impacting an inflated tire (see **Figure 7**).
- 10) Determine the *Total Velocity Change* for the vehicles produced by the impact event (Equations 22 and 23).

Outside of accurate deformation profile measurements, Step 3 is perhaps the most crucial step in the application of the **G-DaTA ΔV^{TM}** system of equations. The determination of the *Generalized Force* of the impact is completed for only one vehicle, not for both, since by Newton’s third law the *Generalized Force* acting upon both vehicles is equal in magnitude but opposite in direction of application. If reliable stiffness data is available for both colliding vehicles and for the appropriate colliding surfaces (front, rear or side), then the determination of the *Total Velocity Change* for each vehicle can be calculated by applying the **G-DaTA ΔV^{TM}** system of equations twice and comparing results as a useful crosscheck or for providing a reasonable confidence interval for the analysis.

The following example of the application of the **G-DaTA ΔV^{TM}** system of equations is taken from RICSAC 6 staged collision involving the front of a 1974 Chevrolet Malibu (Vehicle 1, m_1) colliding with the right front side of a 1975 Volkswagen Rabbit (Vehicle 2, m_2) in an oblique off-set side impact. The impact velocity for both vehicles was recorded at 21.5 mph. The Chevrolet test weight was 4,310 pounds,

and the Volkswagen test weight was 2,640 pounds. Each vehicle contained two 49CFR Part 572 50th percentile anthropomorphic test devices (ATD). The ATDs in the Volkswagen were instrumented while the ATDs in the Chevrolet were un-instrumented during the collision. Data and results from this impact test are listed below.

Variables for the analysis were obtained from reported mass and deformation profiles, and data extrapolated from the collision diagram of **Figure 11** from the damage profiles matched at maximum engagement. As stiffness data was unavailable for the 1974 Chevrolet Malibu, the A and B structural stiffness data was

obtained with permission from Neptune Engineering NEI Data Store for the similar 1970 Chevrolet Malibu four-door sedan. The **G-DaTA** ΔV^{TM} system of equations were set up and analysis completed using PTC[®] MathCAD Prime 3.0.

The following are calculation results using the weighted average deformation depth analysis of Equation 27 applied to the VW Rabbit, the frontal stiffness A/B values for the Chevrolet Malibu for determining the *Generalized Force* using Equation 11 and the forced Newton's third law compliance for determining the *Generalized Work* of the vehicle without A/B stiffness values using Equation 26.

TEST RESULTS AND RECORDED VALUES:

$$\Delta v_{1_{test}} := -14.7 \text{ kph} = -9.134 \text{ mph} \quad \Delta t_{peak} := 0.095 \cdot \text{sec}$$

$$\Delta v_{2_{test}} := 23.0 \cdot \text{kph} = 14.292 \text{ mph}$$

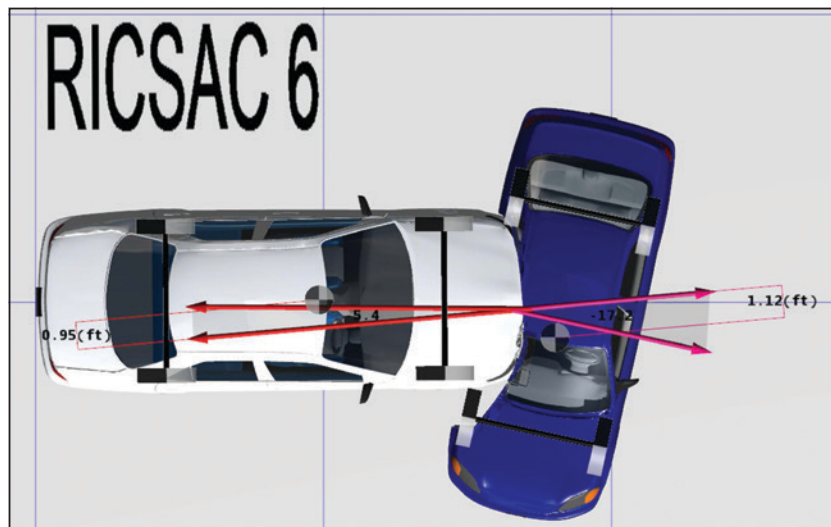


Figure 11
Maximum engagement PDOF diagram for RICSAC 6.

RICSAC 6: Measurements from scale damage sketches at same number of intervals

C1 := $\begin{bmatrix} 0.0 \\ 0.5 \\ 0.5 \\ 1.25 \\ 1.5 \\ 1.75 \\ 2.25 \\ 0 \end{bmatrix} \cdot \text{in}$

W1 := $\begin{bmatrix} 0.0 \\ 22.3 \\ 33.2 \\ 44.1 \\ 55.5 \\ 65.9 \\ 76.8 \\ 76.8 \end{bmatrix} \cdot \text{in}$

$m_1 := \frac{4310 \cdot \text{lb}}{g} = 133.96 \frac{\text{lb} \cdot \text{s}^2}{\text{ft}}$ 1974 Chev. Malibu 4DR

$I_{1zz} := \frac{m_1}{13.8} \cdot ((17.5 \cdot \text{ft})^2 + (6.42 \cdot \text{ft})^2) \cdot (0.769) = (2.59 \cdot 10^3) \text{ lb} \cdot \text{ft} \cdot \text{s}^2$

$A1 := 182 \cdot \frac{\text{lb}}{\text{in}}$ $B1 := 40 \cdot \frac{\text{lb}}{\text{in}^2}$ $h_1 := 1.0 \cdot \text{ft}$

$\Pi_{PDOF1} := -5.4 \cdot \text{deg}$ $\gamma_1 := \frac{I_{1zz}}{I_{1zz} + m_1 \cdot h_1^2}$

C2 := $\begin{bmatrix} 0 \\ 4.0 \\ 12.0 \\ 17.9 \\ 21.5 \\ 17.0 \\ 8.25 \\ 0 \end{bmatrix} \cdot \text{in}$

W2 := $\begin{bmatrix} 0 \\ 25.4 \\ 40.8 \\ 56.2 \\ 71.6 \\ 87.0 \\ 110.0 \\ 110.0 \end{bmatrix} \cdot \text{in}$

$m_2 := \frac{2640 \cdot \text{lb}}{g} = 82.05 \frac{\text{lb} \cdot \text{s}^2}{\text{ft}}$ 1975 Volkswagen Rabbit 2DR

$I_{2zz} := \frac{m_2}{13.8} \cdot ((14.25 \cdot \text{ft})^2 + (5.75 \cdot \text{ft})^2) \cdot (0.769) = (1.08 \cdot 10^3) \text{ lb} \cdot \text{ft} \cdot \text{s}^2$

$\Pi_{PDOF2} := (-17.2) \cdot \text{deg}$ $h_2 := 1.1 \cdot \text{ft}$

$e := 0.05$ $i := 0..6$ $\gamma_2 := \frac{I_{2zz}}{I_{2zz} + m_2 \cdot h_2^2}$

C2_bar := $\frac{\sum_{i=1}^6 (W2_{i+1} - W2_i) \cdot \left(\frac{C2_i + C2_{i+1}}{2}\right)}{W2_6} = 11.306 \text{ in}$ weighted average deformation

$\Delta W_{\text{scrape}} := W2_6 - W1_6 = 33.2 \text{ in}$ scraping distance on vehicle 2

$\mu_k := 0.5$ scraping friction coefficient

$\mu_r := 0.87$ surface friction coefficient

$n_2 := 50\%$ brake efficiency (broadside spin)

$F1 := \sum_{i=0}^6 \left(A1 + B1 \cdot \left(\frac{C1_i + C1_{i+1}}{2} \right) \right) \cdot (W1_{(i+1)} - W1_{(i)}) \cdot \left(\frac{1}{\cos(\Pi_{PDOF1})} \right) = (1.705 \cdot 10^4) \text{ lb}$

$F_i := \left(A1 + B1 \cdot \left(\frac{C1_i + C1_{i+1}}{2} \right) \right) \cdot (W1_{i+1} - W1_i) \cdot \left(\frac{1}{\cos(\Pi_{PDOF1})} \right)$

$F = \begin{bmatrix} 4.301 \cdot 10^3 \\ 2.212 \cdot 10^3 \\ 2.376 \cdot 10^3 \\ 2.714 \cdot 10^3 \\ 2.58 \cdot 10^3 \\ 2.869 \cdot 10^3 \\ 0 \end{bmatrix} \text{ lb}$

Weighted Average Deformation Depth Analysis:

$E2 := F1 \cdot C2_bar \cdot (1 + \tan(\Pi_{PDOF2}))^2 = (1.76 \cdot 10^4) \text{ lb} \cdot \text{ft}$

$E1_{Gen} := E1 + E1_{friction} = (6.031 \cdot 10^3) \text{ lb} \cdot \text{ft}$

$E2_{Gen} := E2 + E2_{friction} = (1.987 \cdot 10^4) \text{ lb} \cdot \text{ft}$

$\Delta t_{peak} := \sqrt{\left(\frac{2 \cdot m_1 \cdot \gamma_1 \cdot m_2 \cdot \gamma_2}{m_1 \cdot \gamma_1 + m_2 \cdot \gamma_2} \right) \cdot \frac{E1_{Gen} + E2_{Gen}}{F1^2}}$ $\Delta t_{peak} = 0.0918 \text{ s}$

$\Delta V1 := -(1+e) \cdot \sqrt{\left(\frac{2 \cdot m_2 \cdot \gamma_2 \cdot (E1_{Gen} + E2_{Gen})}{m_1 \cdot \gamma_1 \cdot (m_1 \cdot \gamma_1 + m_2 \cdot \gamma_2)} \right)} - \frac{m_2 \cdot (g \cdot \mu_r \cdot n_2) \cdot \Delta t_{peak}}{m_1} = -9.33 \text{ mph}$

$\Delta V2 := (1+e) \cdot \sqrt{\left(\frac{2 \cdot m_1 \cdot \gamma_1 \cdot (E1_{Gen} + E2_{Gen})}{m_2 \cdot \gamma_2 \cdot (m_1 \cdot \gamma_1 + m_2 \cdot \gamma_2)} \right)} - (g \cdot \mu_r \cdot n_2) \cdot \Delta t_{peak} = 14.031 \text{ mph}$

$Diff1_{pw} := \Delta V1 - \Delta v1_{test} = -0.196 \text{ mph}$ $Percent1_{pw} := \frac{\Delta V1 - \Delta v1_{test}}{\Delta V1} \cdot 100 = 2.1$

$Diff2_{pw} := \Delta V2 - \Delta v2_{test} = -0.261 \text{ mph}$ $Percent2_{pw} := \frac{\Delta V2 - \Delta v2_{test}}{\Delta V2} \cdot 100 = -1.857$

Conclusions

The **G-DaTA ΔV^{TM}** system of equations presented consider restitution, tire-ground forces, inter-vehicular friction, and rotational effects that result during many collision events. In the absence of these factors, the equations revert back to their basic parent forms originally developed in the CRASH-based analysis models. Application to the RICSAC testing produced extremely good correlation and linear relationship between the known and calculated values between tests and within the entire testing as demonstrated by the F-test and chi-square test results, respectively, as well as the very linear correlation coefficients. The statistical analysis of the data indicates that any errors resulting between the calculated and test results are first of all minimal. Secondly, the difference between values is random in nature rather than any indication of systematic error. The application of the generalized models to the RICSAC testing is a first validation of the accuracy and precision of the presented methodologies.

The greatest use for the **G-DaTA ΔV^{TM}** system of equations is for the forensic analysis of real-world collision events; the methods should allow for greater

confidence in the calculated total velocity change results when the analyst has adequate data to apply these principles. The presented methods have been applied by this author to the following impacts where vehicle and surface specific structural stiffness characteristics were either scarce or non-existent:

- Broadside or oblique side impacts.
- Rear end impacts.
- Impacts involving light trucks, vans, and sport utility vehicles where vehicle and surface specific structural stiffness values are scarce.
- Impacts involving heavy vehicles, buses, RVs, motorcycles, and other similar vehicles with few vehicle- and surface-specific data.
- Impacts with non-vehicular objects, or unique vehicles such as trailers or heavy equipment that deform when struck, but have no known structural stiffness data.

Additional future research should include the application of the **G-DaTA ΔV^{TM}** system of equations to vehicles and impact conditions outside of the RICSAC validation testing.

References

1. Campbell K. Energy basis for collision severity. SAE Technical Paper 740565. Warrendale PA: Society of Automotive Engineers; 1974.
2. CRASH III user's guide and technical manual. United States DOT, National Highway Traffic Safety Administration, National Center for Statistics and Analysis, Accident Investigation Division. Government Printing Office: Washington DC; 1986.
3. Tumbas N, Smith R. Measuring protocol for quantifying vehicle damage from an energy basis point of view. SAE Technical Paper 880072. Warrendale, PA: Society of Automotive Engineers; 1988.
4. Fricke L, Baker J. Traffic collision investigation. 10th Edition. Evanston, IL: Northwestern University Center for Public Safety; 2006. Chapter 3.
5. Rose N, Fenton S, Ziernicki R. An examination of the CRASH3 effective mass concept. SAE Technical Paper 2004-01-1181. Warrendale, PA: Society of Automotive Engineers International; 2004.
6. Ogden J. Forensic engineering analysis of damage and restitution in low velocity impacts. Journal of the National Academy of Forensic Engineers. 1999;16(2):11-34.
7. Ogden J. Methods of investigating and reconstructing minor damage low velocity motor vehicle accidents. Master of Science Thesis. University of Colorado Denver. October 1995.
8. Greenwood D. Advanced dynamics. New York: Cambridge University Press; 2003.
9. Hibbeler R. Engineering mechanics: statics and dynamics. 3rd ed. New York: Macmillan Publishing Company; 1983.
10. Nikravesh P. Planar multi-body dynamics: formulation, programming, and applications, Appendix A: Mass center and moment of inertia. Boca Raton: CRC Press (Taylor & Francis Group); 2008. 433-438.
11. Garrott W. Measured vehicle inertial parameters, NHTSA's data through September 1992. SAE Technical Paper 930897. Warrendale, PA: Society of Automotive Engineers; 1993.
12. Garrott W, Monk M, Christos W. Vehicle inertial parameters - measured values and approximations. SAE Technical Paper 881767. Warrendale, PA: Society of Automotive Engineers; 1988.
13. Neptune J. Overview of an HVE vehicle database. SAE Technical Paper 960896. Warrendale, PA: Society of Automotive Engineers; 1998.

14. Warner C, Smith G, James M, Germane G. Friction applications in accident reconstruction. SAE Technical Paper 830612. Warrendale, PA: Society of Automotive Engineers; 1983.
15. Marine M. On the concept of inter-vehicle friction and its application in automobile accident reconstruction. SAE Technical Paper 2007-01-0744. Warrendale, PA: Society of Automotive Engineers; 2007.
16. McHenry, Lynch, Segal. Research input for computer simulation of automobile collisions (Vol 1-4). U.S. DOT HS-7-01511. Washington, D.C.: National Highway Traffic Safety Administration; 1978.
17. McHenry B, McHenry R. RICSAC-97, a reevaluation of the reference set of full scale crash tests. SAE Technical Paper 970961. Warrendale, PA: Society of Automotive Engineers; 1997.

Forensic Engineering Investigation of Workplace Incidents Involving Machinery

By Richard Ziernicki, Ph.D., P.E. (NAFE 308F)

Abstract

On many occasions, a forensic engineer faces numerous questions when investigating workplace incidents involving machinery, such as: Why did this incident happen? Was it the operator who caused the incident? Was the operator properly trained? Was the equipment properly maintained? Was the equipment defectively designed or manufactured?

This paper focuses on potential product defect issues. How can one determine whether the product was defective and unreasonably dangerous? The paper outlines issues related to the investigation of product liability cases, and discusses potential procedures and steps to be taken in order to establish whether the product is defective or unreasonably dangerous.

The author explains the role of industrial regulations and standards from sources such as the Code of Federal Regulations (CFR), Occupational Safety & Health Administration (OSHA), American National Standards Institute (ANSI), International Organization for Standardization (ISO), and other entities in the process of assessing product safety. In addition, the role of the safety triad, technical and economic feasibility, and warnings/instructions in assessing product safety are examined. The author also discusses another useful approach to safety: implementation of Failure Modes and Effects Analysis (FMEA). Finally, two product cases are presented to illustrate the process of safety analysis and investigation.

Keywords

Forensic engineering, product defect, unreasonably dangerous, standards, safety hierarchy, safety triad

Introduction

Workplace product safety is a combined effort of a designer, manufacturer, user (operator), and employer (if involved). Installers, maintenance providers, and training entities may also play a role in workplace product safety. However, if something goes wrong, the highest price of injury or death is typically paid by the operator. Therefore, it is essential for manufacturers to design equipment/machines to be as safe as practical.

In many cases, in regards to safety, an equipment manufacturer relies heavily on instructions, manuals, warnings, and proper training of potential users. Therefore, the manufacturer has less emphasis on hazard and risk analysis as a method of hazard minimization and ensuring proper guarding. This approach is quite often unsuccessful, and results in serious injury or death. Some reasons for this type of approach stem from lack of knowledge about best practices in safety, concerns

about an increase in product cost by implementing more stringent safety procedures, or simple recklessness. In some cases, safety is simply not a sufficient priority for manufacturers. This author has found that instructions and equipment manuals, written by an individual with great knowledge of the equipment, often assume readers have a great deal of technical knowledge of the equipment, when, in fact, they may not. This may leave the normal operator, especially a new operator, with a great deal of doubt as to the proper operation of the equipment.

On the other hand, many employers have limited financial resources, have a poor understanding of safety, provide inadequate training for their employees, or are simply careless. Further, equipment operators may be tired, poorly trained, illiterate, rushed, or sloppy — and some may even misuse the product.

Any combination of the situations noted above can create a perfect setting for a serious or even deadly incident. Even with proper training and years of experience, machine operators are still getting seriously injured or killed. It may happen because the equipment is simply not safe, or an operator is confused about the safe operation of equipment.

This paper discusses a broad approach to product liability cases, which includes basic terminology, industry standards and practices, and then presents two examples of brief case studies that involve some of the product liability issues addressed in this paper.

Defective and Unreasonably Dangerous Products

In some cases, when serious injury or death occurs, the injured party or his/her estate brings a lawsuit against the designer, manufacturer, distributor, or other entities under the claim of a “defective and unreasonably dangerous product.” After analyzing the incident, an expert witness is asked whether a product is defective and whether the defendants or operator contributed to the incident causation.

In simple terms, a product may be defective and unreasonably dangerous if it can cause an injury, the injury can be serious, and it is technologically and economically feasible to design the hazard off the machine or to guard against the hazard. Technologically feasible means that before the product was manufactured, there was a technology available to make the product safer and to eliminate (or guard against) the defect. Economically feasible means that a higher level of product safety was available at a reasonable cost.

In safety engineering, hazards represent the potential of a product or process to cause injury, death, or damages; risk is the probability of injury, death, or damages.

A product can be defective and unreasonably dangerous if it is defectively designed, defectively manufactured, has defective warnings and instructions, or is defectively maintained. It should be noted in most cases, because of workers compensation immunity statutes, the plaintiff cannot bring a case against his or her own employer.

Safety Practices

In safety engineering, it is commonly understood today that a risk analysis is required by the designer to identify and eliminate or guard against serious hazards.

When hazards with significant risks of serious injury or death are identified with a product, safety methodologies should be used to mitigate the risks associated with the product. The methodology to mitigate the risks has been referred to as an engineering hierarchy, design order of precedence, or engineering triad. Methodologies for proper product design and safety engineering principles have been published in many texts on safe product design^{1,2,3,4} and have also been recognized in engineering standards^{5,6,7}. In essence, hazards are to be eliminated according to the following hierarchy of steps:

- The first priority in safety engineering is to eliminate the hazard through design.
- If the hazard cannot be eliminated due to practical or functional reasons, the hazard must be guarded against.
- If the hazard cannot be guarded against, then warnings should be used.

The safety hierarchy can also be expanded to the following:

- Design so there is no hazard.
- Eliminate hazards through redesign.
- Provide guards/barriers against hazard.
- Provide automatic and manual warning systems (visual, audible).
- Provide warning signs and labels.
- Provide warnings in manuals, written instructions, and training.
- User must wear protective gear, since hazard is unavoidable.

It should be clearly understood that guards or safety devices should only be used if the hazard cannot be eliminated by design. Warnings are a last resort to be used only if the hazard cannot be eliminated by design or guarding. Warnings are a minimum requirement of safety engineering. The hierarchy has been graphically represented as **Figure 1**.

The safety triad principle is important because it requires the manufacturer to be proactive and deal directly with the hazard, rather than simply expecting the operator to comply with what may be very complicated instructions, warnings, or manuals.

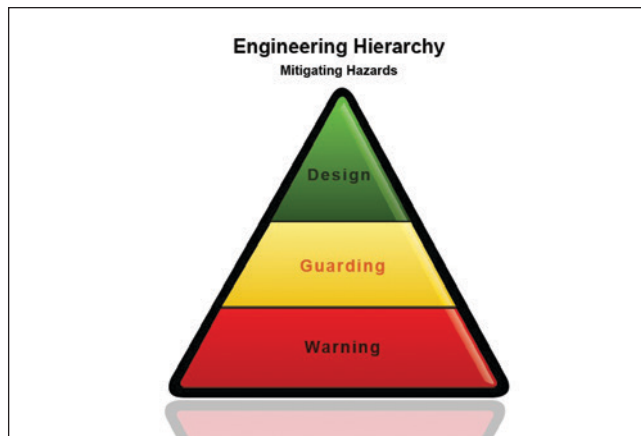


Figure 1

Engineering safety hierarchy of hazard mitigation.

Another important safety design practice is to design a product not only for foreseeable use but also for foreseeable misuse by the potential operator. The term “reasonably foreseeable misuse” is defined in ANSI/AMT B11.0 2008: *Safety of Machinery – General Requirements and Risk Assessment* as: “The use of a machine in a way not intended by the supplier or user, but which may result from readily predictable human behavior.”

Role of Standards

There are many standards available to assist in safety assessment of a given product. These range from mandatory to voluntary to industry guidelines/recommendations to industry “verbal” practices. When conducting investigation of product liability cases, a forensic engineer should be familiar with applicable industry standards and practices. He or she should use them in reaching opinions, including whether the product is defective and unreasonably dangerous. Examples of important standards and regulations are listed below:

A. Code of Federal Regulations (CFR)

consists of thousands of regulations (and referenced standards) that are related to many different industries, such as:

- Transportation (Title 49), including:
 - Federal Motor Carrier Safety Administration (FMCSA) - 49CFR300-399
 - Federal Motor Vehicle Safety Standards (FMVSS) - 49CFR571
- Labor: Occupational Safety and Health Administration (Title 29), including:

- General Industry - 29CFR1910
- Construction - 29CFR1926

B. American National Standards Institute

(ANSI) is an accreditor of voluntary consensus Standards Development Organizations (SDOs), which, in turn, publish safety standards for products, including cranes (ANSI/ASME B30.17), forklifts (ANSI/ITSDF B56.1 and B56.6), wood chippers (ANSI/ISA Z133.1), and many more.

C. International Organization for Standardization (ISO) covers multiple industries and product safety issues.

In the international arena, a company’s engineering design procedures are guided by the 2003 ISO 12100-1 *Safety of Machinery – Basic Concepts, General Principles for Design* standard, which defines that the basic concepts for safety of machinery include general principles for design. This ISO standard outlines the mechanical hazards associated with machinery and presents six general provisions for risk reduction. The first two state:

- a. “It is assumed that, when present on machinery, a hazard will sooner or later lead to harm if no protective measures are taken.”
- b. “Protective measures are a combination of measures taken by the designer and the user. Measures that can be incorporated at the design stage are preferable to and generally more effective than those which are implemented by the user.”

The ISO 12100 standard, which provides a process for hazard identification and risk assessment, states:

“When carrying out a risk assessment, the risk from the most likely severity of the harm is likely to occur from each identified hazard shall be considered, but the highest foreseeable severity shall be taken into account, even if the probability of such an occurrence is not high.” In section 5.4, entitled elimination of hazards or reduction of risk by protective measures, it states:

“This objective may be met by removing the hazards by reducing, separately or simultaneously, each of the two elements that determine the risk: (i) severity of harm from the hazard under consideration; (ii) probability of occurrence of that harm.”

The ISO 12100 standard also provides a sequence of steps to achieve a reduction of risk:

“All protective measures intended to reach this objective shall be applied according to the following sequence referred to as the ‘3-step method,’” which is shown in **Figure 1** and summarized as follows (also see ISO 14121 *Safety of Machinery — Risk Assessment — Part 1: Principles*):

- a. *“Inherently safe design measures (Note: this stage is the only one at which hazards can be eliminated, thus avoiding the need for additional protective measures such as safeguarding or complementary protective measures.)”*
- b. *“Safeguarding and possibly complementary protective measures.”*
- c. *“Information for the user about the residual risk. (Note: Information for the user shall not be a substitute for correct application of inherently safe design measures of safeguarding or complementary protective measures.)”*

OSHA regulations require all machines to be guarded. Some courts will not allow mention of OSHA rules and regulations during a products case. The forensic engineer must determine prior to rendering his or her opinions if the courts will allow relying on the OSHA rules and regulations. The retaining attorney should be able to provide this information. The general requirement for machine guarding can be found at 29 CFR 1910.212(a)(1). The regulation states:

“One or more methods of machine guarding shall be provided to protect the operator and other employees in the machine area from hazards such as those created by point of operation, ingoing nip points, rotating parts, flying chips and sparks. Examples of guarding methods are barrier guards, two-hand tripping devices, electronic safety devices, etc.”

In many cases, there is a dispute whether equipment was defectively designed, was poorly maintained, if the operator was poorly trained or did not follow instructions, if the operator did not follow lockout/tagout procedures (described below), or the lockout/tagout procedures were defectively written. OSHA specifically regulates lockout/tagout procedures.

OSHA, Title 29 Section 1910.147 *The Control of Hazardous Energy (lockout/tagout)* section (a)(2) states: *“Application. This standard applies to the control of energy during servicing and/or maintenance of machines and equipment.”*

The regulation defines *“servicing and/or maintenance”* as *“Workplace activities such as constructing, installing, setting up, adjusting, inspecting, modifying, and maintaining and/or servicing machines or equipment. These activities include lubrication, cleaning or unjamming of machines or equipment and making adjustments or tool changes, where the employee may be exposed to the unexpected energization or startup of the equipment or release of hazardous energy.”*

It should be noted that a given product can meet all voluntary and even mandatory standards and still can be found defective and unreasonably dangerous. Examples of such cases include where a motor vehicle meets all Federal Motor Vehicle Safety Standards but nevertheless has problems with crashworthiness or defects in seatbelts, air bags, seats, etc. Recently, General Motors recalled millions of vehicles with a defective ignition switch that affected the safe operation of airbags, brakes, and steering systems. In 2014 alone, General Motors recalled more than 29 million cars worldwide (25 million in the United States) for a variety of different defects⁸.

Failure Modes and Effects Analysis

Another useful approach to safety analysis is Failure Modes and Effects Analysis (FMEA), which was originally created in the 1940s by the U.S. military and was further developed by the aerospace and automotive industries.

FMEA is an analytical methodology and a step-by-step approach for identifying both potential reliability issues and potential safety hazards in a design, manufacturing process, product, or service. Failures are prioritized according to how serious their consequences are, how frequently they may occur, and how easily they can be detected. The purpose of the FMEA is to take actions to eliminate or reduce failures, starting with the highest-priority ones.

FMEA includes review of the following:

- Failure opportunities (What could go wrong?)

- Failure causes (Why would the hazard happen?)
- Failure effects (What would be the consequences of each failure?)

Important FMEA-related standards include:

1. Commission Electrotechnique Internationale: IEC 60812 Edition 2.0 (also known as British Standard: BS EN 60812:2006).
2. Society of Automotive Engineers: SAE-J1739
3. Automotive Industry Action Group: FMEA-4

All the above provide users with information on how to identify the potential for system elements to fail and how to assess and analyze the hazard. By using an FMEA standard, the designer may be able to eliminate the hazard during the design stage, or mitigate the hazard effects to avoid undesirable safety consequences on the existing hazard.

1. **IEC 60812 Edition 2.0** from 2006, *Analysis Techniques for System Reliability – Procedure for Failure Mode and Effects Analysis (FMEA)*,⁹ (also known as BS EN 60812 2006) describes failure mode and effects analysis (FMEA) and failure mode, effects and criticality analysis (FMECA), and gives guidance as to how these techniques may be applied to achieve various reliability program objectives by:
 - Identifying appropriate terms, assumptions, failure modes, and criticality measures.
 - Providing the procedural steps necessary to perform an analysis.
 - Providing examples of the typical forms used.
2. **SAE J1739**, *Potential Failure Mode and Effects Analysis in Design (Design FMEA), Potential Failure Mode and Effects Analysis in Manufacturing and Assembly Processes (Process FMEA)*¹⁰. This SAE-recommended practice was jointly developed by Chrysler, Ford, and

General Motors under the sponsorship of the United States Council for Automotive Research (USCAR). It is geared toward the ground vehicle community and assists users in the identification and mitigation of risk by providing appropriate terms, requirements, ranking charts, and worksheets. As a standard, this document contains requirements and recommendations to guide the user through the FMEA process.

3. **AIAG FMEA-4**, *Potential Failure Mode & Effects Analysis – 4th Edition*,¹¹ is a reference manual to be used by suppliers to Chrysler, Ford, and General Motors as a guide to assist them in the development of both design and process FMEAs. The manual does not define requirements; it is intended to clarify questions concerning the technical development of FMEAs.

Wood Chipper Fatality Incident

This is a case study of a fatal incident involving the operator of a commercial wood chipper. The operator was a 20-plus-year veteran of the tree trimming industry, was well trained, and was a supervisor of his two-man crew. One man would trim the tree, and the other would feed the chipper. A witness saw the tree trimming truck and the chipper pull up to the incident location. He observed the branches being cut, saw the operator picking up loads of branches (with both hands and arms) from behind the area of the chipper, and then watched him carry each load of branches to the rear of the chipper where the branches were fed. He saw the operator doing this same process numerous times over an approximate 30-minute period before the incident happened. There were no eye witnesses to the actual incident.

Based on the witnesses' statements and biomechanical evaluation of the operator injury pattern, as the operator was feeding branches into the chipper, his right hand or arm apparently became caught or entangled, which pulled him into the infeed chute, the feed wheel, and then the cutting drum containing the blades. The victim died in this very gruesome incident (see **Figure 2** and **Figure 3**).

The wood chipper (as designed) has a quick-stop and reverse control bar that allows the operator to feed the material in, stop, or reverse the material out. The



Figure 2

Wood chipper with the towing truck.

wood chipper manual stated that the machine complied with the ANSI/ISA Z133.1 *Standard for Arboricultural Operations – Safety Requirements*. The ANSI Z133.1 is a minimum voluntary standard. It states:

“The activating mechanism for the quick-stop and reversing device shall be located across the top, along each side, and close to the feed end of the infeed hopper within easy reach of the worker.”

In certain conditions, the operator’s glove or clothing can be entangled with wood branches, and the operator’s body can be pulled into the wood chipper. Under an emergency condition, the operator has to reach and activate the “quick-stop.” Because the “*activating mechanism*,” as designed, was too far for the operator to reach under an emergency situation, the operator was unable to reach the quick-stop and was fed into the wood chipper. **Figure 3** shows the operator when feeding the wood chipper with the branches in relationship to the control bar.

Although the wood chipper apparently complied with this ANSI standard by providing “quick-stop and reversing device,” it did not comply with the standard by making this reversing device “within easy reach of the worker.” While in danger, the worker could not reach the reversing device, and the fatal incident still took place¹².

In conducting the investigation, this engineer also analyzed the presence and effectiveness of warning labels and instructions. There were warning labels attached to the wood chipper warning the user against potential hazards as follows:



Figure 3

Still frame from an animation of the incident.

- Never reach inside infeed chute.
- Never operate this machine when wearing loose clothing, scarves, gauntlet-style gloves, or gloves with large cuffs or holes.
- Never operate this machine alone. Make certain there are at least two people with this machine at all times.
- Never operate this machine without thoroughly reading the operator’s manual.

However, the warnings were not clear, did not include graphical representations, and were written in small letters. Some of the warning labels were worn and not readable. Therefore, this engineer concluded that warnings and/or instructions would not have prevented this incident.

Because of the ineffectiveness of the control bar and warnings and instructions in preventing this incident, this engineer evaluated other safety devices that could have prevented this incident. One effective safety device is a “knee bar” depicted in **Figure 4**. A knee bar is a passive safety device, located across the horizontal opening of the infeed chute/tray and is activated by a caught or entangled operator whose knees come in contact with the bar. The bar, pushed passively by the knees, activates the infeed reverse motion and prevents the operator from being pulled into the infeed chute.

Had a knee bar been present on the subject machine, as it should have been to provide safety protection to operators, the operator’s body (particularly his upper leg and knee) would have activated the knee bar before any part of his body came in contact with the feed wheel (**Figure 4**).



Figure 4

Wood chipper with knee bar and surrogate testing.

Research shows the knee bar was available on the market from one manufacturer when the wood chipper in question was manufactured (2002). Such a “knee bar” and its design was technologically and economically feasible for many years before the wood chipper in question was designed and manufactured. Furthermore, there were many patents describing knee bar design and technology – years before the wood chipper in question was manufactured.

In this engineer’s opinion, it was unreasonable for the manufacturer not to implement a knee bar design as standard equipment simply because the existing standards (including ANSI Z133.1) did not require such a device. The knee bar is an effective safety feature, had been economically and technologically feasible for many years, and would prevent many serious or fatal incidents. It took several years before all major wood chipper manufacturers decided to equip their wood chippers with a safety knee bar.

Since 2012, most manufacturers offer knee bars with their commercial wood chippers, even when the ANSI standard does not have such a requirement.

When processing wood branches in the wood chipper, the branches are fed into the wood chipper at a speed of 2 feet per second. Many operators do not comprehend how quickly an operator, if entangled with branches, can be pulled into the wood chipper — a situation that can result in a fatal incident. In many cases there is not even time for an operator to activate the control bar and rescue himself. Simply relying on operator training, safety labels, and warnings or instructions is not reasonable and can lead to many serious and deadly incidents¹³.

The wood chipper case study shows that the wood chipper (as designed) did not meet the ANSI/ISA Z133.1 *Standard for Arboricultural Operations – Safety Requirements*; there was no evidence that OSHA regulations were violated. At the time the wood chipper was manufactured, only one manufacturer offered a knee bar as safety equipment. Today, all major wood chipper manufacturers not only provide a knee bar for their wood chippers as a standard equipment but they also provide retrofit of knee bars to any commercial wood chipper equipped with a control bar.

The forensic engineer should be prepared to answer the following questions:

1. ***What was the probable cause of the incident?*** *The probable cause of the incident was the operator being caught and entangled with the wood branches during the feeding process and his inability to free himself. In addition, he did not have enough time to reach the control bar because it was located too far for him to reach and activate it.*
2. ***Is this product defective and unreasonably dangerous?*** *The wood chipper was defective and unreasonably dangerous as designed due to lack of a passive safety device to prevent an operator, in certain emergency conditions, being fed into the wood chipper.*
3. ***Could this incident be prevented by a safer design?*** *Yes it could, by providing a knee bar. Operator training, warnings, and instructions will not prevent this incident.*

Forklift Double Fatality Incident

This incident occurred at a plastic pipe manufacturing plant in a loading area. The forklift operator had just finished loading a semi-trailer with a pipe load. After the operator finished loading the semi, the operator parked the forklift on a slight incline near the semi. The operator then set the subject forklift’s transmission to neutral, turned the forklift’s engine off, and applied the forklift’s parking brake. After applying the parking brake, the operator got off the forklift and walked toward the semi driver, who was located near the right front of the semi’s trailer.

Witnesses’ statements, inspection of the incident site, inspection and testing of the forklift, and PC

Crash¹⁴ simulation of the forklift motion (with known initial and final rest position, slope at the incident site and rolling resistance of the forklift) indicate that the subject forklift started rolling forward slowly as soon as the operator took his foot off of the forklift’s service brake pedal. PC Crash simulation was used for camera match animation of the incident, and **Figure 5** and **Figure 6** are still frames from the animation.



Figure 5

Still frame from the animation depicting the incident.



Figure 6

Still frame from the animation depicting the incident from another camera view.



Figure 7

Subject forklift showing parking brake lever.

When the operator got off the forklift, the machine began traveling at such a low velocity that it apparently remained undetected by the operator. After the operator got off the forklift, he began to walk much faster than the forklift’s velocity at that time. Approximately 15 seconds after the operator got off the forklift, the forklift struck both the operator and the semi driver at an approximate speed of 2 to 3 mph and pinned them against the trailer (**Figure 5** and **Figure 6**). Both the operator and the semi driver died as the result of the incident.

After the incident, the Occupational Safety and Health Administration (OSHA) performed an investigation of the subject forklift. OSHA issued a citation to the employer for failing to chock the wheels of a powered industrial truck while parked on an incline (see **Figure 7**).

After the incident, this engineer inspected the braking system and found a lot of caked-on dirt and debris on the outside of the caliper housing and linkage system (**Figure 8**), indicating that the parking brake system components had not been serviced in a long time — possibly years. In addition, the operator’s manual preventive maintenance schedule stated that the parking brake pads must be checked and replaced, as necessary, every 300 hours. However, the heavy wear on the movable parking brake pad and the employer’s maintenance records indicated that the subject forklift’s brake pads had never been replaced in its five-year history and approximately 6,900 hours of service. Therefore, the employer failed to follow the manufacturer operator’s manual preventive maintenance schedule regarding checking and replacing the parking brake pad every 300 hours, as necessary.



Figure 8

Caked dirt located over parking brake linkage components.

In addition, the parking brake was tested by this engineer on the incident site (1.2 percent slope), and it was found that with the parking brake engaged, the forklift began to roll down the incline. Furthermore, review of the ANSI/ASME B56.6 *Safety Standards for Rough Terrain Forklift Trucks* was conducted to determine if the subject forklift's parking brake was defective. Section 8.8.1 of the standard states:

“The parking brake system shall be capable of holding the rough terrain forklift stationary on a 15% dry swept grade under all conditions of loading in both forward and reverse directions”¹⁵.

The subject forklift's parking brake was not able to hold on an incline of no more than 1.2 percent, which was substantially lower than the holding requirement of 15 percent outlined in ANSI B56.6. Therefore, this engineer determined that the parking brake was defective at the time of the inspection.

The operating manual discussed a very simple six-step method that provides forklift operators the ability to adjust the parking brake from within the forklift's operating compartment without the need of any tools or specialized maintenance personnel.

This engineer also conducted testing of braking performance of the forklift and determined that after the parking brake was adjusted per the instructions in the operator's manual, the forklift's parking brake functioned properly. Therefore, had the employer followed the parking brake adjustment procedure described in the forklift's operational manual prior to the incident, the parking brake would have been in proper working condition, and the incident would not have occurred.

The forensic engineer should be prepared to answer the following questions:

1. *What was the probable cause of the incident?*
2. *Is this product defective and unreasonably dangerous?*
3. *Could this incident be prevented and how?*

Incident analysis shows there was nothing wrong with the forklift design or manufacturing. The forklift was simply in an out-of-service mechanical condition caused by lack of proper maintenance and adjusting of the braking system, perhaps for many years. Although the forklift was properly designed and manufactured, it was kept in a defective and unreasonably dangerous condition due to improper maintenance, resulting in a double fatality incident.

Conclusions

This paper shows examples of paths for a forensic engineer to investigate certain types of “product liability” cases. It discusses the basic techniques and procedures to investigate such cases. Furthermore, the paper shows how industry standards, product manuals, product testing and examination, market research, and literature research are used to determine whether a product is defective and unreasonably dangerous.

Furthermore, this engineer shows that relying on instructions and warnings may not be an effective method in preventing certain types of incidents. This paper demonstrates that the equipment can be defective and unreasonably dangerous not only by design but also solely by defective maintenance. As shown in this paper, if something goes wrong, the operator/user typically pays the highest price.

References

1. Hammer W. Handbook of system and product safety. Englewood Cliffs, NJ: Prentice-Hall, Inc.; 1972.
2. Hammer W, Price D. Occupational safety management and engineering. 5th edition. Englewood Cliffs, NJ: Prentice-Hall, Inc.; 1981.
3. Brauer R. Safety and health for engineers. 2nd edition. Hoboken, NJ: Wiley-Interscience; 1994.
4. Roland H, Moriarity B. System safety engineering and management. 2nd edition. Hoboken, NJ: Wiley-Interscience; 1990.
5. ISO 12100-1992. Safety of machinery – basic concepts, general principles for design. Geneva, Switzerland; International Organization for Standardization.
6. ANSI/ASSE Z244.1-2003. Control of hazardous energy-lockout/tagout and alternative methods. Park Ridge, IL; American Society of Safety Engineers.
7. The International System Safety Society. Unionville, Va.: United States Military Standard (MIL-STD) 882D, c2000 [cited 2014]. <http://www.system-safety.org/Documents/MIL-STD-882D.pdf>.
8. General motors recalls 8.2 million more cars. US News; c2014 [Updated June 30, 2014; cited May 28, 2015]. <http://www.usnews.com/news/articles/2014/06/30/general-motors-recalls-82-million-more-cars>.
9. IEC 60812-2006. Analysis techniques for system reliability – procedure for failure mode and effects analysis (FMEA). Geneva, Switzerland; International Electrotechnical Commission.
10. SAE J1739-2008. Potential failure mode and effects analysis in design (design FMEA), potential failure mode and effects analysis in manufacturing and assembly processes (process FMEA). Warrendale, PA; SAE International.
11. Automotive Industry Action Group. Potential failure modes and effects analysis (FMEA), 4th edition. Southfield, MI: Automotive Industry Action Group; 2008.
12. ANSI/ISA Z133.1-2006. American national standard for arboricultural operations – safety requirements. Champaign, IL; International Society of Arboriculture: Section 5.3.5.
13. Ziernicki R, Heist A, Railsback B. Analysis of the hazards of wood chipper accidents, Paper No. IMECE2011-62786. Denver, CO: American Society of Mechanical Engineers; 2012.
14. Datentechnik S, PC Crash Software, Version 9.1.
15. ANSI/ASME B56.6-2002. Safety standard for rough terrain forklift trucks. New York, NY; American Society of Mechanical Engineers: Section 8.8.1.

Furnace Malfunction & Forensic Engineering Wiring Reconstruction

By John Certuse, P.E. (NAFE 708F)

Abstract

This paper details the fire investigation and forensic engineering failure analysis of an oil-fired furnace that had been recently installed. An underlying focus of this paper is the procedure that was used to analyze the electrical and mechanical components leading to the failure – given that evidence had been spoliated. This process demonstrates that by following a systematic investigation procedure, forensic engineers may reconstruct evidence that (in some cases) has been either destroyed or altered (whether intentionally or not) to a level that allows further insight into the malfunction.

This paper details the procedure used to document deviations from intended wiring schematics as well as the physical characteristics of electrical controls and wiring materials used in its construction. The intent of the paper is to show how this investigation procedure can be applied to other forensic investigations where electrical circuit evidence has been altered or a spoliator's identity is not readily known.

Keywords

Forensic engineering, furnace fire, fire investigation, wiring reconstruction, electrical circuit analysis, forced air furnace, high limit control

Furnace Design & Operation

The most common of all residential heating appliances in the United States is the forced air furnace. This unit transfers energy from the combustion of fuel — be it No. 2 fuel oil, natural gas, or propane — within an internal heat exchanger to the circulating air stream.

Building air is circulated along the outer portion of the heat exchanger (within the furnace jacket enclosure, **Figure 1**) and distributed through a system of ductwork supplying heated or conditioned air throughout the building.

To prevent excessive temperatures from being developed within the furnace, these appliances are outfitted with a high temperature control, commonly referred to as the high limit switch.

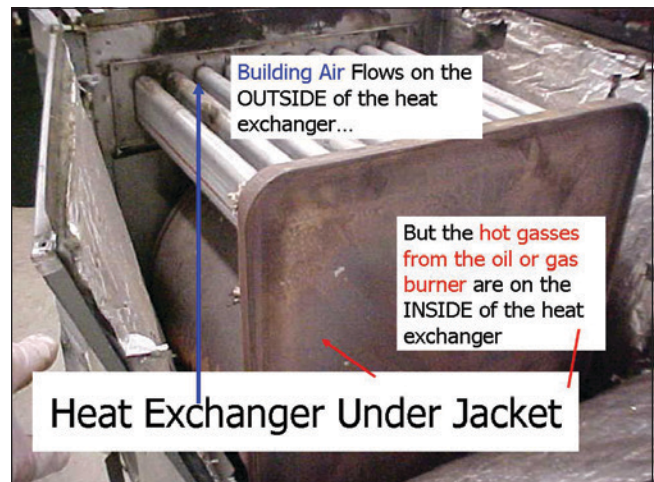


Figure 1
Forced air furnace.

High Limit Switches

High limit (or fan limit switches) — helical coil or bi-metallic thermal sensing controls — function to shut the burner down in the event of excessive temperature. A fan limit control is shown in **Figure 2**.

Integration with Air Conditioning

In many areas of the United States, the flexibility to provide both hot air during winter and conditioned air during cooling season is accomplished by an evaporator coil installation and control arrangement allowing only one mode of operation at a time.

This allows the furnace to also function as an air-conditioning air handler fan cabinet during summer cooling months while also allowing it to provide heat during winter weather conditions.

When a forced hot air heating system is also outfitted with an air conditioning evaporator coil, a fan relay center is installed that prevents the simultaneous operation of the furnace burner and the air conditioning condensing unit. **Figure 3** shows a forced air heating system that is outfitted with air conditioning.

Air Conditioning Evaporator Coil

The evaporator coil, as shown in **Figure 4**, is mounted in a sheet metal enclosure above or to the side of the furnace in a horizontal application. During summer cooling months, moisture in the circulated air will condense on the evaporator coil where it is collected within a condensate pan and then drained to a suitable disposal location to prevent water contact and damage to the furnace.

Initially, condensate pans under evaporator coils were made of metal; however, due to problems with corrosion, many manufacturers have outfitted evaporator coils with polymer or composite condensate drain pans (as shown in **Figure 5**) in order to eliminate the effects of corrosion.

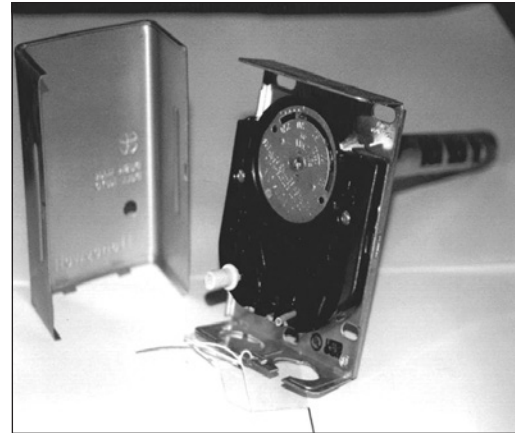


Figure 2
Fan & limit control.

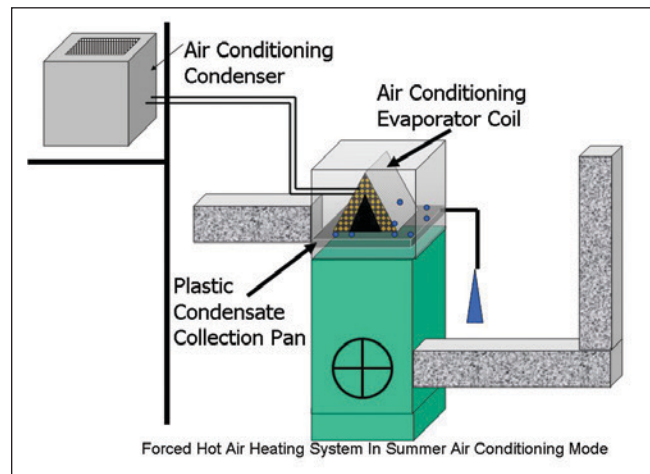


Figure 3
Forced air heating system outfitted with air conditioning.



Figure 4
Evaporator coil.

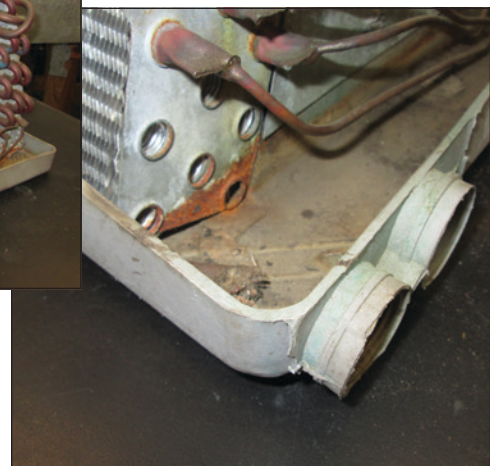


Figure 5
Composite/plastic condensate pan.



Figure 6
Heat-damaged evaporator coil and condensate pan.



Figure 7
Soot damage.

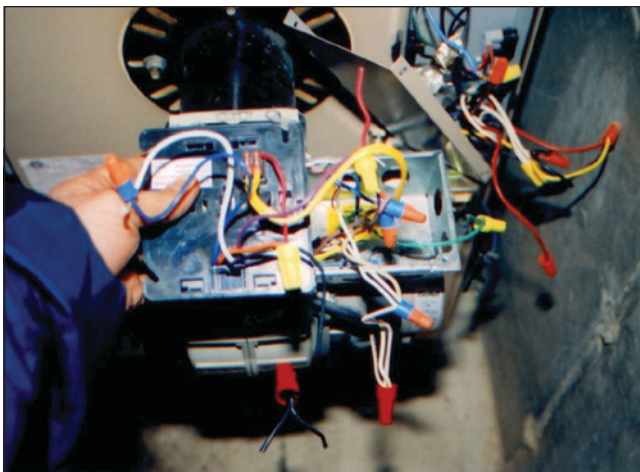


Figure 8
Furnace wiring.

Causes of Evaporator Pan Fires and Runaway Furnaces

Many instances of smoke and fire damage to homes have resulted from overheating furnaces either melting or igniting polymer evaporator coil pans as shown in **Figure 6**. The damage caused by a burning plastic evaporator pan can be extensive, often resulting in smoke and soot damage to the building structure. The melted plastic of the condensate pan may fall into the furnace's heat exchanger and damage the appliance itself, causing it to be replaced.

Fires also result in furnace malfunctions with the level of overheating being so extreme that combustible floor joists above the furnace ignite.

Causes of overheating include:

- Inadequate clearance between furnace/heat exchanger and combustible condensate pan
- Restricted airflow in the recirculation stream
- High limit control failure
- Circulator fan failure
- Improper wiring
- Excessive fuel addition to combustion chamber

Case Study Particulars

This paper focuses on litigation resulting from the malfunction of a new oil-fired forced air furnace installed in the fall of 2005 by a contractor.

In February of 2006, a fire, which was identified as originating within the ductwork of this forced air furnace, occurred at this property. **Figure 7** shows soot damage from the ductwork caused by a burnt evaporator coil pan.

Following the fire, the same company that installed the original furnace removed the fire-damaged appliance and re-installed an identical furnace immediately after the loss.

Fire investigators determined that the furnace wiring had not been preserved after the fire as shown in **Figure 8**. Portions of it were disposed of during the removal and replacement of the fire-damaged appliance.

This investigation provided significant challenges due to spoliation of the evidence.

Investigation Procedures

During the investigation, key variables of the furnace's installation were analyzed to identify potential deficiencies in installation and operation. This included clearance between the heat exchanger and plastic evaporator pan, as well as other conditions previously listed.

Several furnace components were damaged as a result of the fire, including the circulating fan and high temperature control (as seen in **Figure 9**). As a result, pre-fire operability of the furnace could not be determined.

A primary focus in the investigation was the high limit control. The original high limit control was identified as a helical coil type of device inserted into the air stream just downstream from the furnace. Destructive examination of the control commenced by removing the high limit electrical contacts from the control.

Upon examining the contacts, as viewed in **Figure 10**, there was no evidence of any past electrical activity. Accordingly, it did not appear that the high limit control was wired into the control circuit that would have shut the oil burner down in the event of a high temperature.

Testing of an identical "exemplar" control showed that a visible arc overheating of the high temperature control contact was seen after only one cycle of operation. This testing validated the hypothesis that the high limit control was never properly wired into the circuit of the furnace.

Figure 11 shows the contact from the exemplar limit switch.

Wiring Analysis

With the hypothesis apparently confirmed, the next challenge was to determine whether the high limit control was indeed not wired into the circuit, and (if possible) to identify the party responsible for the error in wiring — be that the installer or the manufacturer. The furnace wiring is depicted in **Figure 12**.

Although the furnace had much of its wiring detached and removed when it was detached from the system ductwork and electrical service by the initial contractors, a detailed "as-built" wiring circuit diagram of the existing wires was created (via inspection) and is shown in **Figure 13**.

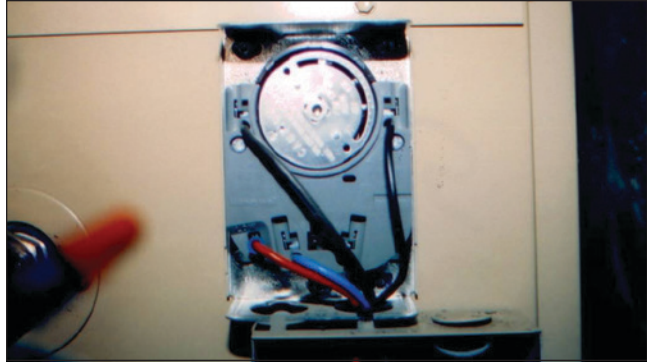


Figure 9

Fan limit and high temperature control into the furnace.

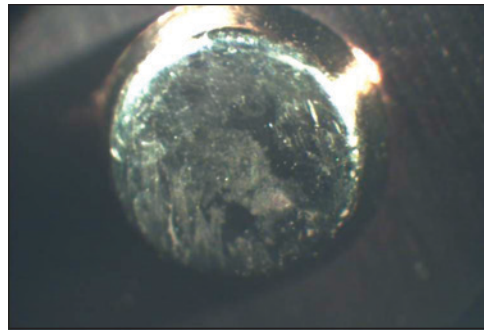


Figure 10

High limit control shows no electrical activity.

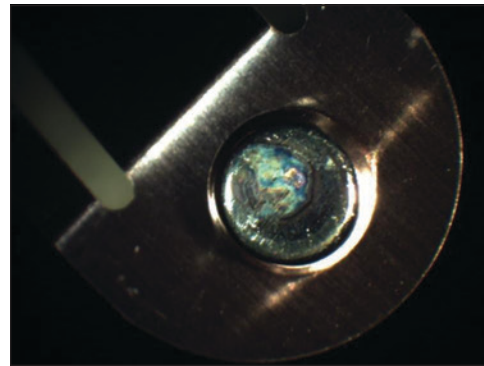


Figure 11

Arcing found on contact of high limit switch that was properly wired into circuit. Compare to contact shown in Figure 10.

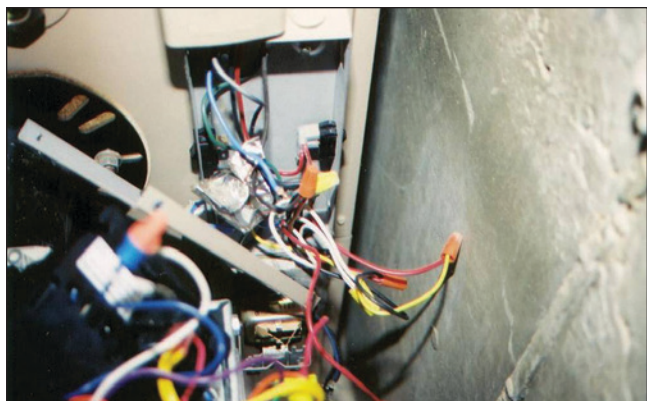


Figure 12

Furnace wiring.

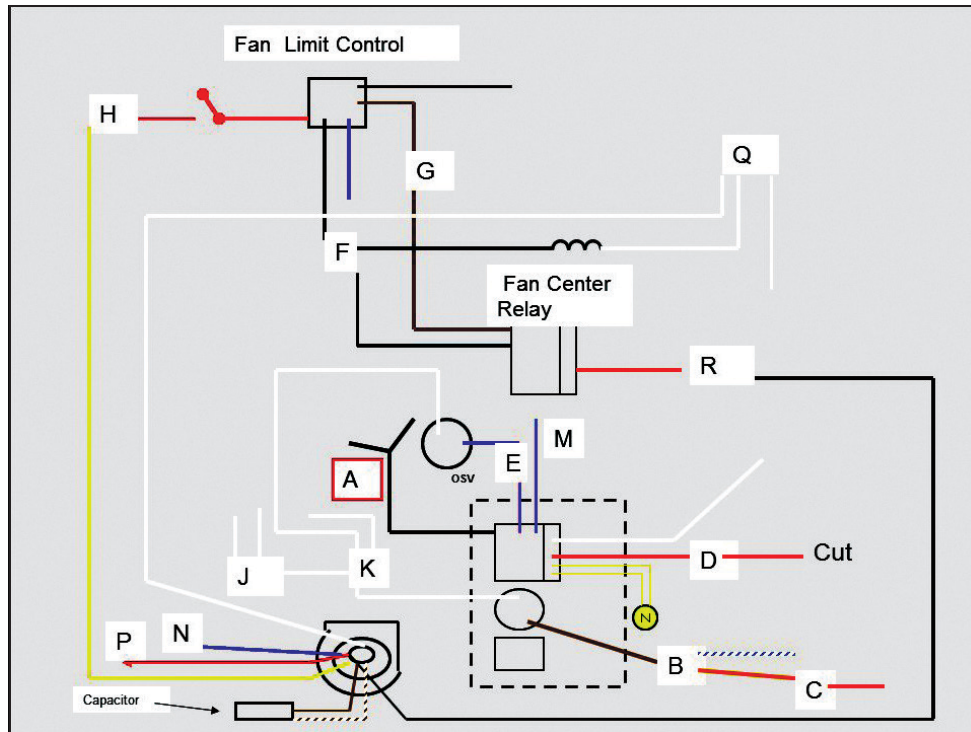


Figure 13
As-built wiring of disassembled furnace.

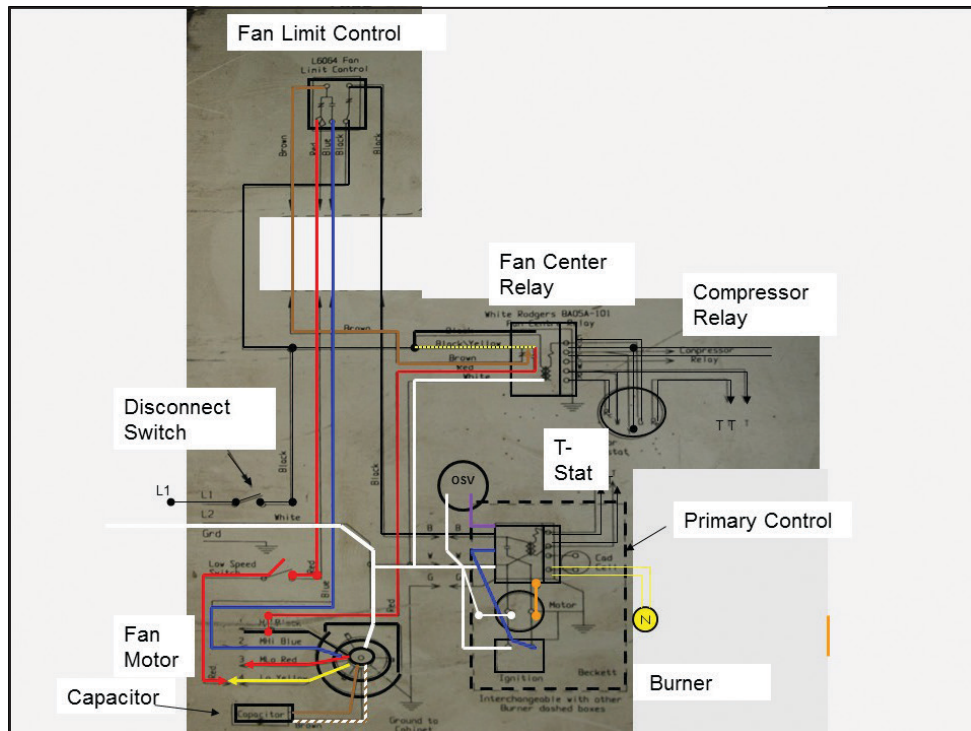
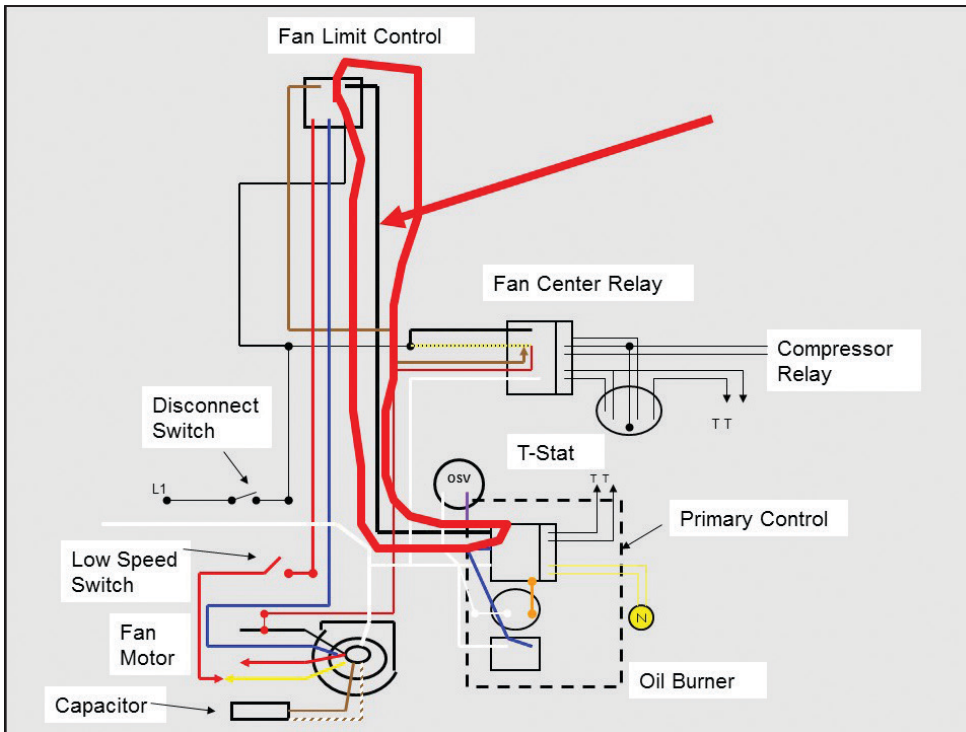









Figure 14
Colored wire lines superimposed over manufacturer's wiring diagram for both furnace and primary high limit control.



Component Identification Key

-  High Limit Control
-  Oil Safety Valve
-  Blower Fan
-  Primary Control
-  Fan Relay Center
-  Thermostat
-  Capacitor

A-R – Wiring Connections

Figure 15

As seen in this manufacturer’s wiring diagram, in no configuration was there supposed to be a branch off of the L1 line to the burner.

Where the as-built wiring drawing was the same as the manufacturer’s wiring diagram, the as-built wiring circuits were superimposed onto the manufacturer’s wiring diagram, as shown in **Figure 14**.

By comparing the as-built wiring on the manufacturer’s wiring diagram, deviations between the two could be identified.

After the as-built wiring diagram and the manufacturer’s wiring diagram were compared, the investigation identified that there was a parallel circuit from the building’s power connection leading into the oil burner that bypassed the high limit control (shown in **Figure 15**).

With this wiring configuration, the furnace burner could be energized upon a call for heat from the thermostat, regardless of the temperature being generated by the burner without the safety feature of the high limit controller. The extra power supply wire is shown in **Figure 16**.

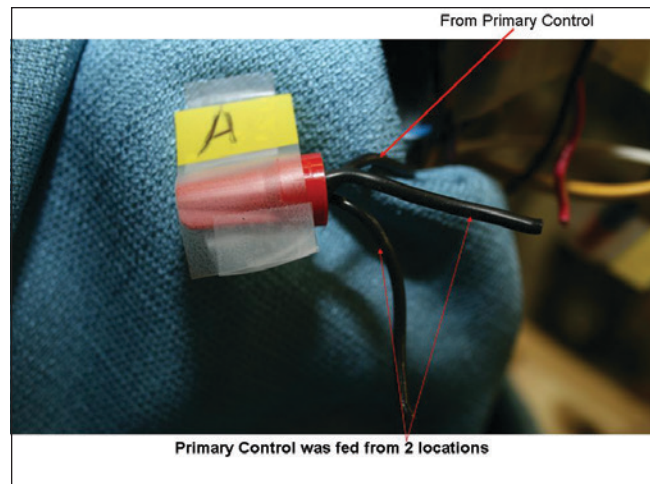


Figure 16

The primary control was fed from two locations, contrary to manufacturer’s wiring instructions.

Characteristics of Improper Circuit Wiring

During examination of the identified wire that was a deviation from the manufacturer’s wiring (**Figure 17**), the following wire characteristics were identified:

- Number of strands
- Wire gauge
- Type of coating
- Manufacturer’s markings

When the factory wiring was compared to the suspect wiring, significant differences (**Figures 18, 19, and 20**) were noted.

The manufacturer of the furnace was Canadian, and all of the factory-installed wiring was identified as originating from a Canadian supplier. The suspect wiring was identified as originating from a U.S. manufacturer. This same wiring was found in some of the connections of the replacement furnace that was also installed by the same contractor who installed the failed furnace.

It should be noted that upon re-examining the replacement furnace, the same identical error in the wiring was also found. Additionally, conditions were found indicative of the beginning of an overheating condition in the replacement furnace. See **Figure 21** for a comparison of the wiring features.

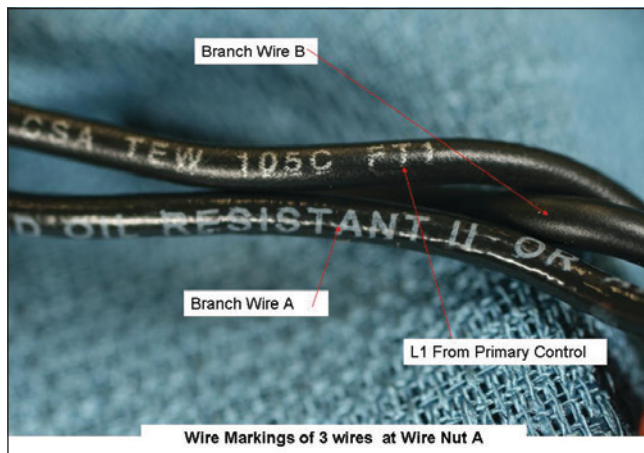
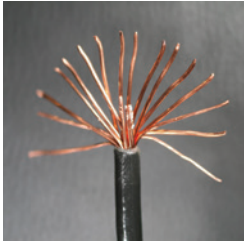
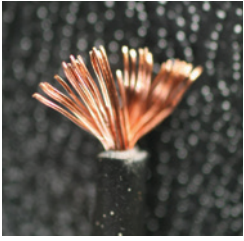



Figure 17
Wire markings of three wires at wire nut A.

	Junction A A Strand	Junction A B Strand	36 Inch Limit L1 Wire
No. Strands	19 - 20	26	24
Coated?	Yes	No	No
Markings	"Markings" Gasoline and oil resistant II or AWM 600 Volt	None	CSA TEW 600V 105C FTLL 3995 - - - AWM 1015 OR 1230 600V

Appears that coated wires are NOT manufacturers Wiring...

Figure 21
Comparison of wiring features.

			
	Figure 18	Figure 19	Figure 20
Wire Segment	A	B	36-in. Segment from Limit Switch
No. of Strands	19-20	26	22
Coated	Yes	No	No
Markings	Gasoline & Oil Resistant II or AWM 600 Volt	No Markings	CSATFW 600V 105C FTILL 3995- - - AWM 1015 OR 1230 600V

Conclusion

The procedure used in the investigation not only allowed identification of whether the wiring in this furnace was properly installed, but it also allowed opinions to be drawn regarding the shortcomings of the “as-built” wiring assembly. Examination of the furnace’s high temperature control showed that it was not wired properly into the circuit. Therefore, it never functioned properly to control the operation of the furnace. As a result, the furnace operated upon the thermostat’s call for heat — regardless of whether or not the temperature generated by the furnace was approaching an unsafe level.

By identifying the characteristics of the materials used in the wiring circuits of this furnace, the forensic engineer was able to identify which wiring circuits were installed by the manufacturer and which were placed by the contractor.

By comparing the as-built wiring to the manufacturer’s wiring diagram, the circuit responsible for the malfunction was found. Through the characteristics of the wiring, the forensic engineering team was able to prove with a reasonable degree of engineering certainty the originator of the negligent work. This led to a settlement based on the determination that the cause of the fire was due to improper installation.

The team reconstructed enough of the existing evidence to develop an opinion as to the cause of the loss. This same procedure could potentially be used with other electromechanical equipment.

Bibliography

Brumbaugh J. Audel HVAC fundamentals, 4th edition. Indianapolis IN; John Wiley: 2005.

Building wire & cable handbook, 3rd edition. Carrollton, GA: Southwire Co.; 2015.

Field EM. Audel oil burners, 5th edition. New York, NY: MacMillan; 1990.

NFPA 70-2013. National electrical code. Quincy, MA; National Fire Protection Association.

NFPA 31-2011. Installation of oil burning equipment. Quincy, MA: National Fire Protection Association.

NFPA 54-2015. National fuel gas code. Quincy, MA: National Fire Protection Association.

NFPA 921-2014: Guide for fire & explosion investigations. Quincy, MA: National Fire Protection Association.

Residential electricity for fire investigators. Benton Harbor, MI: Fire Findings Laboratories; 2014.

Yereance R, Kerkhoff T. Electrical fire analysis, 3rd edition. Springfield, IL: Charles C Thomas Pub Ltd; 2014.

Forensic Engineering Investigation and Analysis of a Tower Crane Collapse

By Bransford Pickett, MScBa, P.E. (NAFE 795M)

Abstract

Tower cranes are popular and one of the predominant methods of material handling in high rise building construction. When there is a collapse of a tower crane in a city like New York, it is very visible, receives intense scrutiny, and becomes potentially political. This paper examines a 250-foot-tall tower crane collapse during the jumping phase of the crane to increase its height in support of a multi-level building construction. The author's investigation examines the "defective sling" claim as the primary cause of the crane collapse along with some key findings and opinions regarding the slings used to rig the collar tie to the tower section of the crane.

Keywords

Ultraviolet, isothermal, slings, tower crane, adiabatic, brittleness, shock load, synthetic

Introduction

This incident investigation looked at the claims made by the People of New York versus the accused master rigger that the 303 51st Street crane collapse (which occurred on 03/15/2008) was a result of an ultraviolet (UV)-degraded sling used to rig a critical 18th floor collar tie. The implication of the UV degradation was the sling did not have the capacity to support the collar tie to which it was attached. In turn, it was implied that the lack of lift capacity in the degraded sling resulted in overload failure. As alleged, this degraded sling failure caused the three remaining slings to fail, resulting in the 18th floor collar tie sliding down the crane tower and rupturing the lower collar ties' rigging on the ninth and third floors. The loss of the rigged collar tie attachments between the building and the crane tower caused the crane to collapse catastrophically.

The following analysis of the rigging associated with the collar tie was accomplished in three categories:

- a. Sling inspection findings
- b. Sling ultraviolet degradation and load carrying capacity
- c. Defense sling test findings

The findings of the investigation did not support the claim that the sling was defective due to ultraviolet degradation. Analysis showed that even if the sling was UV degraded, the loss in lift capacity was insufficient to result in sling failure and ultimately the collapse of the crane.

Tower Crane Configuration Change, Jumping Process

During building construction, as the height of the building changes, there is a requirement to increase the tower sections of the crane. Increasing the crane tower sections (or lowering the crane tower sections) is called "jumping" the crane. **Figure 1** shows the tower sections of the crane going from 18 stories on the left to 28 stories on the right. The jumping process is made up of several steps that can be categorized principally by two phases. The first phase increases the number of sections in the crane tower to a specific height as determined by the engineer of record. The second phase addresses the installation of the collar tie to the crane tower and secures the collar tie and crane to the building. **Figure 1** also shows three highlighted sections where the crane tower is attached to the building.

Typically, tower cranes are configured for one of two jumping methods — internal or external to the building. This case involves the external jumping process. **Figure 2** below gives a typical climbing arrangement and description of the jumping process to increase or decrease the number of tower sections. Phase 1 of the jumping process is as described:

- a. Install climbing collars and ladder. Balance the crane upper, remove the base bolts, and raise the crane using hydraulic rams attached between collar and tower, allowing the climbing supports to skid past and then rest on a ladder rung. Repeat climbing the ladder in this manner, as required.

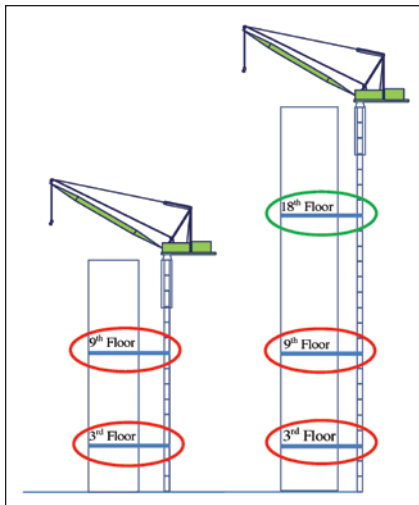


Figure 1

Diagram of tower crane at different elevated heights.

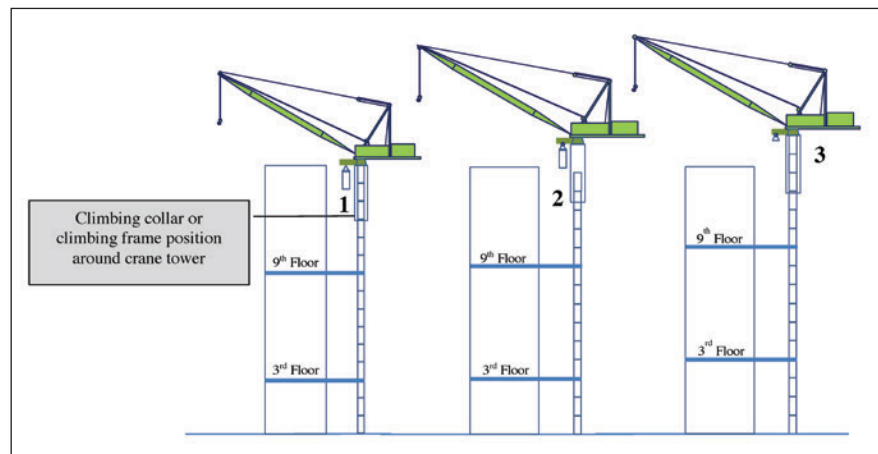


Figure 2

Diagrammatic jumping setup used to change the tower crane height.

- b. Climb through the first collar, and allow the crane supports to rest on the collar. Engage collar chocks to support the crane laterally.
- c. Move the ladder to the second collar, and install a third collar.

Once the crane has been extended to the specified height in phase one, the next phase commences. Phase 2 is shown in **Figure 3**, securing the crane tower to the building. **Figure 3** is a diagrammatic layout of the collar tie and tie beam setup with respect to the crane, and building. This arrangement is typically used at the three locations highlighted in **Figure 1** above.

Phase 2 of jumping the crane includes the installation of the collar tie to the tower of the crane followed

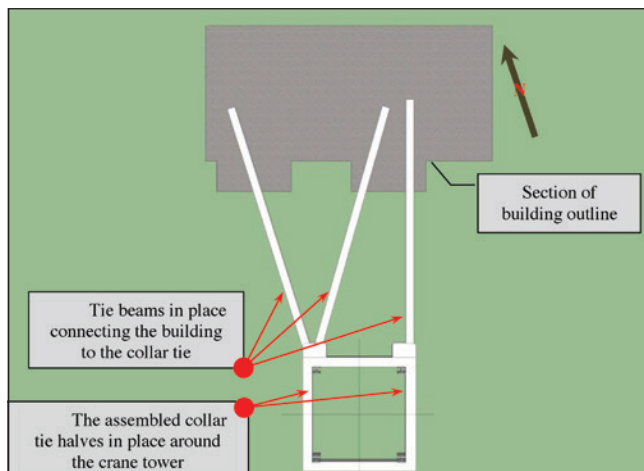


Figure 3

Collar tie and the three tie beams used to secure the crane tower to the building under construction.

by the installation of the tie beams. The collar tie is installed at the predetermined locations in two symmetrical halves using the crane, slings, lever hoist, shackles, and taglines. It was during the installation of the tie beams that the crane collapsed, which occurred some 40 minutes after the collar tie was suspended from the crane tower.

There were four slings used in Phase 2 of the jumping process. The sling that was alleged to have caused the incident is described in the following analysis as “Ex_Lift.” The other three slings involved in the incident were new, and are described as “All_Lift” slings.

Sling Inspection Finds Melted Fibers and No UV Degradation

Synthetic Sling Inspection

The claim made by many experts was that the defective Ex_Lift sling failed, resulting in the failure of three other slings. The 18th floor collar tie fell, triggering the crane collapse. The author’s investigation focused around this allegation made against the company performing the rigging of the collar tie.

Synthetic sling inspection is governed by the Occupational Safety and Health Administration (OSHA). In addition, some key national and industry standards specify inspection requirements. Inspection criteria for polyester synthetic slings are identified in **Figure 4**. A review and comparison of these criteria across the listed organizations show that they are very similar, and the area of focus is highlighted in bold.

Synthetic Web Sling Inspection and Removal from Service Criteria			
REGULATORY AGENCY, OSHA	ASME B30.9 2006 Edition	Manufacturer	Web Sling & Tie Down Association (WSTDA) WS-1 2004 Revision, Compiled
Where any such damage or deterioration is present, remove the sling or attachment from service immediately.	A synthetic webbing sling shall be removed from service if conditions such as the following are present:	The web sling shall be removed from service if any of the following are visible:	A web sling shall be removed from service if any of the following are visible:
Missing or illegible sling identification	Missing or illegible sling identification	Missing or illegible tag	If sling rated capacity or sling material identification is missing or not readable
Acid or caustic burns,	Acid or caustic burns	Acid or caustic burns	Acid or alkalis burn,
Melting or charring of any part of the sling,	Melting or charring of any part of the sling	Melting or charring of any part of the sling	Melting, charring or weld spatters on any part of the web sling
Holes, tears, cuts, or snags,	Holes, tears, cuts, or snags	Holes, tears, cuts, snags or embedded articles	Holes, tears, cut, snags or embedded particles
Broken or worn stitching in load bearing splices,	Broken or worn stitching in load bearing splices	Broken or worn stitching in load bearing splices	Broken or worn stitching in load bearing splices
Excessive abrasive wear,	Excessive abrasive wear	Excessive abrasive wear	Excessive abrasive wear
Knots in any part of the sling,	Knots in any part of the sling	Knots in any part of the sling	Knots in any part of the web sling
Discoloration and brittle or stiff areas on any part of the sling,	Discoloration and brittle or stiff areas on any part of the sling, which may mean chemical or ultraviolet/sunlight damage	Discoloration and brittle or stiff areas on any part of the sling, which may indicate chemical or ultraviolet/sunlight damage	Some visual indications of sunlight or ultraviolet degradation are: <ol style="list-style-type: none"> 1. Bleaching out of web sling color 2. Increased stiffness of web sling material 3. Surface abrasion in areas not normally in contact with the load
Pitted, corroded, cracked, bent, twisted, gouged, or broken fittings, and	Fittings that are pitted, corroded, cracked, bent, twisted, gouged, or broken	Fittings that display excessive pitting, corrosion, or are cracked, bent, twisted, gouged or broken	Excessive pitting or corrosion or cracked, distorted, or broken fittings.
	For hooks, removal criteria as stated in ASME B30.10	For hooks – see ASME B30.10 for removal criteria	
	For rigging hardware, removal criteria as stated in ASME B30.26	For fittings – see ASME B30.26 for removal criteria	
Other conditions that cause doubt as to continued use of a sling.	Other conditions, including visible damage, that cause doubt as to the continued use of the sling	Other conditions and/or visible damage that cause doubt as to the continued use of the sling.	Any other visible damage that causes doubt as to the strength of the sling.
			Proof Testing Warning: Slings used in environments where they are subject to continuous exposure to sunlight or ultraviolet light shall be proof tested to twice the rated capacity semi-annually or more frequently depending on severity of exposure.

Figure 4
Inspection criteria for synthetic polyester sling.

Correctly applying any of the specified inspection requirements is expected to lead to a consistent outcome with regard to sling usability. Thus, the application of these specific criteria and the Web Sling & Tie Down Association (WSTDA) 1994 video resulted in the findings below.

Using **Figure 4** criteria, the inspection of the sling was conducted around May 2010. Following are the findings. **Figures 5** through **8** highlight aspects of the visual inspection conducted on the Ex_Lift sling.

- a. Sling color was uniform, consistent with normal usage, wear, and tear.
- b. The sling surface was dirty, consistent with a construction environment, such as the incident site where the sling was retrieved.
- c. The sling showed two key distinct areas of damage.
 - i. One sling eye was missing. The sling eye was completely severed at stitched location of the three-ply load-bearing splice.
 - ii. There were contact abrasion lines on the face of the sling diagonal to the sling's longitudinal axis.
- d. When the eye of the sling at the stitching was opened up and inspected, the color was consistent with the rest of the sling. A bleached sling typically shows drastic color and texture contrast between the body of the sling and the location where ply of the eyes are sewn together. None was observed.
- e. Bleaching of the sling was not observed or consistent with published standards:
 - i. Regulatory agency
 - ii. ASME
 - iii. Manufacturer
 - iv. WSTDA
- f. The sling stiffness and or brittleness showed no discernable difference when compared to the All_Lift slings that were regarded as new at the time of the incident.
 - i. A brittleness check was conducted on the Ex_Lift sling by rubbing the sling surfaces to dislodge its fibers. No signs of brittleness were detected.
- g. The sheared ends of the sling sections showed a substantial melting of the material fibers.

A similar inspection was done on the All_Lift slings. Besides the structural damage to slings, the findings were unremarkable, including the comparative fading of several of the retrieved sections. The Ex_Lift sling did not show any clear visual signs of UV degradation as claimed by the city's building department report.

Ex_Lift Sling Inspection Findings



Figure 5

Ex_Lift sling section retrieved after crane incident.



Figure 6

Label of the sling is intact, and information is readable.



Figure 7

The intact eye of sling showing wear pad and color consistent with other photos.



Figure 8

Abrasion contact mark on the sling face.

A leading authority on synthetic slings, the WSTDA has produced several publications and videos on slings, including an educational video that shows an inspection protocol for polyester slings with tips for recognition of UV-degraded slings. The excerpts in **Figure 9** and **Figure 10** are examples from the video identifying UV-degraded slings. **Figure 10** shows a comparison of the Ex_Lift sling and a WSTDA UV-degraded sling. Note the distinct bleached appearance of the WSTDA sling versus the intact color of the Ex_Lift sling. The most significant finding from the Ex_Lift sling inspection was that the stiffness and brittleness was comparable to the All_Lift slings that were regarded as newer.

The review and comparison of the Ex_Lift sling to both the WSTDA sling inspection protocol for UV-degraded slings and the newer All_Lift slings showed no UV degradation present, surface abrasion, stiffness, bleaching, or brittleness.

Sling Inspection Inconsistency, New Slings Show Signs of Fading

An inspection of two of the All_Lift sling sections, 2A and 4A, showed similar characteristics to the Ex_Lift sling — color fading, which could have resulted from exposure to water followed by drying. See **Figure 11** through **Figure 13** (items labeled 7A and #11). Of particular interest were two sections of the sling that were faded. Had the larger matching sections not been retrieved, would the inspectors also conclude UV degradation? Bleaching condition of the sling rather than color fading is one measure of UV degradation. To conclude that the two highlighted sections were UV degraded, the other factors would need to be present, including increased stiffness, brittleness, and abrasion. Of course, the obvious fact that the slings were new at the time of the incident excludes the UV findings.

WSTDA 1994 Video Inspection of Ultraviolet-Degraded Slings



Used with permission of the Web Sling and Tie Down Association (WSTDA); © WSTDA 1994

Figure 9

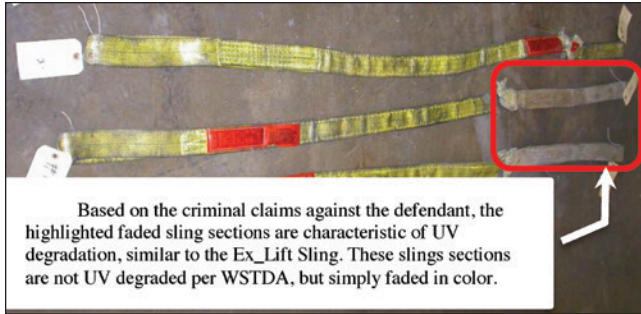
Signs of bleaching, abrasions, stiffness, and brittleness indicated by UV degradation.



Used with permission of the Web Sling and Tie Down Association (WSTDA); © WSTDA 1994

Figure 10

Shows a side-by-side comparison of Ex_Lift sling on the left and bleached UV-degraded sling on the right.



Based on the criminal claims against the defendant, the highlighted faded sling sections are characteristic of UV degradation, similar to the Ex_Lift Sling. These slings sections are not UV degraded per WSTDA, but simply faded in color.

Figure 11

The highlighted faded sections should be regarded as UV-degraded based on the report’s criteria. Color fading was used to evaluate the Ex_Lift.



Figure 12

The retrieved section of the All_Lift slings showing the faded characteristics versus bleaching of the sling.



Figure 13

The faded color of the All_Lift slings, 7A, #12, and #13 shown above did not experience the texture change of stiffness and brittleness that typically accompanies UV degradation.

Sling Inspection Conclusion

Evaluation of synthetic sling failures is very much predicated on several factors laid out by regulatory bodies, consensus standards, and manufacturer associations. Sling fading — used as a criterion to assess the Ex_Lift sling as being UV degraded — is not supported by any of the reviewed documents, including those from the WSTDA. Additional factors would need to be present at the time of inspection and evaluation of the sling to indicate UV degradation conclusively. In **Figure 13**, two of the three All_Lift slings (considered new at the time of the incident) had failed sections that were faded compared to their longer sections. These slings were considered to have been properly stored after the incident. These All_Lift slings were not deemed UV degraded. Slings that are UV degraded not only undergo bleaching, but that bleaching is also typically accompanied by a textural change of the polyester material: stiffness and brittleness. The inspection performed on the slings’ sections that failed showed no visible UV degradation based on the prevailing standards and regulations.

Sling UV Degradation, Regulatory Agency Test Results, and Sling Load Carrying Capacity

Ex_Lift Sling Construction and Data

Figure 14 includes the data from the Ex_Lift sling used in lifting the 11,280-pound collar tie on the crane tower. The Ex_Lift sling is one of four slings used in lifting the collar tie at the time of the tower crane collapse.

One of the key characteristics to be noted is that the polyester webbing used to fabricate the sling is rated at 9,800 pounds/inch minimum — based on the number 9 in the EE292 number in line item 1 of **Figure 14**. The sling webbing is two ply — with each ply 2 inches wide — so the maximum rated strength of the two-ply webbing is 39,200 pounds. This capacity assumes the efficiency of the load bearing three-ply splice stitching and fabrication of the sling to be 100%.

Sling Properties and Characteristics, Manufactured by Ex_Lift		
1	Model	
2	Manufacture Date	07/03/2006
Sling Load Bearing Capacities, Design		
	Hitch	Rated Capacities per Tag, Pounds
3	Vertical	6,400
4	Choke	5,100
5	Basket	12,800
6	Minimum Breaking Strength, 5:1 Safety Factor	32,000 = (5 x 6,400)
7	Ply, minimum number of plies (Splice ply = 3)	2
8	Webbing	Polyester
Sling Rating Based on WSTDA		
8	WSTDA Ply Rating for Class 7 Polyester, Ex_Lift Sling	9,800 pounds/inch
9	Polyester Webbing Design Breaking Strength for Class 7—9,800 pounds/inch width. Total (4 inch x 9,800) =	39,200 pounds, (4 x 9,800 = 39,200 pounds)
10	Fabrication efficiency = 32,000/39,200	~82%

Figure 14
Listing of some properties of the Ex_Lift sling reported to be UV degraded.

Line item 3 of **Figure 14**, the sling strength is 32,000 (6,400 x 5) pounds or a fabrication efficiency of approximately 82% under tensile failure. It is important to note there are no other failure modes, such as shear or compression, identified for the sling. **Figure 15** provides the three lift capacity ratings for the sling in three configurations.

The Ex_Lift sling exceeds the WSTDA WS-1 standard rated capacity for Class 7 polyester sling shown in **Figure 15**. It is important to note that the slings' working load limit (WLL) is based on the webbing material tensile strength and fabrication efficiency. However, there are no equivalent documented shear properties for synthetic slings published. Most slings subjected to shear are based on the sling's configuration and use that is not a characteristic of the synthetic polyester webbing.

Two-Inch Polyester Synthetic Sling-Rated Capacity by Hitch, Tensile Loads in Pounds, WSTDA Comparison			
Sling Manufacturer	Vertical	Choker = 80% of Vertical	Basket
Ex_Lift	6,400	5,100	12,800
WSTDA WS-1 2005 Table 7A	6,200	4,920	12,400

Figure 15
Sling tensile-rated capacity by hitch.

Ultraviolet Degradation

The WSTDA conducted an extensive ultraviolet degradation study of synthetic slings in 1981. Excerpts of the findings are presented below. **Figure 16** shows the UVB radiation by city. Of the U.S. cities shown, Miami has the highest radiation level, which is some 40% greater than New York City.

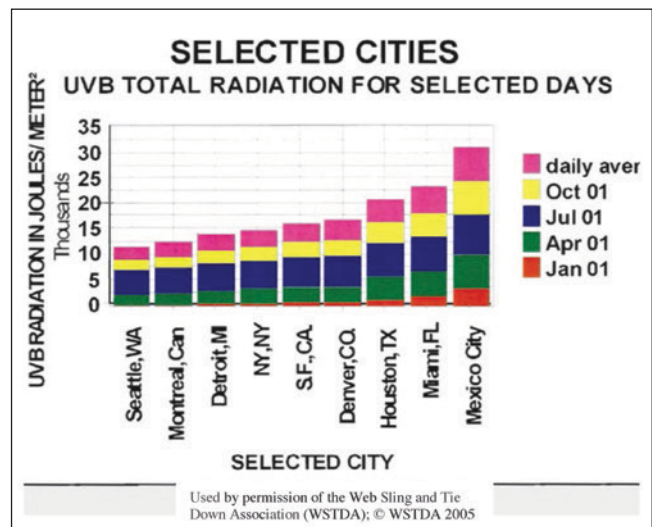


Figure 16
UV energy radiation by location in United States and Mexico. NYC UV radiation energy is approximately 60% of that in Miami.

Based on the WSTDA study, the Ex_Lift sling would have had to be sitting in the New York City sunlight for some 20 continuous months to have an equivalent 12-month UV exposure to Miami radiation or in some equivalent environment.

Figure 17 shows the reduction in breaking strength measured in WLL versus months of UV exposure. The maximum loss in WLL occurs around 12 months of exposure for polyester slings. Further exposure to UV radiation did not show any appreciable degradation below 3.7 times the WLL in 36 months. After 12 months of UV exposure, the breaking strength of the sling has

been reduced by approximately 26%. The WSTDA test establishes a relationship between UV exposure and reduction in sling strength for polyester synthetic slings through destructive testing. Because the subject sling was manufactured on 07/03/2006 — and the incident occurred on 03/15/2008 — the worst-case UV exposure can be estimated at approximately 20 months in New York. Given this worst-case assumption, the reduction in tensile strength can be estimated. The decline in design factor can be estimated from 5 to 1 — to a safety factor of approximately 3.7 to 1. The breaking strength of the Ex_Lift polyester slings exposed to UV radiation can be estimated from **Figure 17** as 3.7 times WLL, which is equal to 3.7 x 6,400 pounds or 23,680 pounds. The strength retained by the assumed UV-exposed sling exceeds the proof load test of 200% of the WLL or 12,800 pounds required by manufacturers and the WSTDA for slings consistently used in a UV environment. The proof load testing of slings used in a UV environment confirms that there is no clear non-destructive method of establishing any level of UV degradation for a synthetic sling.

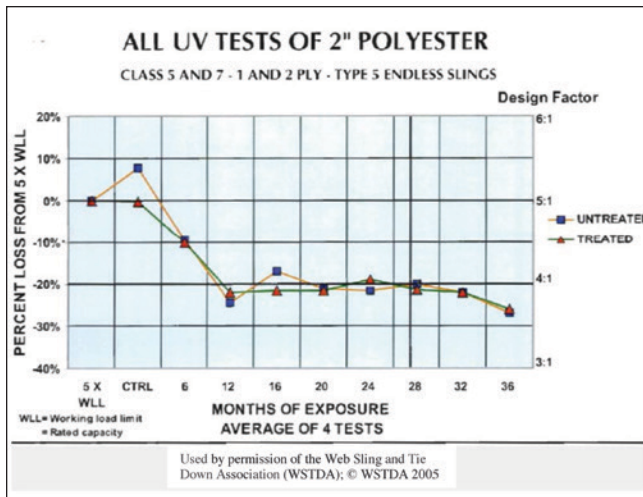


Figure 17

WSTDA graph of breaking strength loss versus months of continuous UV exposure.

A review of the manufacturer’s documentation notes that slings used in environments where they are subject to continuous exposure of ultraviolet light should be tested to two times their rated capacities annually — or more often, as required. The test requirement recommended by manufacturers recognizes that UV degradation presented in **Figure 17** primarily affects the breaking strength of the sling and not necessarily the WLL. Any sling in use that is successfully tested to twice its WLL does not validate or verify UV degradation in that sling. However, the tested sling does

have a lift capacity sufficient to handle loads up to (and including) its WLL. UV degradation in exposed slings is confirmed through destructive pull testing. To that end, UV degradation claims must address the following findings as well as the residual strength of the sling noted above. A list of UV degradation issues that were not directly addressed in the crane incident by experts were as follows:

- The length of time the Ex_Lift sling was exposed to UV degradation.
- UV radiation exposure by geographic location (New York versus Miami) are not all equal.
- Polyester slings experience a 26% reduction in breaking strength (maximum).
- UV-degraded polyester slings are tested to tensile failure and not shear failure.
- UV degradation in slings is verified through destructive load testing.
- Manufacturers and industry standards recommend load testing of slings subjected to UV degradation.

The UV degradation claim against the Ex_Lift sling was virtually silent on the above items.

Collar Tie Sling Load Distribution Upper and Lower Limits for Ex_Lift Sling

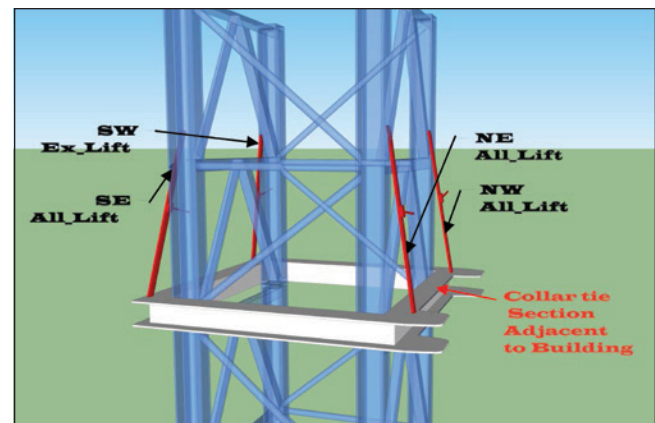


Figure 18

The arrangement of the 11,280-pound collar tie, crane tower, and rigging.

Based on **Figure 18**, the distribution of collar tie weight (11,280 pounds per the manufacturer) on the four slings was unknown at the time of failure. However, an upper and lower limit to the sling loads could

be established for the sling in the SW location. The ideal load configuration assumes the total weight of the collar is distributed on the four slings based on the center of gravity and the collar tie symmetry about the center of gravity. The second sling load configuration addressed was based on industry practice where two slings are predominantly carrying the weight of the collar tie. **Figure 19** summarizes the sling load estimates for the two configurations.

Estimated Sling Load Distribution by Crane Tower Location, Pounds				
Sling Location	NW	NE	SW	SE
Ideal Load Configuration	3013	3013	2627	2627
Industry Practice	407	5631	5242	Sling Detached

Figure 19

The load limits on the slings for two configurations.

For ideal load configuration, the SW sling sees a load of approximately 2,627 pounds — much less than the 5,100 pounds the sling is rated for in a choker hitch. For the worst-case load condition, the Ex_Lift choker hitch saw a load of 5,242 pounds or 142 pounds in excess of the sling's rated capacity in a choker hitch. The Ex_Lift sling was reported to be positioned in the SW location on the crane tower. The loads experienced by the Ex_Lift in either configuration did not approach the UV-degraded failure loads: 3.7 x 6,400 or 23,680 pounds, noting the weight of the collar was only 11,280 pounds.

Deficiency of Regulatory Agency-Sponsored Sling Test

The regulatory agency sling test was designed to evaluate the actual configuration the slings were used in lifting the collar tie and the actual tower crane section involved in the incident. The test evaluated nine new All_Lift polyester slings and three new Ex_Lift polyester slings. The test configured the polyester sling in a choker hitch around the tower crane leg and between the support structures as the sling was used on the day of the incident. Absent from the test setup used to pull test the slings was the lever hoist that was an actual part of the collar tie lifting arrangement at the time of the incident. The regulatory agency-sponsored test setup is shown in **Figure 20**.

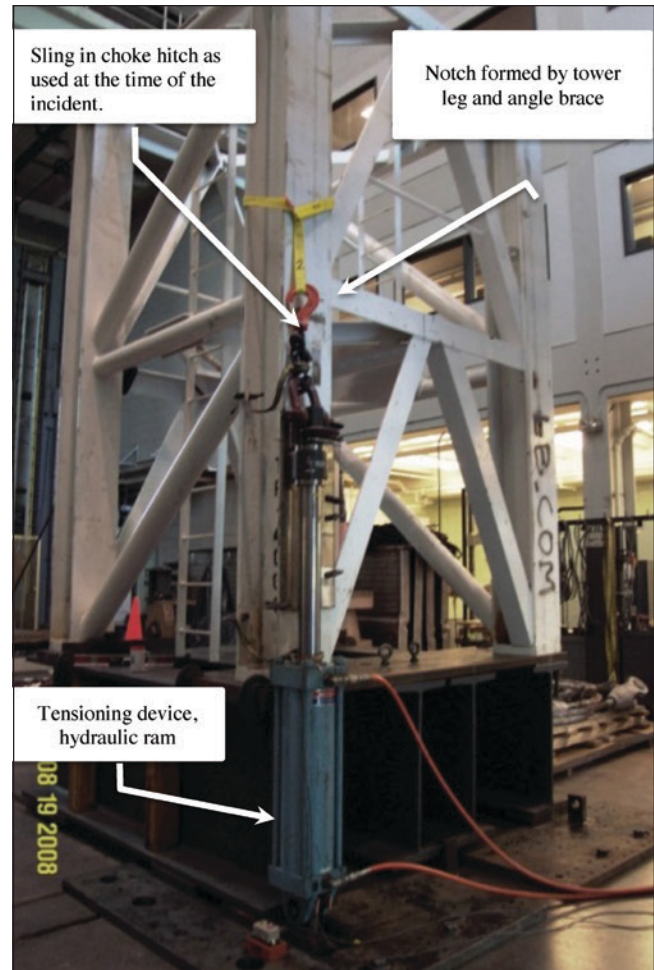


Figure 20

The setup used in the regulatory agency-sponsored test.



Figure 21

Typical sling pulled to failure. The slings failed at the stress riser, as expected.

Figure 20 shows the sling arranged in a choke hitch around the leg of tower section. The sling transits a notch formed by the leg of the crane and the angle brace. The notch is a stress riser on the sling as a load is applied to the sling. The inspection completed on the tower by the testing lab was silent on defects that would

contribute to additional stress risers on the EX_Lift sling. An observation to point out here is that the sling tests utilized the same tower section and sling locations as at the time of the incident. Hence, the effects of any stress riser anomalies would be consistent between the sling tests and the incident. The tests were conducted on different corners of the tower, which ruled out any anomalies in the notch of the SW corner.

A summary of sling test results conducted under regulatory agency sponsorship is presented in **Figure 22**. Test number 4, 5, and 7 are the results from exemplar Ex_Lift slings. In each case, the test load exceeded the rated capacity of 5,100 pounds. More importantly, test 7 showed the Ex_Lift sling was able to sustain a minimum of 9,887 pounds. This failure load would

have exceeded its share of the collar weight by more than 4,000 pounds if only three slings were used to support the collar tie per industry rigging practice.

Figure 23 presents the load comparison for the subject sling. The test loads obtained by the regulatory agency-sponsored test exceeds the loads the sling experienced lifting the collar tie. In addition, the capacity of the assumed UV-degraded Ex_Lift sling exceeded the regulatory agency test load by more than a factor of two.

However, the test failed to capture one key characteristic that was very evident at the time of the sling inspections and discussed in the textile expert’s report — the substantial melting of the fibers found at the sheared or abraded surfaces of the slings.

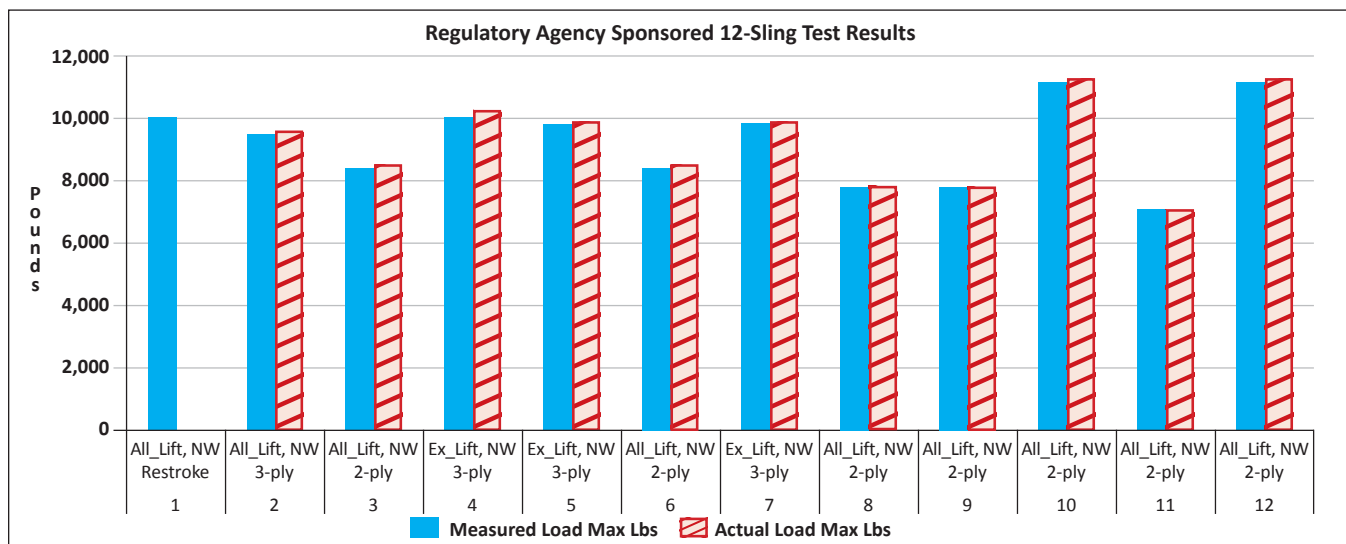


Figure 22
Results of the regulatory agency-sponsored test.

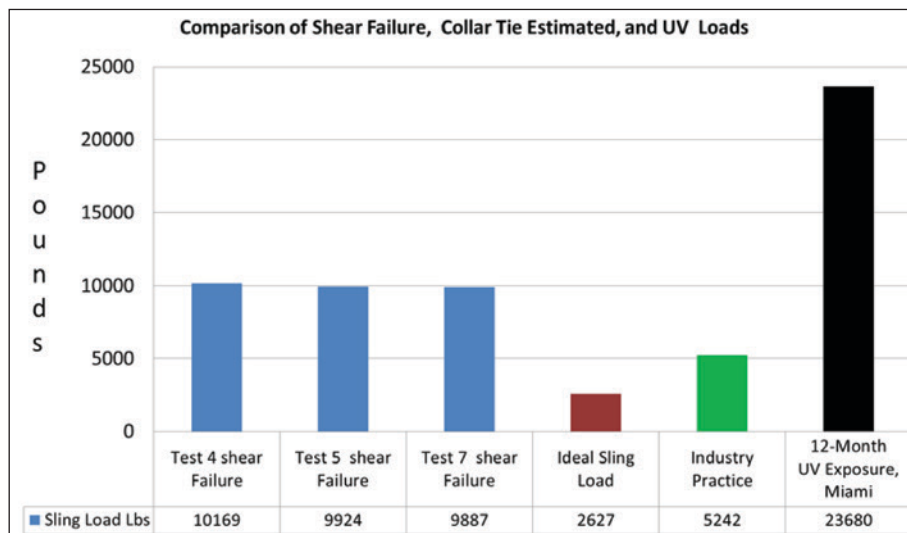


Figure 23
Test load comparison versus slings loads and UV-degraded sling safety factor.

Regulatory Agency-Sponsored Sling Test Limitations

Pictures of sling tests 2 and 4 are presented in **Figure 24** and **Figure 25**, respectively. In each case, the failed surfaces show distress from contact with the crane tower leg and the notch. The abraded and sheared surfaces are consistent with the mechanical failures of the slings retrieved at the incident site. However, neither of the tested slings shows any melted fibers consistent with the slings retrieved at the incident site. The lack of melted fibers across all tested slings suggests that the regulatory agency-sponsored test did not capture the sling's failure process at the time of the incident.

The regulatory agency-sponsored sling test results captured in these photos are regarded as slow-speed failures. These tensile tests were on the order of 10 to 15 minutes in duration in some cases.

The Ex_Lift sling test 4 and 5 conducted on behalf of the regulatory agency had recorded failure times of

1,083 and 1,041 seconds, respectively — a failure rate that is a couple of thousand times slower than a nominal failure time to produce melting of the sling fibers. This failure process that results in melting of the fibers (as noted at the time of the inspection) is called the adiabatic process (defined below).

Adiabatic process: *A thermodynamic process in which there is no transfer of heat between the working substance and the surroundings. An adiabatic process is one that is so rapid that no heat is lost, and the temperature rises accordingly.*

The slings' melted fibers are the strongest evidence that the crane failure is unrelated to the slings and sling configuration used on the collar tie.

In the inspection of the sling designated 2A melted fibers were easily visible, as shown in **Figure 26**. None of the tests conducted on behalf of the regulatory agency showed any level of melted fibers on the sheared ends.

#2, All_Lift Sling Test Visual Results

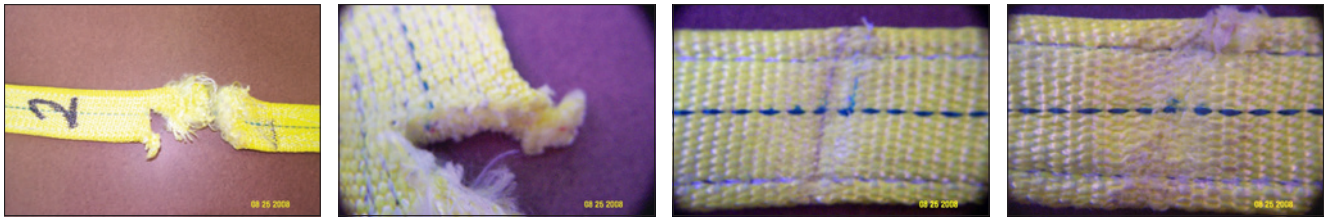


Figure 24

Pictures of the sheared or abraded surfaces of All_Lift Sling #2 test. Note no visible signs of melting on the surfaces.

#4, Ex_Lift Sling Test Visual Results

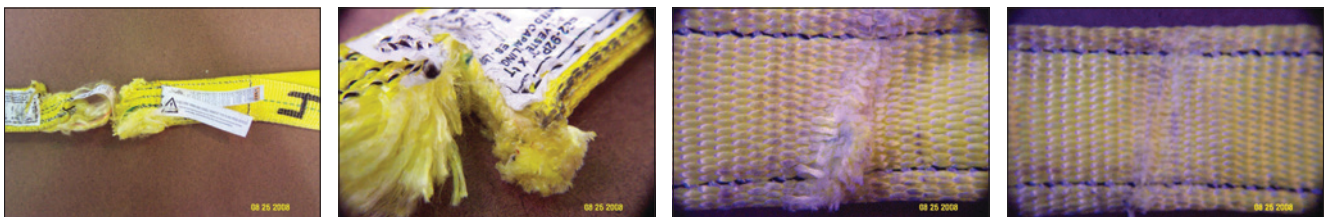


Figure 25

Pictures of the sheared and abraded surfaces of Ex_Lift sling #4 test. Note no visible signs of melting on the surfaces.

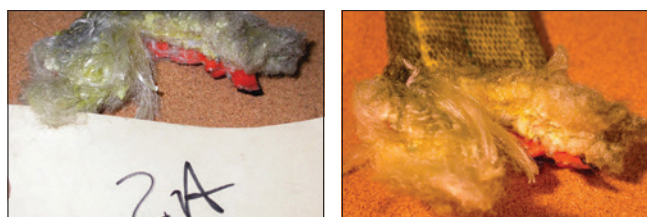


Figure 26

All_Lift Sling 2A sheared surface showing some melted fibers as well as frayed fibers that are a result of tensile failure.

Inspection of All_Lift sling section 4A in **Figure 27** was one of two sections with the greatest amount of visible melted fibers across the sheared surface. Failures of the type shown are typically characterized by rapid application of a tensile load while the material is subject to shear or abrasion. The entire process lasts a fraction of a second, and the melted fibers are a result of the thermodynamic adiabatic process.

The actual sling failure mechanism is similar to the regulatory agency-sponsored test in that they are both shear failures. However, the failure process for the actual slings is thermodynamically different in the application rate of the failure-inducing load. The regulatory agency-sponsored test of the 12 slings is regarded as an isothermal process (constant-temperature process). The rate of application of the test load is more than several minutes, such that the sling temperature remains at or close to ambient. In the case of the sling section 4A, the entire failure process shown in **Figure 27** may be less than a millisecond. In the rigging industry, this type of rapid loading of slings and equipment is called shock loading.

Figure 27 shows the sheared failure surfaces of All_Lift sling sections 4A and 7A. The failure process is similar to that of **Figure 26**, sling section 2A.

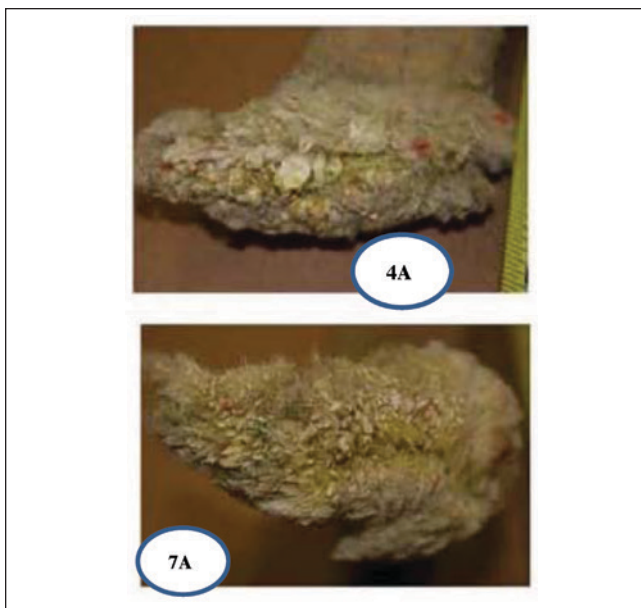


Figure 27
Sheared surfaces of All_Lift sling pieces 4A and 7A.

Figure 28 below shows section #12 and #13. The melted fibers are visible and stands in contrast to the frayed fibers located toward the edge of the sling sections.

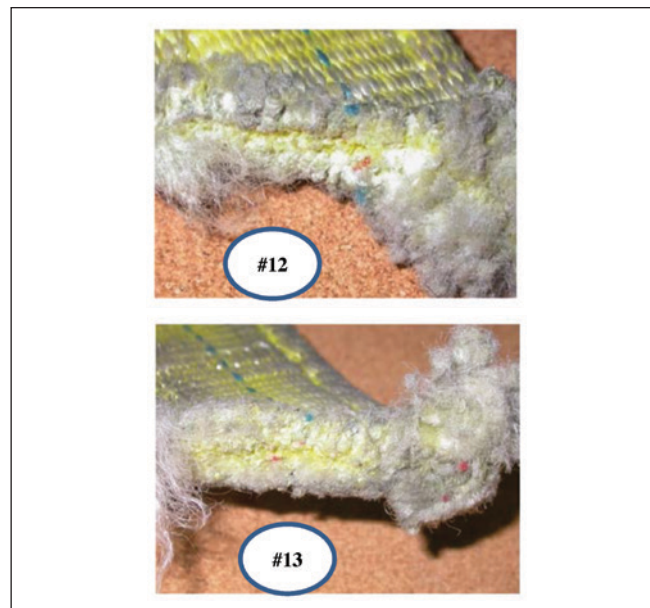


Figure 28
Two All_Lift sling sections #12 and #13. High-speed shear failure process is predominant in both sections.

Finally, **Figure 29** shows two failed sections of the Ex_Lift sling. The top section is the three-ply shear failure surface, and the bottom section is the high-speed abrasion resulting from contact between the sling

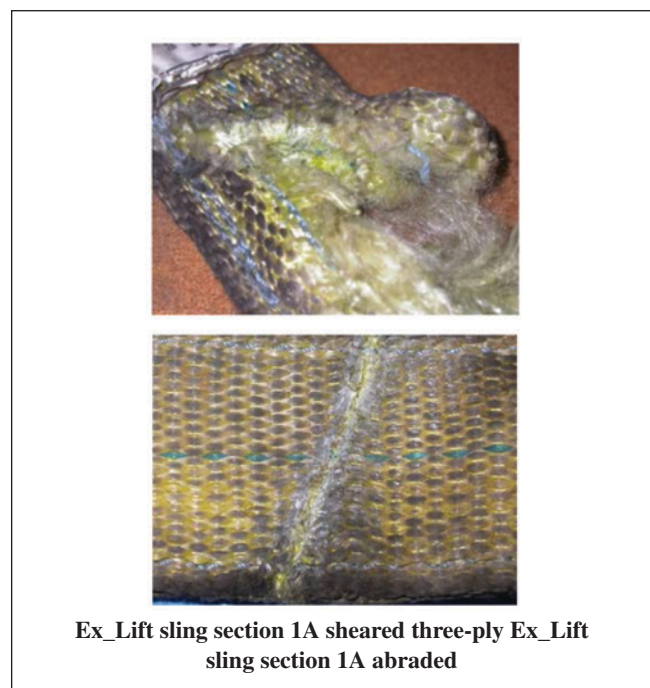


Figure 29
Above is the Ex_Lift sling section 1A, a three-ply adiabatic shear failure with melted fibers. Below is the Ex_Lift sling section 1A with adiabatic abrasion damage.

surface and the edge crane tower leg. The melted fibers are clearly visible to the unaided eye. At the time of inspection, the melted fibers covered more than 70% to 75% of the sheared surface. The common failure process across sling sections 2A, 4A, 7A, #12, and #13 is adiabatic. The long extended frayed fibers are evidence of slow-speed tensile failure that is considered to be a less relevant failure mode based on the amount of material frayed — and one that followed the high-speed failure.

Position of Sling Sections on the Collar Tie and Tower, Rigging Setup

Several incident site photographs were reviewed to determine where sling sections were located just prior to the incident. **Figure 30** shows the SW (southwest) corner of the collapsed crane tower. Suspended from the crane tower section is the Ex_Lift sling 1A attached to the lever hoist.



Figure 30
SW corner with Ex_Lift sling 1A. Visibly extended fibers are evidence of slow-speed failure.

In **Figure 31**, All_Lift sling section 2A is suspended from the collapsed tower. This section combines with All_Lift section 11 to form a complete sling. Note: This sling was the only All_Lift to have been damaged at the red identification tag. In **Figure 32**, sling #12 and #13 identification tags are intact and undamaged.

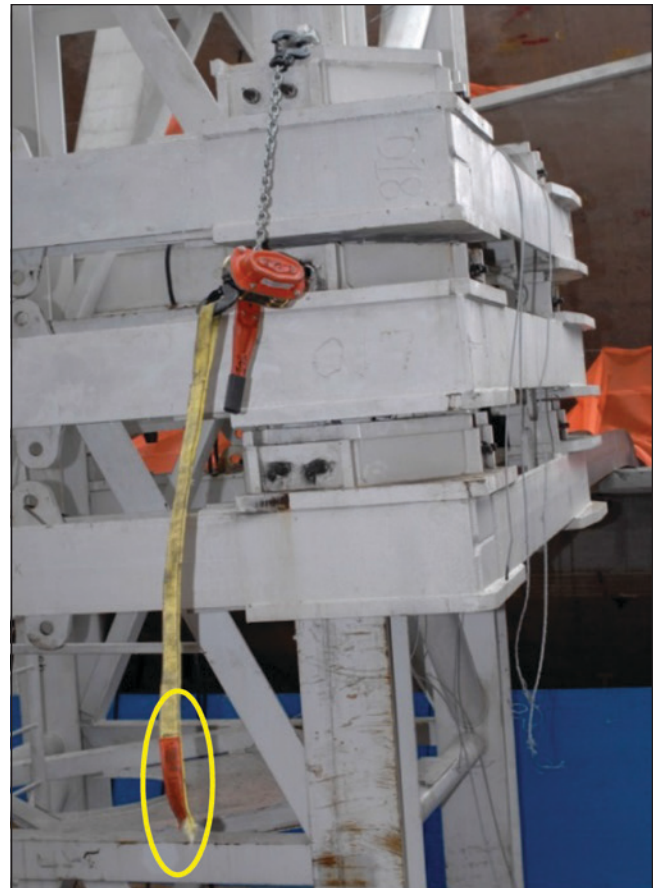


Figure 31
SE corner with All_Lift sling 2A. Extended fibers are evidence of some slow-speed failure as well.



Figure 32
Sling sections retrieved from the incident site. A total of seven sections were retrieved. The Ex_Lift sling 1A, All_Lift slings 2A, 4A, 7A, #11, #12, & #13 tagged and labeled.

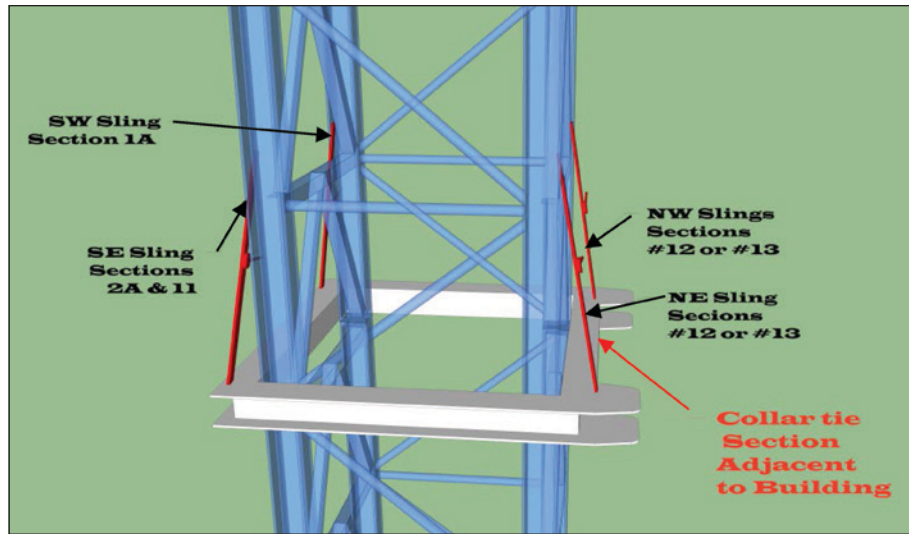


Figure 33
Diagrammatic representation of a section of the crane tower, the collar tie, and sling-lever hoist combination used to rig the collar tie.

Sling + Lever hoist	Manufacturer	Slings Marked	Matching Section	Tower Reference	Leading Failure Mode
NW Sling	All_Lift Sling	#12 or #13	4A or 7A	Building	Shear, high speed, adiabatic
NE Sling	All_Lift Sling	#13 or #12	7A or 4A	Building	Shear, high speed, adiabatic
SW Sling	Ex_Lift Sling	1A	Not retrieved	Road	Shear, high speed, adiabatic, tensile min
SE Sling	All_Lift Sling	2A	#11	Road	Shear, high speed, adiabatic, tensile min

Figure 34
The sling sections retrieved from the incident site, predominant failure modes, and their relative location on the crane tower.

The remaining sling sections #12, #13, 4A and 7A are located on the north side of the crane tower closest to the building to which the crane was attached. In other words, these sling sections were rigged to the collar tie and crane tower closest to the building. The sling section arrangements are shown in **Figure 33** and **Figure 34**.

Based on the adiabatic failure process experienced by the slings that rigged the collar tie to the crane tower, the NW, NE, and SE slings failed before the SW sling. The SW Ex_Lift sling showed substantial slow-speed tensile failure, as can be seen by the frayed extended fibers circled in **Figure 28**.

The analysis presented in foregoing sections shows the following findings: UV degradation (if it were to exist) had no effect on the sling capacity compared to the load imposed by the collar tie; the regulatory agen-

cy sling test showed that the capacity of the exemplar Ex_Lift sling exceeded the load imposed by the collar tie; the regulatory agency sling test reproduced the mechanical failures of the slings but did not reproduce the adiabatic failure process experienced by slings at the time of the crane collapse; and the adiabatic failures analysis established that the slings' failure began on the side of the crane tower closest to the building under construction.

Defense Test Supports Sling Strength Findings

The defense conducted a sling test using the following exemplars: a collar tie, crane tower section, and sample of three new All_Lift slings and a used Ex_Lift sling — manufactured on the same date as the one used on the day of the incident. The scope of the test was to produce the failure modes and failure process the slings experienced at the time of the incident and reconcile the regulatory agency-sponsored test results, the textile

expert's report, and the simulation of UV degradation in one of slings. The test used a section of the crane tower similar to the regulatory agency-sponsored test and the collar tie from the 18th floor. The collar tie was rigged in a similar manner as the day of the incident.

The test examined the following rigging configurations:

- a. Four slings supporting the collar tie for a specified duration — the actual rigging arrangement at the time of the incident.
- b. Three slings supporting the collar tie to assess whether or not the slings had the capacity to support the collar tie in this configuration for a specified duration.
- c. Four sling supporting the collar with a greater than a 50% cut in the width of Ex_Lift sling to replicate the effects of the UV degradation that were alleged at the time of the incident.

- d. Finally, cutting the Ex_Lift sling 100%, simulating the alleged sling failure that resulted in catastrophic collapse of the crane.

Tests c and d were completed on the heavier end of the collar tie, hence using a more severe approach than the claim that the sling on the SW corner of the crane tower failed first.

a. Collar Tie Sling Test Demonstration Setup

Figure 35 through **Figure 45** show the assembly and setup of the crane tower as well as the installation of the collar tie halves in preparation of the first test.



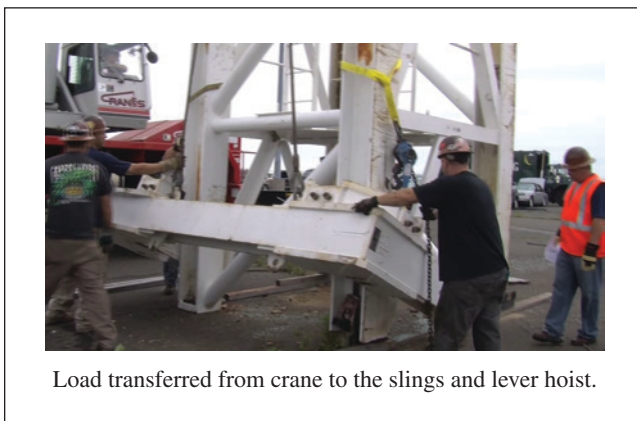
Standing up tower section vertically.

Figure 35
The setup process, tower section.



Installation of sling lever hoist to crane tower leg.

Figure 36
Sling arrangement used to support collar tie.



Load transferred from crane to the slings and lever hoist.

Figure 37
Installation of the collar tie half.



Crane slings slack carrying no load of collar.

Figure 38
Collar tie half transferred from the crane to slings.



Slings from support crane removed from collar tie.

Figure 39

Support crane sling disconnected, and test slings carry the collar tie half.



Collar tie section completely supported on crane tower.

Figure 40

Collar tie half supported by the slings.



Adjusting lever hoist in place to align bolted faces of collar tie.

Figure 41

Two additional slings attached to level the collar tie half.



Second collar tie being setup for bolt up alignment.

Figure 42

Second collar tie being rigged for alignment.



Not a clear view of two of four lever hoist required to assemble the bolted faces of collar tie.

Figure 43

Second collar tie rigged with slings for alignment.



The assembled collar tie bolted out with one of two lever hoist sling combination attached at the bolted face, a manufacturer requirement.

Figure 44

Alignment completed with additional slings disconnected.



Fully assembled collar tie suspended from the crane tower per report.

Figure 45

Collar tie rigged and suspended by four slings.

b. Testing Demonstration



Figure 46

Collar tie test in progress.

Figure 46 shows the completed assembly of rigging and collar tie suspended for approximately 40 minutes to match the elapsed time to failure of the actual setup on the day of the incident. The elapsed time contradicts regulatory agency conclusions that once the collar tie is rigged, the continuous elongation of the polyester slings would require adjustment, hence making synthetic slings incorrect for this rigging operation — no violation of Hooke’s law here.

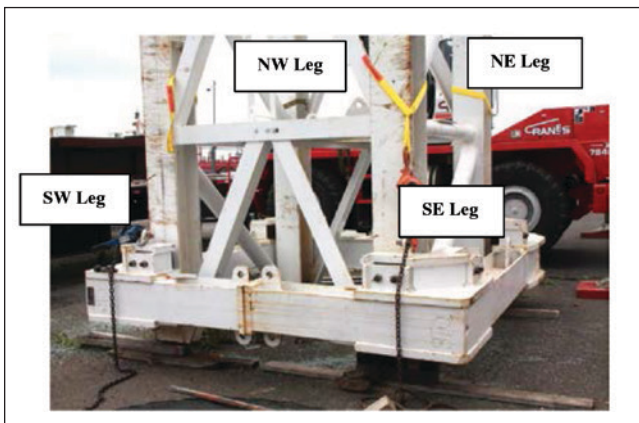


Figure 47

Collar tie suspended from three slings with the SW sling disconnected.

Figure 47 shows the disconnected sling at the SW leg of crane tower. The removal of this sling from the collar tie corresponds to the sling that allegedly failed first, resulting in the failure of the remaining three slings followed by crane collapse. This configuration results in the slings (Ex_Lift sling and All_Lift sling) adjacent to the disconnected slings carrying close to 90% of the collar tie load. This test condition was sustained for more than 20 minutes. The sling directly opposite of the disconnected sling carries a few hundred pounds to balance the collar tie. Based on the geometry of the collar tie, the center of gravity is toward the mobile crane in the background of Figure 45.

This test confirmed no catastrophic failure resulted because two slings are capable of carrying the weight of the collar tie with substantial reserve in lifting capacity in the remaining three slings. The industry practice for handling indeterminate load distribution on slings in Figure 19 predicted this test result.

c. Sling Cut Test

The sling cut test was designed to simulate a sling that was impaired due to UV degradation. The WSTDA sling tests showed slings exposed to UV degradation up to 36 months experienced a reduction of the design



Figure 48

Loaded sling being weakened by cutting.



Figure 49

Weakened sling was cut beyond half its width, weakening more than 50%.

factor of safety. The factor of safety goes from a 5 to 1 on the WLL (ideal) to approximately 3.70 to 1.

The Ex_Lift sling shown in **Figure 48** and **Figure 49** was cut more than 50% of its width (the double blue tread along the width of the sling is regarded as the sling's center line) using a utility knife. The collar tie remained suspended in equilibrium after more than 20 minutes.



Figure 50

Ground clearance is maintained during the static tests using four sling and subsequent three slings.

During the tests performed on the sling, collar tie, and tower, the clearance between the rigged collar tie and the ground was maintained, as shown in **Figure 50**. The clearance between the ground and the collar tie was estimated to be between 14 to 18 inches. Maintaining clearance between the ground and collar tie was essential to ensure the four slings were carrying the total weight of the collar tie. The situation was continuously monitored during each phase of the test.

d. Dynamic Test

Finally, the dynamic test was completed. The initially cut section of the Ex_Lift was cut through the remainder of the way. A sudden drop of the collar tie was experienced, though the three remaining slings did not catastrophically fail. The key factor associated with this test was not only to determine whether the remaining slings would fail in shear but also to assess the failure process.



Figure 51

Shock load being applied to the collar tie rigging.



Figure 52

Post shock load configuration of the suspended collar tie. The collar dropped an estimated 8 inches.

The sling cut, as shown in **Figure 51**, resulted in a dynamic load to the entire system of remaining slings. Additionally, the northwest corner of the collar tie dropped some 8.5 inches, remaining clear above the ground as shown in **Figure 52**. This equilibrium condition was sustained for more than 15 minutes. During the 15 minutes of equilibrium, the remaining slings showed no further elongation.

Sling Test Results

The dynamic test where one sling was cut to replicate a weak, UV-degraded sling was incorrectly performed. The sling that was to be cut was the All_Lift sling located diagonally opposite the Ex_Lift sling. However, by cutting the Ex_Lift sling, the effect was more severe because the Ex_Lift was located on the heavier end of the collar tie. The cutting of this sling dynamically imparted a larger shock load into the remainder of the three slings. The results of the collar tie dynamic test are shown in the photographs. Compared to the regulatory agency-sponsored sling tests and the actual sling failures, the results are unremarkable. The Ex_Lift sling was sheared less than $\frac{1}{5}$ its width for the section placed in the notch area after being cut by the

utility knife. The All_Lift sling A, as shown in **Figure 53**, adjacent to the Ex_Lift sling B, is on the heavier end of the collar tie. This sling experienced the worst damage of all the slings. This result is expected because the All_Lift sling is one of the two slings carrying the total load of the collar tie. This sling carried about 55% of the total weight of the collar tie after the shock load — it should be noted that shock loads increase loads shared by the slings conservatively by an order of magnitude of 2, minimally.

The results, though expected, are far less remarkable when the failure process is considered. None of the partially sheared surfaces showed visible signs of melted fibers. The melted fibers are the by-product of synthetic fibers undergoing rapid failure that last for milliseconds perhaps — consistent with no heat transfer between the failure surfaces and the environment.

Post Test Results and Conclusions

The following five pictures show the damage to the slings that resulted from the dynamic test. The cuts are less than 50% of the sling width. The damage to the slings was a result of the slings being placed in the notch. The Ex_Lift sling damage in the three-ply area was restricted to shear.

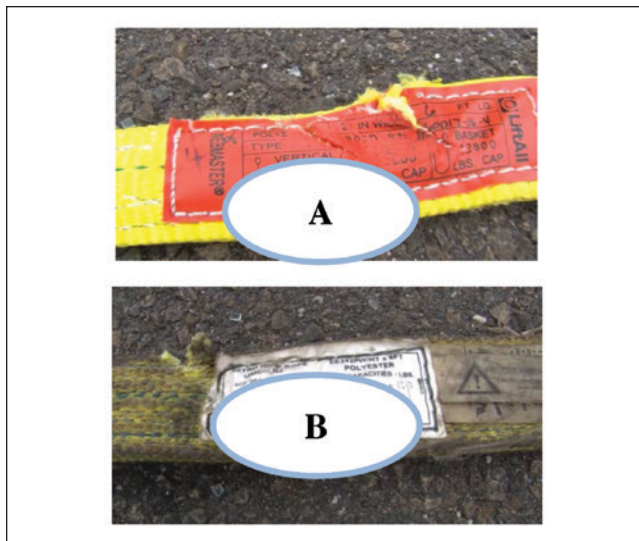


Figure 53

Damage sustained by tested slings. No ultimate slings' failure occurred after one sling was completely cut.

The conclusions of the defense collar tie test were:

- The slings were capable of supporting the collar tie with reserve capacity.
- The disconnection of one sling (this equates to a bad sling) from the collar tie showed the

remaining three slings had the capacity to carry the weight of the collar tie.

- The dynamic shock load was less conservative than the New York Department of Buildings' report non-linear analysis. The resulting failure was not enough to cause catastrophic failure of three remaining slings and the ultimate collapse of the crane.
- Most importantly, the damage to the slings showed no visible adiabatic failures that are predominant in the actual sling failures.
- The slings showed no appreciable elongation after the shock load; the length measured approximately 72 inches. This finding is contrary to the regulatory agency's expert who noted that these synthetic slings would continue to stretch (violation of Hooke's Law), given their application of lifting the collar tie (a fixed weight).

Conclusions

The findings of the investigation and analysis did not support the claims that the Ex_Lift sling was defective (due to prolonged UV degradation) and lost its lift capacity to support its share of the collar tie weight. The conclusions are as follows:

- The sling inspection confirmed no visible indications of UV degradation were present.
- A 36-month, UV-degraded polyester sling had an estimated breaking strength of 3.7 times WLL, which was 4.5 times the worst-case loading of the failed sling.
- The regulatory agency-sponsored load test confirmed the All_Lift slings alone had more than adequate lift capacity to support the collar tie — had there been a compromise to the Ex_Lift sling.
- The regulatory agency-sponsored test adequately showed that mechanical failure modes of the tested slings were similar to the slings recovered from the incident.
- The regulatory agency-sponsored tests were isothermal, and they failed to replicate the adiabatic failure process of the slings involved in the incident.
- The defense sling test confirmed the regulatory agency-sponsored test:

- i. Four slings supported the collar tie.
- ii. Three slings supported the collar tie with one sling carrying as little as 407 pounds.
- g. The defense sling test showed that shock loading the collar tie and slings did not cause the collar tie to fall and the likely collapse of the tower crane.
- h. The defense sling test confirmed that the imparted shock load to the collar tie slings was insufficient to cause the melting of the sling fibers at the sheared surfaces.

Bibliography

- 2008-07-24_Telephone Record - NYCDOB OSHA. DOC. Verbal communication among participants on Regulatory Agency Test.
- AS 1418.4-2004, Cranes, hoist and winches. Australian Standard.
- ASME B30.9-2006. Slings. New York; American Society of Mechanical Engineering.
- DuPont. Properties of DuPont industrial filament yarns – Multifiber Bulletin X-273. Overland Park, KS: DuPont; April 1993.
- Irwin D. Mechanical engineer's handbook. San Diego, CA: Academic Press; 2001.
- nyc.gov. New York: City of New York; March 2009. http://www.nyc.gov/html/dob/downloads/pdf/51streetcraneinvestigation_all.pdf
- OSHA 29 CFR 1910.184(i). Synthetic web slings. Washington, D.C.; Occupation Safety and Health Administration.
- WSTDA training inspection video. Forest Hill, MD; Web Sling and Tie Down Association: 1994.
- WSTDA-UV-MM-2005. UV degradation mini manual. Forest Hill, MD; Web Sling and Tie Down Association.
- WSTDA-UVDR-1981, (Revised 2005). UV degradation report. Forest Hill, MD; Web Sling and Tie Down Association.
- WSTDA-UV-Sling-2003. Summary report UV degradation. Forest Hill, MD; Web Sling and Tie Down Association.
- WSTDA WS-1 standard 2004. Forest Hill, MD; Web Sling and Tie Down Association.

Forensic Engineering Analysis of Dynamic Forces Created by Pedestrians Impacting Plate Glass at Different Speeds

By Michael Kravitz, P.E. (NAFE 451F)

Abstract

This paper examines the effect of a pedestrian inadvertently impacting a glass panel adjacent to a glass exit door. The glass panel was full length and unmarked, violating the local building code and building commissioner directives. The defense argued that the old building code, to which the college building was constructed, was “grandfathered” and there was no violation. Initial witness and plaintiff statements indicated that the plaintiff was running when he struck the panel, which shattered and caused the plaintiff to incur injuries. The plaintiff testified later, in deposition, that he was walking when he struck the glass. The court needed to establish liability percentage, which is common in civil cases, and it was necessary to determine at what pedestrian impact speed the glass panel would break. The analysis used Timoshenko’s theory of vibration plates, Roark’s stress strain formulas, ergonomics, and human factors to estimate the impact load and stresses on the glass panel that caused failure.

Keywords

Glass, vibration, building code, directives, differential equation, ergonomics, human factors

Case Description

The plaintiff had received a message that a family member had just been taken to the hospital, and he was descending the stairs of a state-owned college building. Adjacent to the double exit doors were full-length unmarked glass panels that were in-line with the stair route. The plaintiff reached out, arm fully extended, and pushed on the unmarked glass side panel, thinking it was the exit door. The glass panel was not made of safety glass (annealed glass), and his arm pushed at approximately the center of the panel. It broke in shards, causing severe cuts along his wrist and forearm. EMS was called, and the plaintiff was taken to the hospital. He stated to EMS and building security guards that he was running down the stairs, while on his cell phone, and thought that the panel was the door (see **Figure 1**).

Plaintiff Argument

The plaintiff engaged an expert engineer who claimed that the unmarked glass panel violated certain sections of Industrial Board of Appeals Chapter 1 Part 47 and, in particular, Part 47.8. The plaintiff’s Expert cited codes from the current 2008 laws — the year the incident occurred — and wrote:

“...which stated that the fixed glass panel was clear and gave the optical illusion as if it did



Figure 1

The photo shows the view of the stairs, landing, exit doors, and glass panel that was impacted by the plaintiff as he was descending the stairs. The trash containers were not in front of the glass panel at the time of incident. The photograph was taken at the time of the inspection; therefore, the panel had been repaired.

not exist, and gave the impression that there was a straight walking distance to the outer lobby. It should be noted that that transparent glass doors and fixed adjacent transparent glass sidelights shall be marked in two areas of the glass surface thereof. One such area shall be located at least 30 but not more than 36 inches and the other at least 60 but not more than 66 inches above the ground, or floor or equivalent surface below the door or sidelight.”

“...that the New York State Labor Law Section 241-B requires that all transparent glass doors in mercantile establishments and in public and commercial buildings and structures shall be marked in such a manner as shall be calculated to warn persons using the same that such doors are glass doors.”

After the plaintiff retained his lawyer, he cited in his deposition and all subsequent dialogs that he was “walking.” Therefore, he retracted his earlier statement that he was running, and changed it to walking.

Defense Argument

The author researched the building department website and discovered that the building was constructed circa 1962 under the 1938 Building Code of the City of New York — where there was no requirement for glass markings on doors or side panels.

The defense attorney’s theory of the case was that the unmarked glass side panel was “grandfathered” in the building code because the old building code was silent regarding glass panel markings. However, the building commissioner issued a directive in 1961, which became part of the labor law, requiring glass side panels adjacent to glass exit doors to be marked.

These directives were made public when issued and served as clarifications of the building code by the commissioner of buildings. The glass door and side panel markings directive went into effect on Jan. 1, 1968.

The Department of Labor industrial commissioner issued a directive as Part 47 of Title 12 of the Official

Compilation of Codes, Rules and Regulations of the State of New York, cited as 12 NYCRR47, Transparent Glass Doors in Mercantile Establishments and in Public and Commercial Buildings and Structures (see **Figure 2**).

The City of New York Housing & Development Administration Department of Buildings		Glass Doors, LL Section 241-b
<u>DEPARTMENTAL MEMORANDUM</u>		
TO: Borough Superintendents	DATE: February 6, 1968	
FROM: Julius W. Schneider Director of Operations	SUBJECT: Marking of transparent glass doors- Sec. 241-b, Labor Law	
<p>Section 241 of the Labor Law has been amended so as to require that all transparent glass doors-in mercantile establishments and in public and commercial buildings and structures be marked in such manner so as to warn persons using same that such doors are glass doors.</p> <p>Section 666 of the New York City Charter stipulates that the New York City Board of Standards and Appeals shall have the power to make rules and regulations for enforcement of those provisions of the Labor Law which relate to buildings within the city, which shall take the place of the Industrial Code and of any rules and regulations of the Department of Labor of the State of New York relating to the same subject matter.</p> <p>The requirements for marking of such doors was reviewed with Chairman Glass, New York City Board of Standards and Appeals, and it was decided that pending the promulgation of rules by the Board, that Industrial Code Rule 47 shall be applicable.</p>		

Figure 2

The marking of glass doors and side panels went into effect on Jan. 1, 1968.
 The building commissioner’s directive was made public on Feb. 6, 1968.

The directive did not support the defense attorney’s theory because it required the building owner to mark the glass panels and had been in effect for at least 40 years.

The author agreed with the opposing expert that the building owners had not marked the panels, which was a violation. The author’s initial suggestion was that the defense submit to the claim. However, on reading the case material, the author saw the change in oral evidence from “run” to “walk” and suggested to the defense (who did not realize the walk/run distinction) that an analysis be performed to compare the stresses on the glass between the impact of running and walking.

The author was permitted to perform an analysis regarding the stress on the glass panel for walking and running into the panel. This required engineering analysis to determine the magnitude of dynamic force necessary to break the glass panel and let the trier of fact apportion liability to the parties accordingly.

Case Material Reviewed

The author reviewed three photostats of photographs of the inner entranceway of the glass side panel where the event occurred, the verified bill of particulars with attachments, the opposing expert disclosure, and the report of the plaintiff's expert. That report included: photostats of photographs, original design engineering calculations for wind, and plans of the entranceway doors, mullions, connections, etc. Also reviewed were the fire department's EMS report, the safety department incident report, several depositions (including the plaintiff and building maintenance personnel), and references regarding human factors, ergonomics, and material properties of plate glass.

The author visited the location and took measurements/photographs. On the date of the inspection, the scene was not in the same condition represented in the photographs because the interior easterly glass panel had been repaired. Note that the glass panel was in direct line and direction of travel of the plaintiff descending the stairs (**Figure 1**).

Analysis Methods

The glass panel consisted of two ¼-inch-thick panels sandwiched together, as shown in **Figure 3**, which was adjacent to the exit doorway. The panel on the other exit doorway was the original glass, and the author was able to measure the thickness as well as the unsupported height and width of the panel. The glass panel appeared to be substantially fixed and supported around all edges of the panel, but the window frame could not be disassembled to ascertain the specific mounting and weather sealing method used. The analysis assumption was that the glass panel would behave as a membrane because the thickness relative to the shortest dimension was large — approximately 90 to 1, which is above the threshold of 80 to 1 for membrane analysis¹. The analysis assumed that the membrane was flexible and infinitely thin, of uniform material and thickness, and that it would elastically stretch uniformly in all directions when deflected. Hence, if it failed, it would fail in tension^{1,2}. The impact load was considered to be perpendicular to the plate surface. Testing of the pushing strength was estimated to be approximately 15% of the male's weight. Based on the plaintiff's weight of 180 pounds, that pushing force equals 27 pounds of force³. Another source of arm strength estimated 37 pounds of force⁴. Based on the average for the arm pushing force against the panel on sources, the author used 32 pounds of force

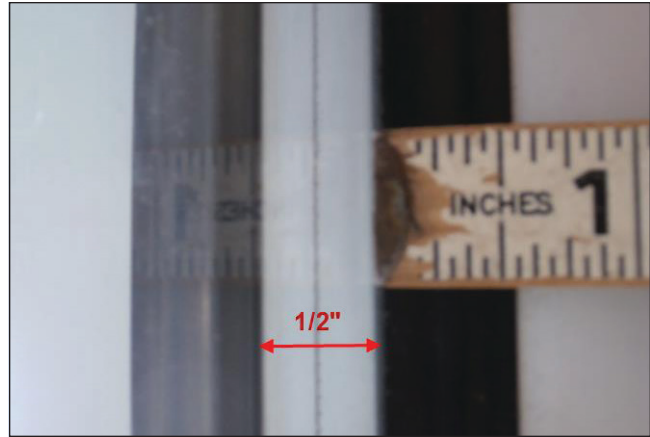


Figure 3

The photograph represents the measurement taken of the thickness of the sandwiched glass panels of ¼ inch each. The panel was the original installed glass panel similar to the one that the plaintiff impacted.

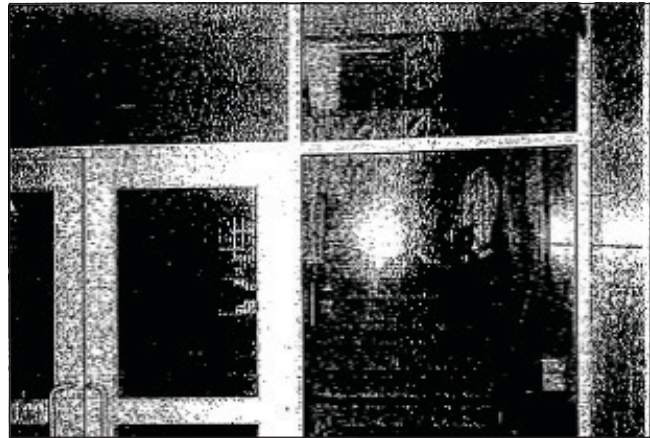


Figure 4

The poor photographic reproduction shows the glass panel as viewed from the outer lobby entrance. The shards of glass still remaining in the frame can be barely observed.



Figure 5

Poor photographic reproduction of the glass panel taken from the outer lobby to show the glass shards. The shards of glass remaining in the frame would indicate that the panel was substantially fixed within the frame.

for the load on the glass panel. See calculations in the **Appendix** for further analysis.

The author performed an analysis to determine the stress on the glass panel walking at 4 feet per second (fps), the design speed for walking per the Manual of Uniform Traffic Control Devices (MUTCD), the American Association of State Highway and Transportation Officials (AASHTO), and other studies that are referenced to determine the running speed of pedestrians descending stairs and then accelerating to a run or sprint. The average fast descending speed on stairs of pedestrians is approximately 2.3 fps. The average acceleration of a pedestrian reaching the ground floor landing while still in motion is approximately 0.2 g's — for a maximum of 1 second. This calculated to a pedestrian velocity, using the two velocity equations (one using a time and the other using distance). Using a time of 1 second, the velocity yields 8.7 fps; using a distance of 7 feet, the distance of the bottom step to the glass panel, yields 9.8 fps. The author averaged the two results and used 9.25 fps. This value of the plaintiff's speed was derived from various tests of pedestrians descending stairs and the acceleration of sprinters/runners from a walk to a run⁵⁻¹². It should be noted that the speed of pedestrians is a function of slope of the stairs, dimension of the treads and risers, and the number of other pedestrians in the area. At the time of incident, there was a change in classes so the corridors and stairs were not empty, which may have affected the speed of the plaintiff.

As mentioned, the glass panel was treated as a thin plate or membrane. The dimensions of the glass plate were 81.75 inches in height, 45.5 inches in width, and two ¼-inch thicknesses. The thickness used for glass was calculated using the equivalent thickness of two ¼-inch panels into one equivalent thickness. The calculation was arrived at by equating the two ¼-inch panels using mass moment of inertia into the equivalent of one glass panel. The resulting equivalent thickness of a single glass panel was 0.50005 inches. Sliding between the two ¼-inch glass panels was not considered because the edges of both panels were substantially fixed and tightly sandwiched together in the frame, and the author was not able to compare this model to a sliding model. This assumption may be a source of error. See labeled mass moment of inertia calculations in the **Appendix**. Another potential source of error in "combining" these glass panels is that glass is a brittle material and will behave differently than a typical elastic-plastic deforming material. The glass panel was annealed glass, not safety

glass, which would have broken in small pieces — not the shards that caused the serious cuts in the plaintiff's arm and wrist¹³.

In order to determine the breaking stress on the glass panel, it was necessary to derive the dynamic impact force of the panel and apply the loads to a static model. Because the thickness of the glass panel was much smaller than the shortest dimension of the panel, the panel could be treated as a membrane. The force was dynamically applied. Using Timoshenko's "Vibration Problems in Engineering"², a 2nd order differential equation was set up and solved using the initial conditions. The initial conditions were: (1) at time zero, the deflection of the panel was zero; and (2) at time zero, the change in velocity of the panel was due to the impact. Damping of the vibration was considered to be between 1% and 8% of the natural frequency. A damping vibration of 4% of the natural frequency was used based on the density and thickness of the glass panel¹⁴.

The analysis of the model calculated the acceleration and force on the glass panel using an impact speed of 4 fps and 9.25 fps as the initial conditions. The force on the model glass panel was a pressure force at the mid-point of the panel derived from the estimated dynamically pressing of the hand on the panel. The estimated area of the hand applying the load was approximately 18 square inches. The acceleration was calculated, and the corresponding force was the equivalent static load applied to the glass panel. See graphs 1a, 1b, 2a, and 2b in the **Appendix**. Once the force was calculated, the load was placed in "Roark's Stress and Strain Formulas" for flat plates with fixed edges all around. Roark Formula criteria were that the plate was not stressed beyond its elastic limit¹⁵. Because glass is a brittle material, it would not be stressed beyond the elastic limit. As a comparison, the author compared the end conditions if the plate was simply supported and loaded identically. The method and calculations are attached in the **Appendix**.

Results

The outcome of the analysis for fixed edges resulted in a stress of approximately 2,565 psi for walking into the glass panel, which was less than the tensile failure stress of 5,000 psi for glass. The stress for running into the glass panel was approximately 5,932 psi, which exceeded the tensile failure stress of 5,000 psi for glass¹⁶. If the plate was simply supported on all edges, the results were 3,269 psi and 7,559

psi for walking and running, respectively. Under the same loading conditions, the simply supported edges would undergo higher stresses as compared to the fixed supported edges. One consideration that could not be accommodated was the potential effect on edge damping that could result from the use of rubber or other compliant weather sealing material between the windows and rigid frame. See the **Appendix** for the Roark calculation.

References

1. Ventsel E, Krauthammer T. Thin plates and shells, theory, analysis, and applications. New York: Marcel Dekker, Inc.; 2001.
2. Timoshenko S. Vibration problems in engineering, 2nd edition. Hoboken, NJ: John Wiley & Sons; 1990.
3. Peebles L, Norris B. The handbook of adult anthropometric and strength measurements. Nottingham, England: Institute for Occupational Ergonomics, Department of Manufacturing Engineering and Operations Management; 1995.
4. Kroemer K, Grandjean E. Fitting the task to the human, a textbook of occupational ergonomics, 5th edition. Abingdon, England: Taylor & Francis; 1997.
5. Manual of uniform traffic control devices, 2003 edition. Washington, D.C.: United States Department of Transportation – Federal Highway Administration; 2012.
6. A policy on geometric design of highways and streets (“Green Book”), 6th edition. Washington D.C.: American Association of State Highway and Transportation Officials.
7. Fujiyama T, Tyler N. An explicit study on walking speeds of pedestrians on stairs. Centre for Transport Studies, University College London, United Kingdom; 2004.
8. Fruin JJ. Pedestrian planning and design. New York: Metropolitan Association of Urban Designers and Environmental Planners, Inc.; 1971.
9. Shah J, Joshi G, Parida P. Walking speed of pedestrian on stairways at intercity railway station in India, Vol 9. Proceedings of the Eastern Asia Society for Transportation Studies; 2013.
10. Zębala J, Ciępka P, Reza A. Pedestrian acceleration and speeds, problems of forensic sciences, Vol 91. Krakow, Poland: Institute of Forensic Research; 1991.
11. New Jersey Department of Transportation. Pedestrian compatible planning and design guidelines. Cherry Hill, NJ: NJDOT; [accessed 2015 September 8]. <http://www.state.nj.us/transportation/publicat/pdf/PedComp/pedintro.pdf>.
12. Ramsley CG, Sleeper HR. Architectural graphic standards, 9th edition. Hoboken, NJ: John Wiley & Sons; 1994.
13. McLellan G, Shand EB. Glass engineering handbook, 3rd edition. New York: McGraw Hill; 1984.
14. Larcher M, Manara G. Influence of air damping on structures especially glass. Ispra, Italy: Joint Research Centre, European Commission; 2010.
15. Young W, Budynas R. Roark’s formulas for stress and strain, 7th edition. New York: McGraw Hill; 2002.
16. Marks L. Mechanical engineering handbook, 5th edition. New York: McGraw-Hill; 1951.

Conclusion

Within a reasonable degree of engineering certainty — and within the estimates and approximations stated — walking/running speeds greater than normal walking speeds would have broken the glass under the equivalent dynamic loading conditions. The fact that the plaintiff was running, as originally stated, resulted in an apportionment of liability by the trier of fact.

Appendix

$$W_t := 180 \cdot lb$$

Weight of male contacting glass panel.

$$R_{arm} := 32 \text{ lbf}$$

Force the arm pushes on the glass panel per an average of various ergonomics estimates ³⁻⁶

Calculation of the running speed into the glass panel by the plaintiff using data from pedestriains studies of pedestrians descending stairs; and the acceleration of runners/sprinters off the start line adjusted for the non-sprinter/runner.

$$v_{descend} := 2.3 \frac{ft}{s}$$

Average stair descending pedestrian speed from reference Centre for Transport Studies, University College London, United Kingdom ⁷⁻¹⁴

$$f_{acc} := 0.2$$

Estimated acceleration based on runners/sprinters off the start line as 1 g and adjusted for pedestrian already in motion and not in a competition.

$$dist_{landing} := 7 \text{ ft}$$

Landing length from bottom stair to the glass panel.

$$t_{acc} := 1 \text{ s}$$

Standard pedestrian acceleration time from start.

$$v_{impact1} := v_{descend} + f_{acc} \cdot g \cdot t_{acc}$$

Impact speed using time of acceleration.

$$v_{impact1} = 8.73 \frac{ft}{s}$$

$$v_{impact2} := \sqrt{v_{descend}^2 + 2 \cdot f_{acc} \cdot g \cdot dist_{landing}}$$

Impact speed using the distance from the stair to the glass panel.

$$v_{impact2} = 9.77 \frac{ft}{s}$$

$$v_{impact} := \frac{v_{impact1} + v_{impact2}}{2}$$

Average velocity calculation.

$$v_{impact} = 9.25 \frac{ft}{s}$$

Use the average impact speed of the time and distance calculated.

Calculation of the equivalent thickness of a single glass panel from two 1/4" glass panels sandwiched and fixed all around the edges.

Using mass moment of inertia find the equivalent plate thickness of one plate in place of two 1/4" plates.

$$t_1 := 0.25 \cdot \text{in}$$

Plate thickness.

$$L_w := 81.75 \cdot \text{in}$$

Plate length (b).

$$W_w := 45.5 \cdot \text{in}$$

Plate width (a).

$$I_1 = 2 \cdot \left(\frac{1}{12} \cdot \left(\frac{\rho \cdot L_w \cdot W_w \cdot t_1}{g} \cdot W_w^2 + \frac{\rho \cdot L_w \cdot W_w \cdot t_1}{g} \cdot \left(\frac{t_1}{2} \right)^2 \right) \right)$$

Moment of inertia for 2 - 1/4" plates moving the cg to the edge of the plate.

$$I_2 = \frac{1}{12} \cdot \frac{\rho \cdot L_w \cdot W_w \cdot t_2}{g} \cdot W_w^2$$

Moment of inertia of the equivalent plate.

$$\frac{1}{12} \cdot \frac{\rho \cdot L_w \cdot W_w \cdot t_2}{g} \cdot W_w^2 = 2 \cdot \left(\frac{1}{12} \cdot \frac{\rho \cdot L_w \cdot W_w \cdot t_1}{g} \cdot W_w^2 + \frac{\rho \cdot L_w \cdot W_w \cdot t_1}{g} \cdot \left(\frac{t_1}{2} \right)^2 \right)$$

$$\frac{1}{12} \cdot t_2 \cdot W_w^2 = 2 \cdot \left(\frac{1}{12} \cdot t_1 \cdot W_w^2 + t_1 \cdot \left(\frac{t_1}{2} \right)^2 \right)$$

Equating the moments of inertia.

$$t_2 = 2 \cdot \left(t_1 + \frac{12 \cdot t_1}{W_w^2} \cdot \left(\frac{t_1}{2} \right)^2 \right)$$

Equivalent thickness of plate.

$$t_2 := \left(t_1 + \frac{3 \cdot t_1^3}{W_w^2} \right) \cdot 2$$

$$t_2 = 0.50005 \text{ in}$$

This is the equivalent thickness of 2 - 1/4" plates sandwiched together and clamped (fixed) on all edges as one plate.

Orientation of plate glass where "b" in the long edge and "a" is the short edge.

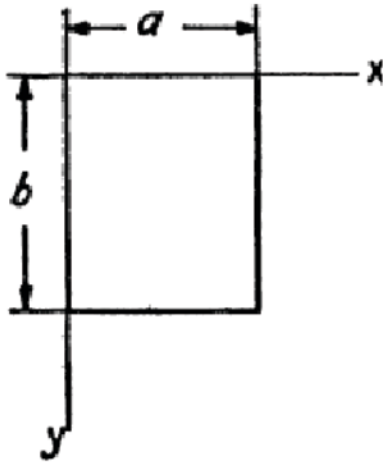


Figure 6.

Note: The properties of annealed glass were taken from various sources with an approximate average used in this analysis.

Specifications of glass panel.

$$\rho := 2.2 \cdot \frac{gm}{cm^3}$$

$$\rho = 137.3 \frac{lb}{ft^3}$$

Density of glass.

$$E := 10000000 \cdot \frac{lbf}{in^2}$$

$$E = 10000000 \text{ psi}$$

Young's modulus for glass.

$$L := 81.75 \cdot in$$

Vertical dimension of glass panel.

$$W := 45.5 \cdot in$$

Horizontal dimension of glass panel.

$$H := 0.50005 \cdot in$$

Thickness of two quarter inch thickness of glass panel.

$$W_g := L \cdot W \cdot H \cdot \rho$$

$$W_g = 147.8 \text{ lb}$$

Weight of equivalent thickness glass panel.

Using momentum, calculate the velocity that the glass panel is subjected to as it sits edges fixed in the frame. Use 4 fps as estimated walking speed and 9.25 fps as running speed.

$$W_b := R_{arm}$$

$$W_b = 32 \text{ lbf}$$

Force of boy's arm striking glass panel.

$$M_g := \frac{W_g}{g}$$

$$M_g = 4.6 \frac{\text{lb} \cdot \text{s}^2}{\text{ft}}$$

Mass of glass panel.

$$M_b := \frac{W_t}{g}$$

$$M_b = 5.6 \frac{\text{lb} \cdot \text{s}^2}{\text{ft}}$$

Mass of boy striking glass panel.

$$v_{b1} := 9.25 \cdot \frac{\text{ft}}{\text{s}}$$

$$v_{b2} := 4 \cdot \frac{\text{ft}}{\text{s}}$$

Velocity boy strikes glass panel walking and running.

$$v_{g1} := \frac{W_t}{(W_t + W_g)} \cdot v_{b1}$$

$$v_{g1} = 5.08 \frac{\text{ft}}{\text{s}}$$

Change in velocity of the glass running. From Linear Momentum.

$$v_{g2} := \frac{W_t}{(W_t + W_g)} \cdot v_{b2}$$

$$v_{g2} = 2.2 \frac{\text{ft}}{\text{s}}$$

Change in velocity of the glass walking. From Linear Momentum.

From Linear Momentum:

$$m_b \cdot v_b + m_g \cdot v_g = m_b \cdot v_b' + m_g \cdot v_g'$$

$$m_b \cdot v_b = (m_b + m_g) \cdot v'$$

$$v' = \frac{m_b}{(m_b + m_g)} \cdot v_b$$

Since the initial velocity of the glass panel is zero; and both the boy and the glass panel achieve the same velocity at impact then the post velocities are the same.

v' is the velocity of the glass panel to be used as the initial condition at time zero.

Analyze the plate glass window using Timoshenko, "Vibration Problems in Engineering", 2nd Edition 5th printing, 1937, D. Van Nostrand Company, Section 70, Vibration of Plates, beginning on page 421. Figure 8.

$$\frac{\gamma \cdot h}{g} \cdot q''(t) + c \cdot q'(t) + \pi^4 \cdot D \cdot q(t) \cdot \left(\frac{m^2}{a^2} + \frac{n^2}{b^2} \right) = 0$$

Differential equation for normal vibration from an applied force with damping term added to equation.

$$p = \pi^2 \cdot \sqrt{\frac{g \cdot D}{\gamma \cdot h} \cdot \left(\frac{m^2}{a^2} + \frac{n^2}{b^2} \right)}$$

Natural frequency of glass panel.

$$2 \cdot s = \frac{c \cdot g}{\gamma \cdot h}$$

Damping term which will be a function of the natural frequency term used further down in calculation.

$$q''(t) + 2 \cdot s \cdot q'(t) + p^2 \cdot q(t) = 0$$

Equation in standard form.

$$q(t) = e^{r \cdot t} \quad q'(t) = r \cdot e^{r \cdot t} \quad q''(t) = r^2 \cdot e^{r \cdot t}$$

Trial solution.

$$r^2 + 2 \cdot r \cdot s + p^2 = 0$$

$$r_1 = -s + \sqrt{s^2 - p^2} \quad r_2 = -s - \sqrt{s^2 - p^2}$$

$$q(t) = C_1 \cdot e^{(-s + \sqrt{s^2 - p^2}) \cdot t} + C_2 \cdot e^{(-s - \sqrt{s^2 - p^2}) \cdot t}$$

General solution to differential equation.

$$-p_1^2 = p^2 + s^2$$

$$q(t) = e^{-s \cdot t} \cdot (C_1 \cdot \cos(-p_1 \cdot t) + C_2 \cdot \sin(-p_1 \cdot t))$$

$$t = 0 \quad q(t) = 0 \quad q'(t) = v$$

Initial conditions.

$$C_1 = 0$$

$$q'(t) = -e^{-s \cdot t} \cdot p_1 \cdot C_2 \cdot \cos(p_1 \cdot t) - s \cdot e^{-s \cdot t} \cdot C_2 \cdot \sin(p_1 \cdot t)$$

$$C_2 = \frac{-v}{p_1}$$

$$q(t) = e^{-s \cdot t} \cdot \left(\frac{v}{\sqrt{p^2 - s^2}} \right) \cdot \sin(\sqrt{p^2 - s^2} \cdot t)$$

Equation of vibration after solving differential equation.

$$h := H$$

$$h = 0.50005 \text{ in}$$

Thickness of two glass panels.

$$v := 0.23$$

Poisson's ratio for glass.

$$\gamma := 0.0806 \cdot \frac{\text{lb}}{\text{in}^3}$$

Glass panel density.

$$D := \frac{E \cdot h^3}{12 \cdot (1 - v^2) \cdot g}$$

$$D = 9168 \text{ lb} \cdot \text{ft}$$

Flexural rigidity of glass panel.

$$a := W$$

$$a = 45.5 \text{ in}$$

Short horizontal dimension of glass panel.

$$b := L$$

$$b = 81.75 \text{ in}$$

Long vertical dimension of glass panel.

$$\text{area}_g := a \cdot b$$

$$\text{area}_g = 26 \text{ ft}^2$$

Area of glass panel.

$$m := 1$$

$$n := 1$$

m & n are Integers for the lowest mode of vibration in Timoshenko equations.
Vibration of panel (page 413)

$$p := \pi^2 \cdot \sqrt{\frac{g \cdot D}{\gamma \cdot h}} \cdot \left(\frac{m^2}{a^2} + \frac{n^2}{b^2} \right) \quad p = 203 \frac{1}{s}$$

Natural frequency of glass panel.

$$T := \frac{2 \cdot \pi}{p}$$

$$T = 0.031 \text{ s}$$

Period of glass panel.

$$t := 0 \cdot \text{ms}, 1 \cdot \text{ms} \dots \frac{T}{4}$$

Time of maximum vibration loading.

$$\zeta := 0.02$$

Damping based on density of 1/2 inch glass as percentage of natural frequency.

$$s := \zeta \cdot p \qquad s = 4.054 \frac{1}{s}$$

Damping term.

$$q_1(t) := e^{-s \cdot t} \cdot \left(\frac{v_{g1}}{\sqrt{p^2 - s^2}} \right) \cdot \sin(\sqrt{p^2 - s^2} \cdot t)$$

Exact solution of differential equation using initial conditions for running.

$$q_1'(t) := \frac{d}{dt} q_1(t)$$

1st derivative; velocity - fps for running.

$$q_1''(t) := \frac{d^2}{dt^2} q_1(t)$$

2nd derivative; acceleration - fpsps for running.

$$q_2(t) := e^{-s \cdot t} \cdot \left(\frac{v_{g2}}{\sqrt{p^2 - s^2}} \right) \cdot \sin(\sqrt{p^2 - s^2} \cdot t)$$

Exact solution of differential equation using initial conditions for walking.

$$q_2'(t) := \frac{d}{dt} q_2(t)$$

1st derivative; velocity - fps for walking.

$$q_2''(t) := \frac{d^2}{dt^2} q_2(t)$$

2nd derivative; acceleration - fpsps for walking.

$$F_1(t) := \frac{W_b}{g} \cdot q_1''(t)$$

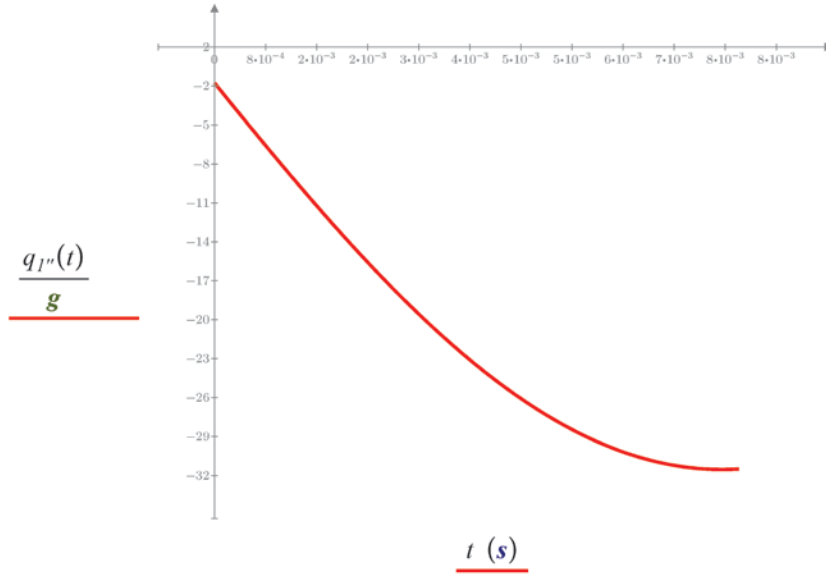
Force on panel for boy running. Where W_b is the applied force on the panel by the arm calculated above.

$$F_2(t) := \frac{W_b}{g} \cdot q_2''(t)$$

Force on panel for boy walking. Where W_b is the applied force on the panel by the arm calculated above.

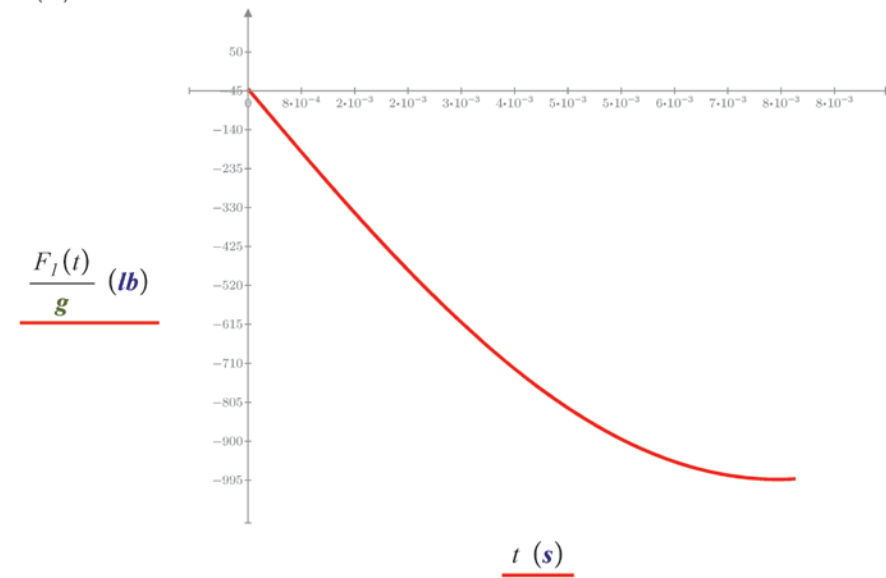
$$q_{1''}\left(\frac{T}{4}\right) = -31 \text{ g}$$

Graph 1a. Maximum running g-force on glass panel.



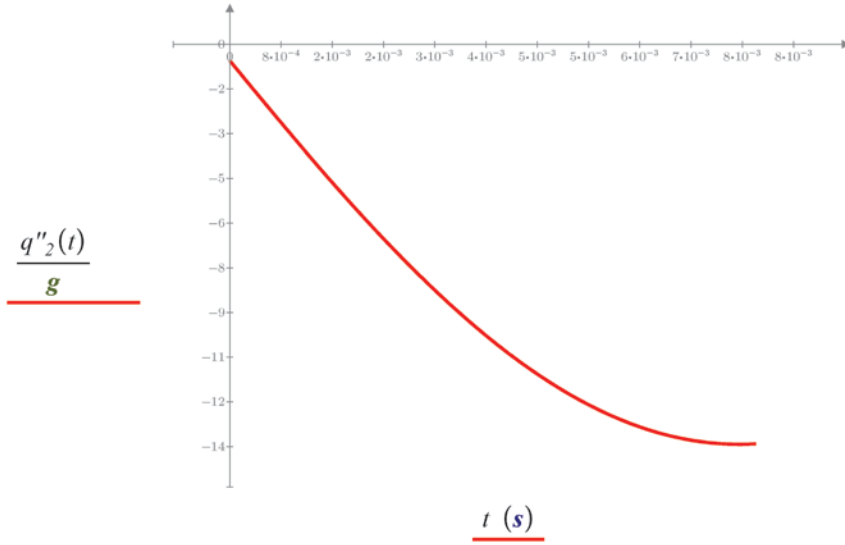
$$F_1\left(\frac{T}{4}\right) = -992 \text{ lbf}$$

Graph 1b. Maximum running force on glass panel.



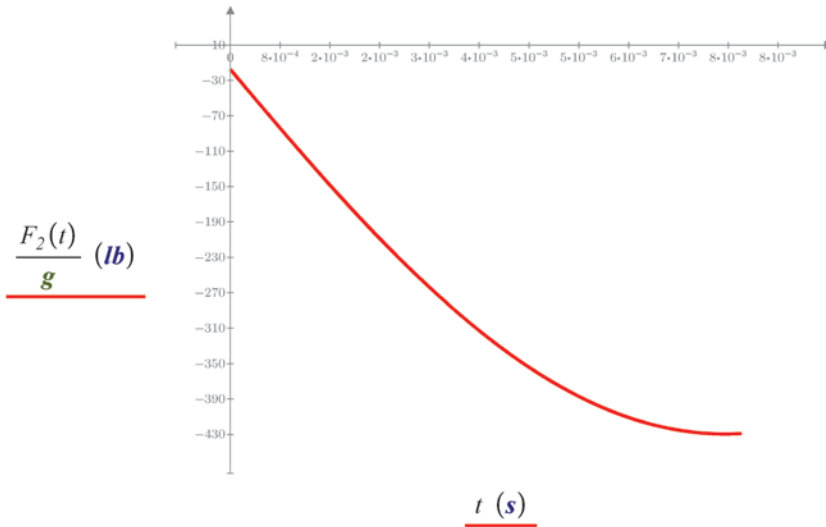
$$q''_2\left(\frac{T}{4}\right) = -13.4 \text{ g}$$

Graph 2a. Maximum walking g-force on glass panel.



$$F_2\left(\frac{T}{4}\right) = -429 \text{ lbf}$$

Graph 2b. Maximum walking force on glass panel.



Calculate the stress on the glass panel using Roark's Stress and Strain Formulas

Reference:

Warren C. Young and Richard G. Budynas, 7th Edition, page 514, Copyright 2002, McGraw-Hill Companies, Inc., Roark's Formulas for Stress and Strain, Uniform over small concentric circle of radius r_o (note definition of $r'o$), page 514. Figure 9.

See Table 11.4 Formulas for flat plates with straight boundaries and constant thickness. Uniform over small concentric circle of radius r_o where

$$r'_o = \sqrt{1.6 r_o^2 + t^2} - 0.675 t \quad r'_o = r_o \quad \text{if} \quad r_o \geq 0.5 t$$

Calculation using Roark's Formula fixed edges.

$$a := 81.75 \cdot \text{in}$$

Long plate dimension.

$$b := 45.5 \cdot \text{in}$$

Short dimension.

$$\frac{a}{b} = 1.8$$

Ratio a/b for coefficients.

$$\beta_1 := 0.068$$

Beta coefficient from table.

$$t := 0.50005 \cdot \text{in}$$

Equivalent plate thickness.

$$r_o := 2.4 \cdot \text{in}$$

$$r_o = 2.4 \text{ in}$$

Radius of applied load.
(approximate area for hand on glass panel.)

$$E := 10000000 \cdot \text{psi}$$

Young's modulus for glass.

$$P := 429 \cdot \text{lbf}, 992 \cdot \text{lbf}, 992 \cdot \text{lbf}$$

Applied loads.

$$\nu := 0.23$$

Poisson's ratio.

$$\sigma_{mc}(P) := \frac{3 \cdot P}{2 \cdot \pi \cdot t^2} \cdot \left((1 + \nu) \cdot \ln \left(\frac{2 \cdot b}{\pi \cdot r_o} \right) + \beta_1 \right)$$

Maximum tensile stress at the center of the panels for fixed edges.

$$\sigma_{mc}(P) = \begin{bmatrix} 2565 \\ 5932 \end{bmatrix} \text{ psi}$$

Maximum stress at the plate center measured 5,932 psi which is greater than the approximate 5,000 psi, the maximum tensile stress of glass. The stress was created with the velocity of the hand/arm at 9.25 feet/second. Therefore, the plate glass would have failed running into the panel.

Maximum stress at the plate center measured 2,565 psi which is less than 5,000 psi, the approximate maximum stress of glass. The stress was created with the velocity of the body at 4 feet/second. Therefore, walking into the glass panel would not have caused the glass to fail.

Calculation using Roark's Formula simply supported edges.
For Uniform over small concentric circle of radius r_o where all edges are simply supported for rectangular plate.

$$\beta_2 := 0.927$$

Beta coefficient from Roark table.

$$r'_o := r_o$$

Radius of applied load.
(approximate area for hand on glass panel.)

$$\sigma_{max}(P) := \frac{3 \cdot P}{2 \cdot \pi \cdot t^2} \cdot \left((1 + \nu) \cdot \ln \left(\frac{2 \cdot b}{\pi \cdot r'_o} \right) + \beta_2 \right)$$

Maximum tensile stress at the center of the panels for simply supported edges.

$$\sigma_{max}(P) = \begin{bmatrix} 3269 \\ 7559 \end{bmatrix} \text{ psi}$$

Under the same loading conditions, the simply supported edges would undergo higher stresses as compared to the fixed supported edges.

Maximum stress at the plate center measured 7,559 psi which is greater than the approximate 5,000 psi, the maximum tensile stress of glass. The stress was created with the velocity of the hand/arm at 9.25 feet/second. Therefore, the plate glass would have failed running into the panel under the simply supported analysis.

Maximum stress at the plate center measured 3,269 psi which is less than 5,000 psi, the approximate maximum stress of glass. The stress was created with the velocity of the body at 4 feet/second. Therefore, walking into the glass panel would not have caused the glass to fail under the simply supported analysis.